Using inelastic scattering of light to understand the nature of electron-phonon interactions and phonon self-energy renormalizations in graphene materials

Daniela Lopes Mafra

August 2012

Using inelastic scattering of light to understand the nature of electron-phonon interactions and phonon self-energy renormalizations in graphene materials

Daniela Lopes Mafra

Orientador: Prof. Marcos Assunção Pimenta

Tese de doutorado apresentada ao Departamento de Física da Universidade Federal de Minas Gerais como requisito parcial para a obtenção do grau de Doutor em Física.

August 2012

To Hugo, Quita and Sérgio, my life...
To Paulo, my love...

Contents

Abstract

In the last decade, many theoretical and experimental achievements have been made in the physics of graphene. In particular, Raman spectroscopy has been playing an important role in unraveling the properties of graphene systems. In this thesis we use the Raman spectroscopy to study some effects of the electron-phonon coupling in monolayer and bilayer graphene and to probe the electronic and vibrational structure of bilayer graphene. Phonon self-energy corrections have mostly been studied theoretically and experimentally for phonon modes with zone-center ($q = 0$) wavevectors. Here, we combine Raman spectroscopy and gate voltage to study phonons of monolayer graphene for the features originated from a double-resonant Raman (DRR) process with $q \neq 0$ wavevectors. We observe phonon renormalization effects in which there is a softening of the frequency and a broadening of the decay width with increasing the gate voltage, that is opposite from what is observed for the zone-center $q = 0$ case. We show that this renormalization is a signature for the phonons with $q \approx 2k$ wavevector that come from both intravalley and intervalley DRR processes. Within this framework, we resolve the identification of the phonon modes contributing to the G* Raman feature, at $\sim 2450\,\mathrm{cm}^{-1}$, and also for five second order Raman combination modes in the frequency range of $1700 - 2300\,\mathrm{cm}^{-1}$ of monolayer graphene. By combining the DRR theory with the anomalous phonon renormalization effect, we show a new technique for using Raman spectroscopy to identify the proper phonon mode assignment for each combination mode.

We also study the behavior of the optical phonon modes in bilayer graphene devices by applying top gate voltage, using Raman scattering. We observe the splitting of the Raman G band as we tune the Fermi level of the sample, which is explained in terms of mixing of the Raman (E_g) and infrared (E_u) phonon modes, due to different doping in the two layers. We show that the comparison between the experiment and theoretical model not only gives information about the total charge concentration in the bilayer graphene device, but also allows to separately quantify the amount of unintentional charge coming from the top and the bottom of the system, and therefore to characterize the intrinsic charges of bilayer graphene with its surrounding environment.

In the second part of this thesis, the dispersion of electrons and phonons near the K point of bilayer graphene was investigated in a resonant Raman study of the G$'$ band using different laser excitation energies in the near-infrared and visible range. The electronic structure was analyzed within the tight-binding approximation, and the

Slonczewski-Weiss-McClure (SWM) parameters were obtained from the analysis of the dispersive behavior of the G′ band considering both the inner and the outer DRR processes. We show that the SWM parameters obtained considering the inner process are in better agreement with those obtained from other experimental techniques, strongly suggesting that the inner process is the main responsible for the G′ feature in graphene.

Additionally, the dependence of the intensity of the four peaks that compose the G′ band of bilayer graphene with laser excitation energy and laser power is explored and explained in terms of the electron-phonon coupling and the relaxation of the photon-excited electron. We show that the carrier relaxation occurs predominantly by emitting a low-energy acoustic phonon and the different combinations of relaxation processes determine the relative intensities of the four peaks that give rise to the G′ band. Some peaks show an increase of their intensity at the expense of others, thereby making the intensity of the peaks both different from each other and dependent on laser excitation energy and on power level. This effect gives important information about the electron and phonon dynamics and needs to be taken into account for certain applications of bilayer graphene in the field of nanotechnology.

Resumo

Na última década, muitos avanços teóricos e experimentais foram alcançados na física do grafeno. Em particular, a espectroscopia Raman tem sido muito importante para a elucidar propriedades físicas e químicas em sistemas de grafeno. Nessa tese nós usamos a espectroscopia Raman para estudar alguns dos efeitos do acoplamento elétron-fônon no grafeno de camada única e de dupla camada, e para se obter informações sobre a estrutura eletrônica e vibracional do grafeno de camada dupla. As renormalizações das energias dos fônons tem sido estudadas basicamente para fônons com vetor de onda nulo ($q = 0$). Aqui, nós combinamos a espectroscopia Raman com aplicação de tensão de porta para estudar, em grafeno de camada única, as bandas originadas do processo Raman com dupla ressonância (DRR) com vetores de onda $q \neq 0$. Nós observamos os efeitos de renormalização dos fônons, em que há a diminuição da frequência e o alargamento no decaimento dos fônons com o aumento da tensão de porta, e esse efeito é o oposto do que é observado para os fônons com $q = 0$. Nós mostramos que esse tipo de renormalização observada é uma assinatura dos fônons com vetor de onda $q \approx 2k$ que vêm de um processo DRR intervale ou intravale. Dentro desse contexto, nós identificamos, para o grafeno de camada única, os modos de fônons que contribuem para a banda Raman G*, em $\sim 2450\,\mathrm{cm}^{-1}$, e para outros cinco picos provenientes de combinação de modos na região de frequência $1700 - 2300\,\mathrm{cm}^{-1}$. Combinando a teoria do processo DRR com o efeito de renormalização de fônons, nós mostramos uma nova técnica para usar a espectroscopia Raman para identificar cada modo Raman apropriadamente.

Nós também estudamos o comportamento dos modos ópticos do grafeno de camada dupla combinando-se o espalhamento Raman e a aplicação de tensão de porta em dispositivos desse material. Nós observamos que a banda G se divide em duas quando o nível de Fermi da amostra é mudado, e isso é explicado em termos da mistura dos modos de fônon Raman (E_g) e infravermelho (E_u) devido a diferença de concentração de carga nas duas camadas. Nós mostramos que a comparação entre os dados experimentais e o modelo teórico não dá apenas informação sobre a concentração de carga total no dispositivo de grafeno de camada dupla, mas também nos permite quantificar separadamente as cargas não intencionais provenientes da camada de cima e de baixo do sistema, e, portanto, caracterizar a interação do grafeno de camada dupla com o ambiente em sua volta.

Na segunda parte dessa tese, a dispersão de elétrons e fônons perto do ponto K do grafeno de camada dupla é investigado através do estudo da banda G$'$ usando

várias energias de excitação de laser na região do infravermelho e do visível. A estrutura eletrônica foi analisada dentro da aproximação de ligações-forte, e os parâmetros Slonczewski-Weiss-McClure (SWM) foram obtidos através do comportamento dispersivo da banda G′ considerando-se tanto o processo DRR interno quanto o externo. Nós mostramos que os parâmetros SWM obtidos considerando-se o processo DRR interno está em melhor acordo com os valores obtidos por outras técnicas experimentais, sugerindo fortemente que o processo interno é o principal responsável pela banda G′ no grafeno.

Além disso, a dependência da intensidade dos quatro picos que compõe a banda G′ do grafeno de camada dupla com a energia de excitação de laser e com a potência do laser é explorada e explicada em termos do acoplamento elétron-fônon e do relaxamento dos elétrons foto-excitados. Nós mostramos que o relaxamento dos elétrons ocorre predominantemente pela emissão de fônons acústicos de baixa energia e as diferentes combinações dos processos de relaxamento determinam as intensidades relativas dos quatro picos que dão origem à banda G′. Esse efeito nos fornece informações importantes sobre a dinâmica dos elétrons e fônons e precisa ser levado em conta para aplicações do grafeno de camada dupla do campo nanotecnológico.

Chapter 1

Introduction

Why phonon and electron-phonon interactions matters? This question is undoubtable the start-point to understand many fundamental phenomena in solids. *Phonon* is the name given to a quantum of energy of traveling vibrational wave in a solid. Because the interatomic forces in a solid are so strong, there is little profit in considering the motion of an atom in a crystal in terms of particle motion. Any momentum we might give to one atom is so quickly transmitted to its neighbors that after a very short time it would be difficult to tell which atom we had initially displaced. But we do know that a vibrational wave in the solid will exist for a much longer time before it is attenuated, and is therefore a much more useful picture of an excitation in the material. Since a vibrational wave is specified by giving the coordinates not of just one atom but of every atom in the solid, we call this a collective motion. A phonon is thus an example of a collective excitation in a solid [1].

Usually, the states of matter are principally studied in terms of electronic degrees of freedom in materials. However the coupling of the electronic degrees of freedom to lattice degrees of freedom is seen to play a crucial role in the materials properties. This coupling is usually described by interactions between the electronic excitations and phonons and is responsible for many interesting effects in a crystal. The most classical effect of the electron-phonon coupling is the the formation of polaron, which is a quasi-particle composed of a charge and its accompanying polarization field. Polarons can be understood as follows: when an electron moves in a crystal, interacting with lattice ions through long-range forces, the positive ions will be attracted towards the electron resulting in the lattice polarization and deformation. Moving through the crystal, the electron carries the lattice distortion with it, thus one speaks of a cloud of phonons accompanying the electron. As a consequence, the resulting lattice polarization acts as a potential well that

hinders the movements of the charge, thus decreasing its mobility [1].

Another fundamental consequence of the electron-phonon interactions is the superconductivity phenomenon. In this case, there is an effective electron-electron interaction mediated by phonons, that allow pairs of electrons to form a bound state of lower energy than that of the two free electrons (in other words, phonons that before were scattering electrons apart throughout the material are now helping the electrons to be stuck together. This means less resistance and better conductivity!). The existence of these bound state of two electrons with opposite wavenumber and spin, known as Cooper pairs, provides the foundation for the theory of superconductivity [1]. Additionally, the Peierls transition, in which the dimerization of the lattice occurs to minimize the system energy, and the Kohn anomaly, an abrupt softening of the phonon energy characterized by the discontinuity of the derivative of the phonon frequency, are also fenomena directly related to the electron-phonon coupling. By now, the reader probably has the answer to the question asked earlier and should be convinced of the importance of phonons and electron-phonon interactions in a system.

Electron-phonon interactions can be observed in a diversity of materials. Here, this thesis is mainly devoted to the study of electron-phonon interactions, as well as their consequences, in graphene-like systems, which have been shown as ideal platforms to observe some of the effects mentioned above. Graphene is a special material due to its fascinating electrical, mechanical, optical and thermal properties [2–5]. This strictly two-dimensional material exhibits exceptionally high crystal and electronic quality, in which charge carriers can travel thousands of interatomic distances without scattering [5,6], and has revealed a bunch of new physics and potential technological applications. Particular interest has been turned to monolayer graphene due to the unique nature of its charge carriers, that make it a promisor material for photonics, optoelectronics and organic electronics such as in solar cells, light-emitting, touch screen and photodetctors devices [2,7,8]. Some progress in the application of graphene is already done, as illustrated in Fig. 1.1. In condensed matter physics, most of materials are ruled by the Schrödinger equation, usually being quite sufficient to describe electronic properties of materials. Monolayer graphene is an exception and its charge carriers mimic relativistic particles and are more easily and naturally described starting with the Dirac equation [9]. The electronic structure of monolayer graphene has a linear dispersion around the K point of the Brillouin zone and it is a zero gap semiconductor.

Bilayer graphene does not show the linear electronic dispersion as monolayer graphene, but it has two hyperbolic valence and two hyperbolic conduction bands. Although bilayer

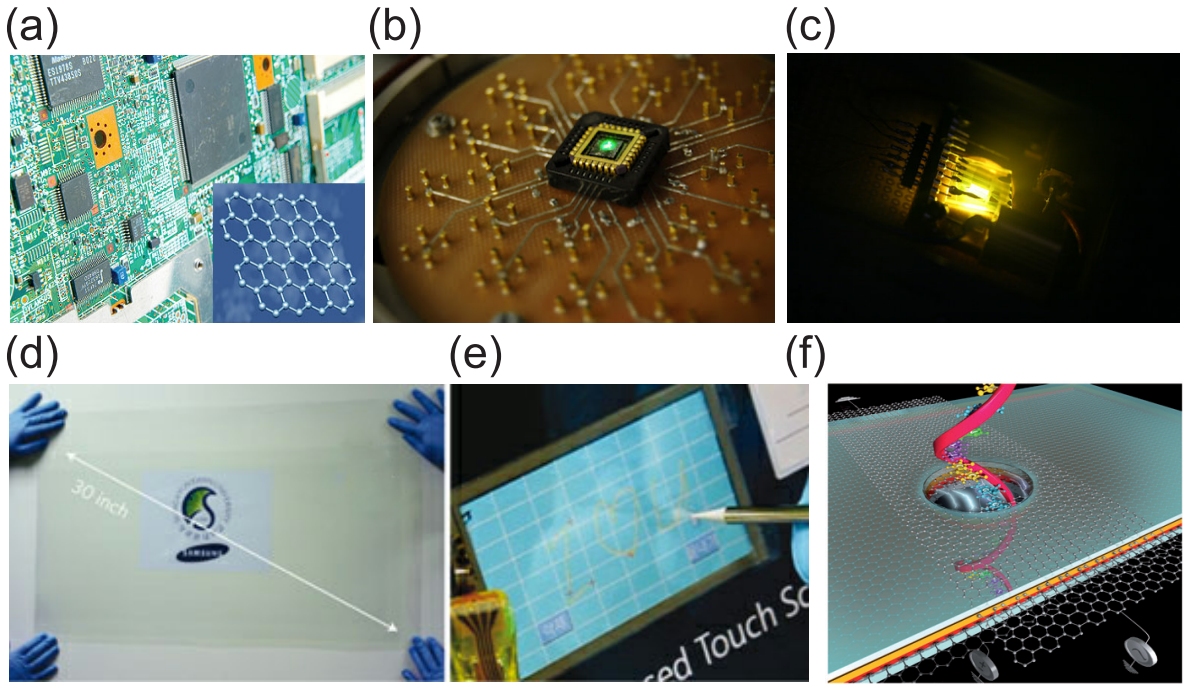

Figure 1.1: (a) Electrons pass through graphene with less resistance than through silicon, making the carbon sheet a good candidate for future chips [12]. (b) Hybrid graphene-quantum dot phototransistors with ultrahigh gain [13]. (c) Light-emitting Electrochemical cell [14]. (d) A transparent ultralarge-area graphene film transferred on a 35-inch PET sheet [8]. (e) A graphene-based touch-screen panel connected to a computer with control software [8]. (f) Graphene nanopore for DNA sequencing [15].

graphene is also a zero gap semiconductor, it is a highly desired material for the development of graphene-based electronics such as field effect transistor [5,6], since it becomes a tunable band gap semiconductor under the application of an electric field perpendicular to the system [10,11]. However, for all the desirable applications of graphene, it is extremely important to understand all the properties of these materials.

In this thesis, gate-modulated and laser energy dependent Raman spectroscopy are the experimental techniques used to characterize monolayer and bilayer graphene. Raman spectroscopy is a fundamental technique to obtain information about the phonons in the material and has historically played an important role in the structural characterization of carbon materials [16]. It has been used in the last decades to characterize graphite, carbon nanotubes, nanographite, amorphous carbon and graphene. Moreover the vibrational and electronic structures of graphene systems can be probed with the use of resonant Raman spectroscopy [17,18], providing experimental support for understanding the vibrational and electronic properties of carbon materials. Also, Raman spectroscopy is a fast and

non-destructive technique.

Traditionally, electron-phonon interactions are investigated through chemical doping, in which the charge carrier density is varied by the introduction of impurities [19]. However, the appliance of electrical fields to control carriers in materials (so-called the electrical field effect) is an alternative method for changing the charge carrier density effectively in low dimensional systems. In this thesis we combine both the electric field effect and Raman spectroscopy to study the electron-phonon coupling in graphene-like systems. Also, a structural study of the bilayer graphene is done by the analysis of the double resonance Raman band known as G′ (or 2D) band.

This thesis is arranged as follows: in Chapter 2, a brief discussion about the electronic and vibrational properties of monolayer and bilayer graphene, together with predictions of electron-phonon interactions in those systems are presented. In Chapter 3 we first present the basic theory of first and second order Raman scattering, and then we explain the origin of the main Raman features in graphene. Chapter 4 explains, in details, all the steps of graphene devices fabrication for the use in both back and top gated studies. In Chapter 5 we make use of Raman spectroscopy to study electron-phonon interactions in monolayer and in bilayer graphene by applying a variable gate voltage on the graphene devices. In Chapter 6 we show how the resonant Raman spectroscopy can be used in graphene systems to gather information about its electronic and vibrational properties. Finally, in Chapter 7, we explain how to obtain information about the phonon dynamics in bilayer graphene by using the double resonance Raman scattering. Chapter 8 summarizes the thesis contents.

Chapter 2

Basic properties of monolayer and bilayer graphene

This chapter brings an overview of the electronic and vibrational structures of graphene. A special focus will be given to the electron-phonon interactions in the last section. In particular, some important consequences of these interactions in the frequency and line width of the zone-center phonons for monolayer and bilayer graphene will be given.

2.1 Structure and group theory of graphene

Graphene is a flat layer of carbon atoms in a honeycomb lattice with sp^2 hybridization. Fig. 2.1(a) shows the hexagonal real space for the monolayer graphene with two inequivalent atoms in the unit cell and the unit cell lattice vectors $\mathbf{a_1}$ and $\mathbf{a_2}$, given by:

$$\mathbf{a}_1 = \frac{a}{2}(\sqrt{3}\hat{x} + \hat{y})\,, \tag{2.1}$$

$$\mathbf{a}_2 = \frac{a}{2}(-\sqrt{3}\hat{x} + \hat{y})\,, \tag{2.2}$$

where $a = \sqrt{3}a_{cc}$ and $a_{cc} = 0.142\,\text{nm}$ is the carbon-carbon bond distance [20]. The real space for bilayer graphene (top view) with AB Bernal stacking are show in Fig. 2.1(b), where the black dots plus black open circles represent the atoms in the lower layer, and red dots represent the atoms in the upper layers. In the AB stacking, one of the atoms of the top layer lays on the top of one atom of the lower layer. The other atom of the top layer lays in the middle of the hexagon of the lower layer. In this thesis, we will only work with AB stacked bilayer graphene. The unit cell of bilayer graphene is composed of four atoms disposed as shown in Fig. 2.1(c). The reciprocal space of monolayer and bilayer

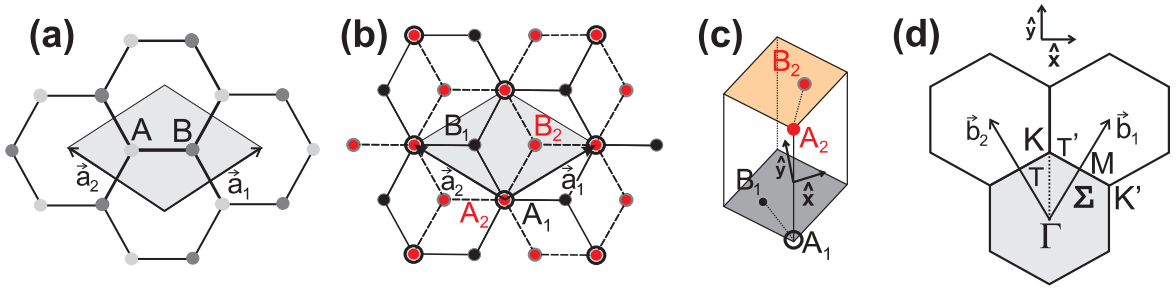

Figure 2.1: (a) The real space of monolayer graphene showing the non-equivalent A and B atoms and the primitive lattice vectors $\mathbf{a_1}$ and $\mathbf{a_2}$. (b) The real space top-view of bilayer graphene. Black dots plus black open circles, and red dots represent the atoms in the lower and upper layers, respectively. (c) The three dimensional unit cells of bilayer graphene. (d) The reciprocal space for both monolayer and bilayer graphene showing the first Brillouin zone in light gray, the high symmetry points and the two reciprocal vectors $\mathbf{b_1}$ and $\mathbf{b_2}$.

graphene is shown in Fig. 2.1(d) highlighting the high symmetry points Γ, K, K', M and the high symmetry lines T, T' and Σ. Any other generic point outside the high symmetry points is named here u. Since there is no periodicity in the $\hat{\hat{z}}$ cartesian direction for bilayer graphene, its reciprocal space is the same of monolayer graphene. The reciprocal vector $\mathbf{b_1}$ and $\mathbf{b_2}$ are given by:

$$\mathbf{b}_1 = \frac{2\pi}{a}\left(\frac{\sqrt{3}}{3}\hat{k_x} + \hat{k_y}\right), \tag{2.3}$$

$$\mathbf{b}_2 = \frac{2\pi}{a}\left(-\frac{\sqrt{3}}{3}\hat{k_x} + \hat{k_y}\right). \tag{2.4}$$

Group theory is a powerful theoretical tool to determine eigenvectors, the number and the degeneracies of eigenvalues and to obtain and understand the selection rules governing, for example, electron-radiation and electron-phonon interactions. The monolayer graphene on an isotropic medium has the space group P6/mmm (D^1_{6h}) in the Hermann-Mauguin (Schoenflies) notation. At the Γ point, the group of wavevector is isomorphic to the point group D_{6h} (the Schoenflies character tables for the point groups can be found in the Appendix B). The symmetries for N-layer graphene, with N even or odd (from now on, N$\neq$ 1), are the same as for bilayer and trilayer graphene, respectively. The point groups isomorphic to the group of the wavevector for monolayer, N-layer graphene (N even and odd), and for N infinite (graphite) are listed in Table 2.1 for all points and lines in the first Brillouin Zone (BZ).

Table 2.1: The space groups and wavevector point groups for monolayer graphene, N-layer graphene and graphite (N infinite) at all points in the BZ.

	Space group	Γ	K (K′)	M	T (T′)	Σ	u
Monolayer	P6/mmm	D_{6h}	D_{3h}	D_{2h}	C_{2v}	C_{2v}	C_{1h}
N even	P$\bar{3}m1$	D_{3d}	D_3	C_{2h}	C_2	C_{1v}	C_1
N odd	P$\bar{6}m2$	D_{3h}	C_{3h}	C_{2v}	C_{1h}	C_{2v}	C_{1h}
N infinite	P$6_3/mmc$	D_{6h}	D_{3h}	D_{2h}	C_{2v}	C_{2v}	C_{1h}

2.2 Electronic structure

2.2.1 Monolayer graphene

The atomic orbitals in graphene are in a sp^2 hybridization, in which the carbon atoms are bounded covalently to each other forming a 120^o angle. There are three in-plane σ orbitals and one out-of-plane π orbital. Since the π electrons are less bounded to the atoms, they can move in the crystal and can be excited to the conduction band more easily than the σ electrons, giving rise to interesting electronic and optical physics phenomena.

The electronic structure of graphene can be described by tight-binding calculations considering interactions with just first neighbors [20]. The problem consists of solving the Schrödinger equation,

$$E_j(\mathbf{k}) = \frac{\langle \psi_j | H | \psi_j \rangle}{\langle \psi_j | \psi_j \rangle}, \tag{2.5}$$

where ψ_i and ψ_j are the Bloch's functions given by:

$$\psi_{\mathbf{k}}(\mathbf{r}) = \sum_j c_j(\mathbf{k}) \varphi_{\mathbf{k}j}(\mathbf{r}), \tag{2.6}$$

where $\varphi_{\mathbf{k}j}(\mathbf{r})$ is given by:

$$\varphi_{\mathbf{k}j}(\mathbf{r}) = \frac{1}{\sqrt{M}} \sum_l e^{i\mathbf{k}.\mathbf{R}(\mathbf{l})} \phi_l(\mathbf{R}(\mathbf{l}) - \mathbf{r}). \tag{2.7}$$

M is the number of unit cells, $\mathbf{R}(\mathbf{l})$ is the vector giving the position of an atom in the j-th unit cell and ϕ_l is the l-th atomic orbital of the atom. It follows that the electronic dispersion of monolayer graphene is given by

$$E_{\pm}(\mathbf{k}) = \frac{\epsilon_{2p} \pm \gamma_0 f(\mathbf{k})}{1 \pm s f(\mathbf{k})}, \tag{2.8}$$

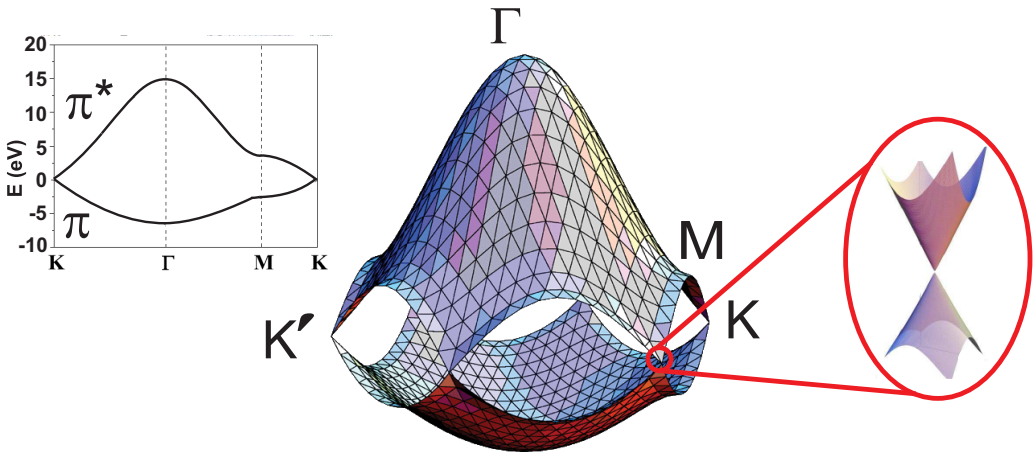

Figure 2.2: The graphene's π and π^* electronic dispersion calculated over the first Brillouin zone. The inset shows the dispersion along the high-symmetry points. The values used for γ_0 and s are, respectively, 3.033 eV and 0.129 eV. [20] The zoom shows the linear dispersion near the K point.

where γ_0 parameter is the nearest neighbor transfer integral between the atomic orbitals of the carbon atoms A and B of the graphene sheet, s is the overlap integral and the function $f(\mathbf{k})$ is given by

$$f(\mathbf{k}) = \sqrt{1 + 4\cos\frac{\sqrt{3}k_x a}{2}\cos\frac{k_y a}{2} + 4\cos^2\frac{k_y a}{2}}\,. \tag{2.9}$$

Eq. 2.8 is plotted as a function of $\mathbf{k}$, as exhibited in the Fig. 2.2. Monolayer graphene is a zero gap semiconductor, where the valence π and conduction $\pi^\star$ bands touch each other at the K (or Dirac) point, and this is where the Fermi level is located. We can expand Eq. 2.8 (considering ϵ_{2p} and s equal zero) for values of $\mathbf{k}$ close to the K point. In this case, the electronic dispersion of monolayer graphene is given by [20]

$$E(k) = \hbar v_F k \tag{2.10}$$

where $v_F = \sqrt{3}\gamma_0 a/2\hbar$ is the Fermi velocity of the electrons near the Dirac point and is close to 1×10^6m/s [5]. We can see that around the K point, the electronic structure can be described as a linear dispersion (see the zoom of Fig. 2.2).

2.2.2 Bilayer graphene

Since the unit cell of AB stacked bilayer graphene is the same as that of graphite (four atoms per unit cell, see Fig. 2.1(c)), we can model the bilayer electronic structure using the tight-binding model for graphite [21] by adapting the Slonczewski-Weiss-McClure

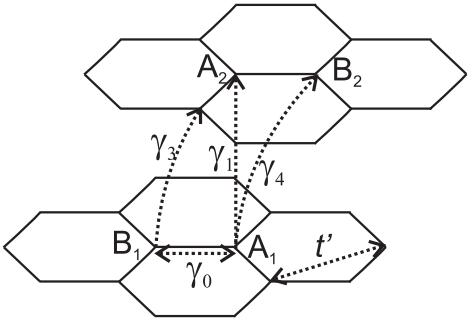

Figure 2.3: The intra- (γ_0 and t') and inter-layer (γ_1, γ_3 and γ_4) tight-binding hoping parameters in bilayer graphene.

(SWM) parametrization [22,23], using the nearest-neighbor hopping parameters γ_0, γ_1, γ_3 and γ_4 (shown in Fig. 2.3). The parameter Δ, which represents the difference between the on-site energies of the two layers, and t', which is the in-plane second-neighbor hopping parameter, can also be included. The electronic structure of bilayer graphene is then, given by solving the 4×4 tight-binding Hamiltonian [24]

$$H_{bilayer} = \begin{pmatrix} \Delta & \gamma_0 f(\mathbf{k}) & \gamma_1 & \gamma_4 f^*(\mathbf{k}) \\ \gamma_0 f^*(\mathbf{k}) & 0 & \gamma_4 f^*(\mathbf{k}) & \gamma_3 f(\mathbf{k}) \\ \gamma_1 & \gamma_4 f(\mathbf{k}) & \Delta & \gamma_0 f^*(\mathbf{k}) \\ \gamma_4 f(\mathbf{k}) & \gamma_3 f^*(\mathbf{k}) & \gamma_0 f(\mathbf{k}) & 0 \end{pmatrix} \tag{2.11}$$

Solving the Hamiltonian, we find two valence bands (π_1 and π_2) and two conduction bands ($\pi_1^\star$ and $\pi_2^\star$). Bilayer graphene is also a zero gap semiconductor but the electronic dispersion is no longer linear around the K point, but it has a hyperbolic dependence with k, as can be seen in Fig. 2.4 [24]. One valence band touch one conduction band at the K point and the other two bands have a gap of $2\gamma_1$. Considering only the γ_0 and γ_1 hopping parameters, the solution for the Hamiltonian can be simplified to [25]

$$E(k) = s\left[\pm\frac{\gamma_1}{2} + \sqrt{\gamma^2 k^2 + \frac{\gamma_1^2}{4}}\right], \tag{2.12}$$

where s is a band index: $+1$ for conduction band and -1 for valence band, and $\gamma = \sqrt{3}\gamma_0 a/2$.

The γ_3 and γ_4 parameters have interesting consequences in the electronic structure. γ_3 gives rise to a trigonal warping effect in the low energy spectrum, where the equienergies curves have triangular shape, while γ_4 is related to the electron-hole asymmetry in bilayer graphene [24]. Figs. 2.5(a) and (b) show, respectively, the bilayer graphene band structure near to the K point with γ_3 and γ_4 equal to zero and with γ_3 and γ_4 different from zero.

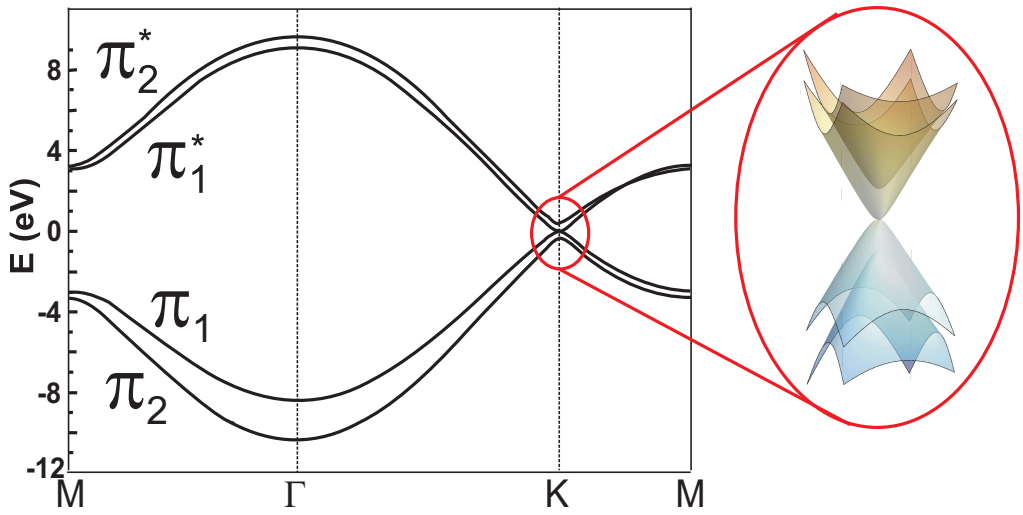

Figure 2.4: Electronic structure of bilayer graphene along the high symmetry lines calculated by Partoens and Peeters [24]. The zoom shows the hyperbolic dispersion near the K point.

Including the γ_3 and γ_4 parameters (Δ and t' were also included), along the high symmetric line ΓKM direction the 4×4 matrix factorizes, and the dispersion of the four electronic bands are given by [18]:

$$E_{\pi_2}^{\pi_1^*} = \frac{-\gamma_1 - \sigma v_3 + \Delta' \pm \xi_1}{2}, \tag{2.13}$$

$$E_{\pi_1}^{\pi_2^*} = \frac{\gamma_1 + \sigma v_3 + \Delta' \pm \xi_2}{2}, \tag{2.14}$$

where $v_i = \gamma_i/\gamma_0$,

$$\Delta' = \Delta + t' \left[2\cos\left(\frac{2\pi}{3} - \frac{\sqrt{3}ka_{cc}}{2}\right) + \cos\left(\frac{4\pi}{3} - \sqrt{3}ka_{cc}\right) \right], \tag{2.15}$$

$$\xi_1^2 = \sqrt{(\gamma_1 + v_3\sigma \pm \Delta')^2 + 4((1 \mp v_4)^2\sigma^2 \mp \sigma v_3(\Delta' \pm \gamma_1))}, \tag{2.16}$$

and

$$\sigma = \gamma_0 \left[2\cos\left(\frac{2\pi}{3} - \frac{\sqrt{3}ka_{cc}}{2}\right) + 1 \right]. \tag{2.17}$$

One major intriguing feature of bilayer graphene is a band structure that can be externally tuned. Ohta *et al.* [26] used angle resolved photoemission to show that bilayer graphene has a gap that can be tuned from 0 to up to 200 meV. Fundamentally, the gap opening in bilayer graphene originates from the breaking of inversion symmetry, that can be achieved, for example, by applying an electric field perpendicular to the layers. This

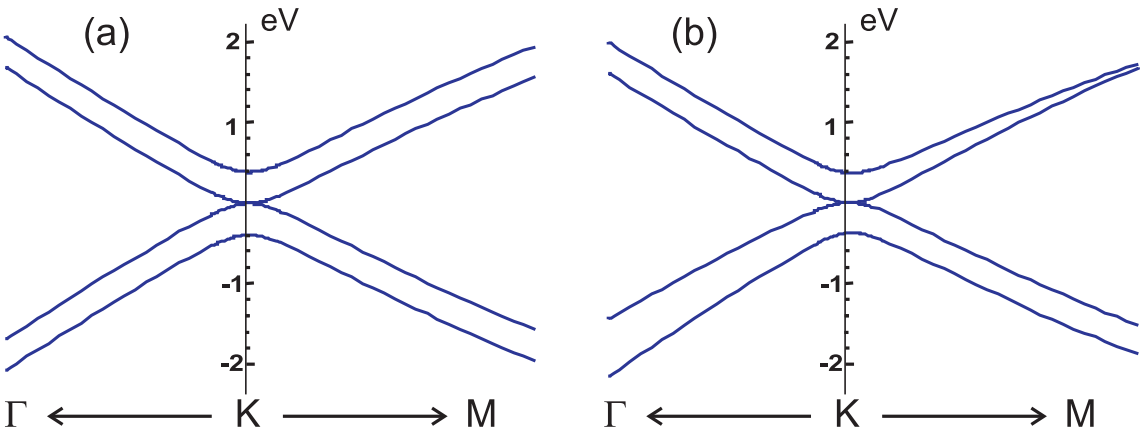

Figure 2.5: Electronic structure of bilayer graphene around the K point using (a) γ_3 and γ_4 equal to zero and (b) γ_3 and γ_4 hopping parameters different from zero ($\gamma_3 = 0.3\,\text{eV}$ and $\gamma_4 = 0.15\,\text{eV}$).

creates an asymmetry between the two layers that lowers the whole symmetry of the bilayer system, consequently opening an electronic band gap at the K point.

2.3 Phonon structure

As shown in Section 2.1, the monolayer graphene sheet has two atoms per unit cell, each one with three degrees of freedom, thus having 6 phonon branches. There are three acoustic (A) branches, with frequency $\omega = 0$ at the Γ point, and three optic (O) branches. Also, the phonon modes are classified as longitudinal (L) or transverse (T) according to vibrations parallel or perpendicular to the carbon-carbon bond directions, respectively. The transverse modes can be in-plane (i) or out-of-plane (o) and the longitudinal modes are always in-plane.

These phonon branches can be calculated by using a simple harmonic oscillator model which lead us to solve the equation

$$M_i \ddot{\mathbf{u}}_i = \sum_j^n K^{ij}(\mathbf{u}_i - \mathbf{u}_j) \ (i = 1, ..., N)\,, \tag{2.18}$$

where $\mathbf{u}_i$ is the displacement of the i-th atom in the unit cell, M_i is the mass of the atom i and K^{ij} is an element of the force constant tensor which gives the interaction strength between atoms i and j [20]. The summation is performed over the n nearest neighbors. Fig. 2.6(a) shows the phonon dispersion for monolayer graphene calculated by force constant method over the entire first Brillouin zone [20] and Fig. 2.6(b) shows the

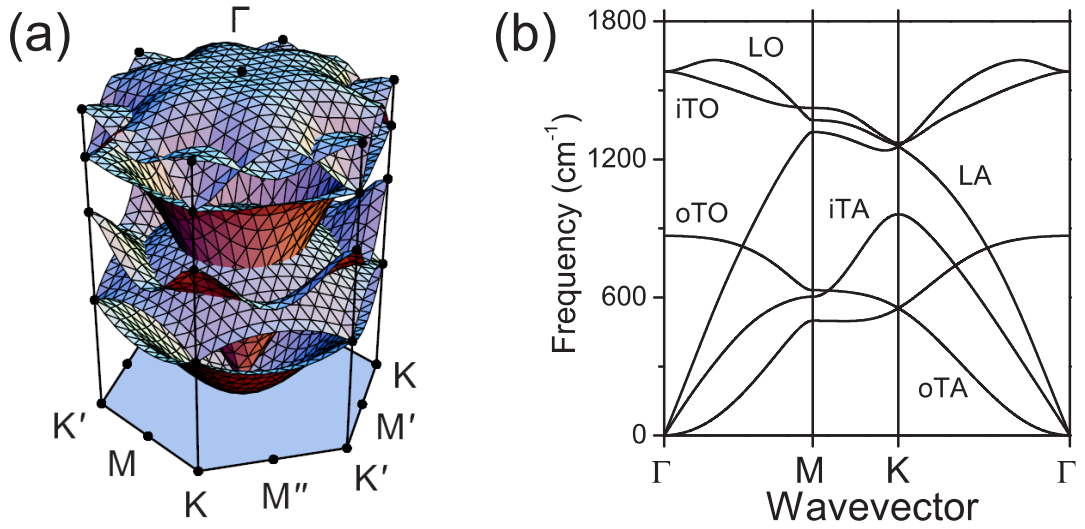

Figure 2.6: (a) Phonon dispersion of graphene over the entire Brillouin zone calculated by force constants method [20]. (b) Phonon dispersion of monolayer graphene in the high symmetric directions calculated by Popov and Lambin [27] using the tight-biding method. The phonon branches are labeled: out-of-plane transverse acoustic (oTA); in-plane transverse acoustic (iTA); longitudinal acoustic (LA); out-of-plane transverse optic (oTO); in-plane transverse optic (iTO); longitudinal optic (LO).

phonon dispersion in the high symmetric directions calculated by Popov and Lambin [27] using the tight-binding approach.

At the Γ point of monolayer graphene, the iTO and LO modes are double degenerated and correspond to the vibrations of the sublattice A against the sublattice B as shown in Fig. 2.7. According to group theory, the degenerated zone-center LO and iTO phonon modes belong to the two-dimensional representation E_{2g}, which is Raman active [20]. This mode can be seen in the Raman spectrum with frequency around $1582\,cm^{-1}$ and it is known as the G band. The G band is one of the most prominent feature in the Raman spectrum of graphene, as shown in Section 3.2.

For bilayer graphene, there are four atoms in the unit cell, and then, each phonon branch of monolayer graphene splits into two branches. The E_{2g} phonon mode of monolayer graphene splits into two double degenerated modes associated with the in-phase (IP) and out-of-phase (OP) displacements of the atoms in the two layers, that belong to the representations E_g and E_u of the D_{3d} point group, respectively [28]. The E_u mode is observable in the Infrared spectroscopy, while the E_g mode can be seen as one peak in the Raman spectrum (G band).

In some cases, the force constant and *ab initio* calculations do not describe properly

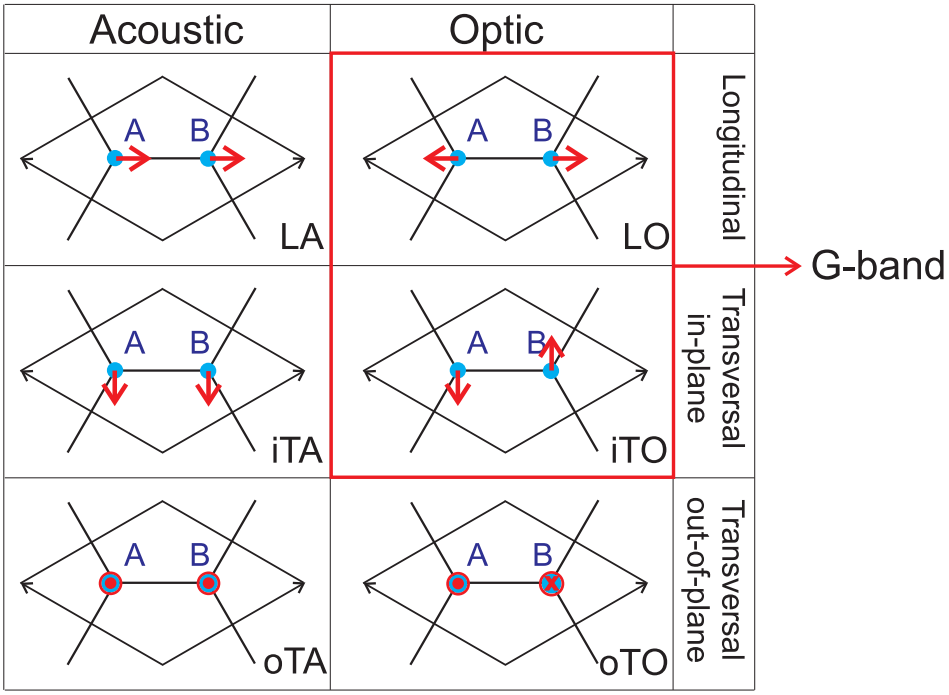

Figure 2.7: Vibrations of the two atoms of the unit cell of monolayer graphene that correspond to the six phonon branches at the Γ point. The double degenerated modes LO and iTO gives rise to the G band in the Raman spectrum.

the dispersion of the phonon modes. This is the case in graphene for the LO and iTO phonon branches around the Γ and K points, respectively. In these points, there is a strong electron-phonon coupling and a more carefull calculation must be done in order to correctly describe the behavior of the phonon modes. More details about the electron-phonon coupling will be given in the next section.

2.4 Electron-phonon interaction

We think of a metal as composed of a lattice of positively charged ions embedded in a sea of nearly free conduction electrons. We must suppose that in a vibrational wave in a metal the local variations in charge density due to the motion of the positively charged ions are screened by the motion of the conduction electrons (see Fig. 2.8). This influx of negative charge reduces the restoring force on the ions, and so the frequency of the oscillation is drastically reduced [1]. The residual electric field that was not screened by the electron gas acts on the electrons and that gives rise to the electron-phonon interaction. In this section we shall consider some of the consequences of the interaction of phonons

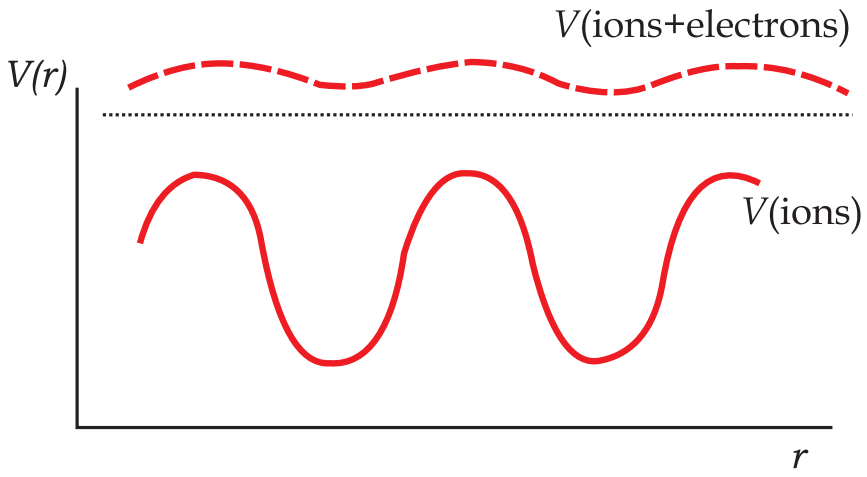

Figure 2.8: The deep potential due to the displacement of the ions by a phonon is screened by the flow of electrons.

with electrons.

2.4.1 The Fröhlich Hamiltonian

In this model we take for granted the concept of screening, and assume that the ions interact with each other and with the electrons only through a short-range screened potential (dashed line in Fig. 2.8), and we treat the electrons themselves as independent fermions. Also we neglect electron-electron interactions. For a Bravais lattice our unperturbed Hamiltonian, where the electrons and phonons are treated separately, is:

$$H_0 = \sum_{\mathbf{k}} \varepsilon_{\mathbf{k}} c^\dagger_{\mathbf{k}} c_{\mathbf{k}} + \sum_{\mathbf{q},\mathbf{s}} \hbar\omega_{\mathbf{q},\mathbf{s}} a^\dagger_{\mathbf{q},\mathbf{s}} a_{\mathbf{q},\mathbf{s}} \,, \tag{2.19}$$

where $c^\dagger_{\mathbf{k}}$ ($c_{\mathbf{k}}$) is the creation (annihilation) operator for the electrons with energy $\varepsilon_{\mathbf{k}}$ and momentum $\mathbf{k}$, and $a^\dagger_{\mathbf{q}}$ ($a_{\mathbf{q}}$) is the creation (annihilation) operator for the phonons with energy $\hbar\omega_{\mathbf{q}}$, momentum $\mathbf{q}$ and direction of polarization $\mathbf{s}$. If it happens that $\mathbf{s}$ is parallel to $\mathbf{q}$, we say that it is a longitudinally polarized phonons in the crystal. If $\mathbf{s}\cdot\mathbf{q} = 0$, the phonon is transversely polarized. To the unperturbed Hamiltonian, we add the interaction H_1 of the electrons with the screened ions:

$$H_1 = \sum_{\mathbf{k},\mathbf{k}',\mathbf{l}} \langle \mathbf{k}|V(\mathbf{r}-\mathbf{l}-\mathbf{y}_\mathbf{l})|\mathbf{k}'\rangle \, c^\dagger_{\mathbf{k}} c_{\mathbf{k}'} \,, \tag{2.20}$$

where $|\mathbf{k}\rangle$ and $|\mathbf{k}'\rangle$ are the initial and final electronic state, respectively. Here, we assume that at any point the potential $V(\mathbf{r}-\mathbf{l}-\mathbf{y}_\mathbf{l})$ due to a particular ion depends only on the

distance from the center of the ion, where $\mathbf{y_l}$ is the ion displacement from the equilibrium position $\mathbf{l}$. We can use the Fourier transform of the potencial, then:

$$V_{\mathbf{k}-\mathbf{k}'} = \Omega^{-1} \int e^{i(\mathbf{k}'-\mathbf{k})\cdot(\mathbf{l}+\mathbf{y_l})}\ V(\mathbf{r}-\mathbf{l}-\mathbf{y_l})\ d(\mathbf{l}+\mathbf{y_l}) \tag{2.21}$$

where Ω is the crystal volume, and we can rewrite Eq. 2.20 as:

$$H_1 = \sum_{\mathbf{k},\mathbf{k}',\mathbf{l}} e^{i(\mathbf{k}'-\mathbf{k})\cdot(\mathbf{l}+\mathbf{y_l})}\ V_{\mathbf{k}-\mathbf{k}'}\ c^\dagger_{\mathbf{k}} c_{\mathbf{k}'}\,. \tag{2.22}$$

If we assume that the displacement $\mathbf{y_l}$ of the ion is sufficiently small that $(\mathbf{k}'-\mathbf{k})\cdot\mathbf{y_l} \ll 1$, we have:

$$\begin{aligned} e^{i(\mathbf{k}'-\mathbf{k})\cdot\mathbf{y_l}} &\simeq 1 + i(\mathbf{k}'-\mathbf{k})\cdot\mathbf{y_l} && (2.23)\\ &= 1 + iN^{-1/2}(\mathbf{k}'-\mathbf{k})\cdot\sum_{\mathbf{q}} e^{i\mathbf{q}\cdot\mathbf{l}}\ \mathbf{y_q}\,, && (2.24)\end{aligned}$$

where $\mathbf{q} = \mathbf{k}-\mathbf{k}'$. Substituting Eq. 2.24 into Eq. 2.22, we can separate H_1 into two parts, $H_1 = H_{Bloch} + H_{el-ph}$. The first term

$$H_{Bloch} = \sum_{\mathbf{k},\mathbf{k}',\mathbf{l}} e^{i(\mathbf{k}'-\mathbf{k})\cdot\mathbf{l}}\ V_{\mathbf{k}-\mathbf{k}'}\ c^\dagger_{\mathbf{k}} c_{\mathbf{k}'} \tag{2.25}$$

is independent of the lattice displacements. The second term can be written as:

$$\begin{aligned} H_{el-ph} &= iN^{-1/2} \sum_{\mathbf{k},\mathbf{k}',\mathbf{l},\mathbf{q}} e^{i(\mathbf{k}'-\mathbf{k}+\mathbf{q})\cdot\mathbf{l}}\ (\mathbf{k}'-\mathbf{k})\cdot\mathbf{y_q}\ V_{\mathbf{k}-\mathbf{k}'}\ c^\dagger_{\mathbf{k}} c_{\mathbf{k}} && (2.26)\\ &= iN^{1/2} \sum_{\mathbf{k},\mathbf{k}'} (\mathbf{k}'-\mathbf{k})\cdot\mathbf{y}_{\mathbf{k}-\mathbf{k}'}\ V_{\mathbf{k}-\mathbf{k}'}\ c^\dagger_{\mathbf{k}} c_{\mathbf{k}'}\,. && (2.27)\end{aligned}$$

The displacement $\mathbf{y_q}$ can be written in the harmonic approximation as a function of the phonon creation and annihilation operators as:

$$\mathbf{y_q} = \sum_{\mathbf{s}} \sqrt{\frac{\hbar}{2M\omega_{\mathbf{q},\mathbf{s}}}}\ (a^\dagger_{-\mathbf{q},\mathbf{s}} + a_{\mathbf{q},\mathbf{s}})\mathbf{s}\,. \tag{2.28}$$

The H_{el-ph} then becomes:

$$H_{el-ph} = i \sum_{\mathbf{k},\mathbf{k}',\mathbf{s}} \sqrt{\frac{N\hbar}{2M\omega_{\mathbf{k}-\mathbf{k}',\mathbf{s}}}}\ (\mathbf{k}'-\mathbf{k})\cdot\mathbf{s}\ V_{\mathbf{k}-\mathbf{k}'}\ (a^\dagger_{\mathbf{k}'-\mathbf{k},\mathbf{s}} + a_{\mathbf{k}-\mathbf{k}',\mathbf{s}})\ c^\dagger_{\mathbf{k}} c_{\mathbf{k}'}\,. \tag{2.29}$$

For simplicity we shall assume the phonon spectrum to be isotropic, so that the phonons will be either longitudinally or transversely polarized. Then, only the longitudinal modes,

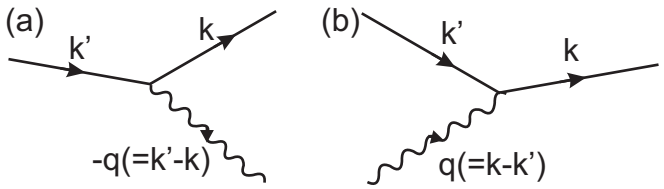

Figure 2.9: The Fröhlich Hamiltonian includes an interaction term in which an electron is scattered from $\mathbf{k}'$ to $\mathbf{k}$ with either (a) emission or (b) absorption of a phonon. In each case the total momentum is conserved.

for which $\mathbf{s}$ is parallel to $\mathbf{k}' - \mathbf{k}$, will enter H_{el-ph}. Also, since the H_{Bloch} is not dependent of the displacement, we shall neglect its effects for the electron-phonon interaction. With these simplifications we are left with the *Fröhlich Hamiltonian*:

$$H = \sum_{\mathbf{k}} \varepsilon_{\mathbf{k}} c^{\dagger}_{\mathbf{k}} c_{\mathbf{k}} + \sum_{\mathbf{q}} \hbar\omega_{\mathbf{q}} a^{\dagger}_{\mathbf{q}} a_{\mathbf{q}} + \sum_{\mathbf{k},\mathbf{k}'} M_{\mathbf{k},\mathbf{k}'} \left(a^{\dagger}_{-\mathbf{q}} + a_{\mathbf{q}}\right) c^{\dagger}_{\mathbf{k}} c_{\mathbf{k}'} \,, \tag{2.30}$$

where the electron-phonon matrix element is defined by:

$$M_{\mathbf{k},\mathbf{k}'} = i\sqrt{\frac{N\hbar}{2M\omega_{\mathbf{q}}}} \left|\mathbf{k}' - \mathbf{k}\right| V_{\mathbf{k}-\mathbf{k}'} \,. \tag{2.31}$$

The interaction H_{el-ph} can be considered as being composed of two parts - terms involving $a^{\dagger}_{-\mathbf{q}} c^{\dagger}_{\mathbf{k}} c_{\mathbf{k}'}$ and terms involving $a_{\mathbf{q}} c^{\dagger}_{\mathbf{k}} c_{\mathbf{k}'}$. These terms may be represented by the diagrams shown in Figs. 2.9(a) and (b), respectively. In the first diagram an electron is scattered from $\mathbf{k}'$ to $\mathbf{k}$ with the emission of a phonon with momentum $(\mathbf{k}' - \mathbf{k})$. The second diagram represents the electron being scattered from $\mathbf{k}'$ to $\mathbf{k}$ with the absorption of a phonon with momentum $(\mathbf{k} - \mathbf{k}')$.

2.4.2 Phonon frequencies and the Kohn anomaly

To calculate the effect of the electron-phonon interaction on the phonon spectrum, we may use perturbation theory to calculate the total energy ε of the system described by the Fröhlich Hamiltonian (Eq. 2.30) to second order in H_{el-ph}:

$$\varepsilon = \varepsilon_0 + \langle\Phi|H_{el-ph}|\Phi\rangle + \left\langle\Phi|H_{el-ph}(\varepsilon_0 - H_0)^{-1}H_{el-ph}|\Phi\right\rangle \,, \tag{2.32}$$

with $\varepsilon_0 = \varepsilon_{\mathbf{k}}\ c^{\dagger}_{\mathbf{k}} c_{\mathbf{k}} + \hbar\omega^0_{\mathbf{q}}\ a^{\dagger}_{\mathbf{q}} a_{\mathbf{q}}$ being the unperturbed energy of the state Φ having $n_{\mathbf{q}}$ phonons in the longitudinally polarized mode $\mathbf{q}$ and $n_{\mathbf{k}}$ electrons in state $\mathbf{k}$. Since the components of H_{el-ph} act on Φ either to destroy or create one phonon, the first-order term vanishes from this expression because the resulting wavefunction must be orthogonal to

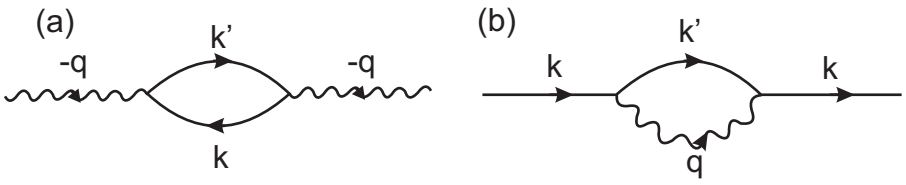

Figure 2.10: The Fröhlich Hamiltonian includes an interaction term in which an electron is scattered from $\mathbf{k}'$ to $\mathbf{k}$ with either (a) emission or (b) absorption of a phonon. In each case the total momentum is conserved.

Φ. In second order there is a set of nonvanishing terms, as the phonon destroyed by the first factor of H_{el-ph} to act on Φ can be replaced by the second factor of H_{el-ph}, and vice versa. We then find the contribution of the second-order terms ε_2 to be

$$\varepsilon_2 = \langle\Phi| \sum_{\mathbf{k},\mathbf{k}'} M_{\mathbf{k},\mathbf{k}'}(a^\dagger_{-\mathbf{q}} + a_{\mathbf{q}})\ c^\dagger_{\mathbf{k}} c_{\mathbf{k}'} (\varepsilon_0 - H_0)^{-1} \times \sum_{\mathbf{k}'',\mathbf{k}'''} M_{\mathbf{k}'',\mathbf{k}'''}(a^\dagger_{-\mathbf{q}'} + a_{\mathbf{q}'})\ c^\dagger_{\mathbf{k}''} c_{\mathbf{k}'''} |\Phi\rangle \tag{2.33}$$

$$= \langle\Phi| \sum_{\mathbf{k},\mathbf{k}'} |M_{\mathbf{k},\mathbf{k}'}|^2 \left[\frac{(a^\dagger_{-\mathbf{q}} a_{-\mathbf{q}})\ c^\dagger_{\mathbf{k}} c_{\mathbf{k}'}\ c^\dagger_{\mathbf{k}'} c_{\mathbf{k}}}{(\varepsilon_0 - H_0)} + \frac{(a_{\mathbf{q}} a^\dagger_{\mathbf{q}})\ c^\dagger_{\mathbf{k}} c_{\mathbf{k}'}\ c^\dagger_{\mathbf{k}'} c_{\mathbf{k}}}{(\varepsilon_0 - H_0)} \right] |\Phi\rangle\,, \tag{2.34}$$

all other terms having zero matrix element since the resulting wavefunction will be orthogonal to Φ. The first term in the brackets in Eq. 2.34 can be represented as in Fig. 2.10(a). An electron is first scattered from $\mathbf{k}$ to $\mathbf{k}'$ with the absorption of a phonon with momentum $-\mathbf{q} = \mathbf{k}' - \mathbf{k}$. The factor $(\varepsilon_0 - H_0)^{-1}$ measures the amount of time the electron is allowed by the Uncertainty Principle to stay in the intermediate state $\mathbf{k}'$ and can be written as the energy difference between the initial and intermediate states, $(\varepsilon_{\mathbf{k}} + \hbar\omega^0_{-\mathbf{q}} - \varepsilon_{\mathbf{k}'})^{-1}$. The electron is then scattered back into its original state with the re-emission of the phonon. We can represent the second term in Eq. 2.34 by Fig. 2.10(b), and then, we find an energy denominator of $\varepsilon_{\mathbf{k}} - \hbar\omega^0_{\mathbf{q}} - \varepsilon_{\mathbf{k}'}$.

We can write the creation and annihilation operators in terms of occupation numbers ($n_{\mathbf{k}}$ or $n_{\mathbf{q}}$). For fermions (electrons) we have:

$$c^\dagger_{\mathbf{k}} c_{\mathbf{k}} = n_{\mathbf{k}} \tag{2.35}$$

$$c_{\mathbf{k}} c^\dagger_{\mathbf{k}} = 1 - n_{\mathbf{k}}, \tag{2.36}$$

and for bosons (phonons):

$$a^\dagger_{\mathbf{q}} a_{\mathbf{q}} = n_{\mathbf{q}} \tag{2.37}$$

$$a_{\mathbf{q}} a^\dagger_{\mathbf{q}} = 1 + n_{\mathbf{q}}\,. \tag{2.38}$$

Rearranging the creation and annihilation operators in Eq. 2.34 into the form of number operators then gives:

$$\varepsilon_2 = \langle\Phi| \sum_{\mathbf{k},\mathbf{k}'} |M_{\mathbf{k},\mathbf{k}'}|^2 \left[\frac{n_{-\mathbf{q}}\ c^\dagger_{\mathbf{k}} c_{\mathbf{k}} (1-n_{\mathbf{k}'})}{(\varepsilon_{\mathbf{k}} - \varepsilon_{\mathbf{k}'} + \hbar\omega^0_{-\mathbf{q}})} + \frac{(1+n_{\mathbf{q}})\ c^\dagger_{\mathbf{k}} c_{\mathbf{k}} (1-n_{\mathbf{k}'})}{(\varepsilon_{\mathbf{k}} - \varepsilon_{\mathbf{k}'} - \hbar\omega^0_{\mathbf{q}})} \right] |\Phi\rangle \tag{2.39}$$

$$= \langle\Phi| \sum_{\mathbf{k},\mathbf{k}'} |M_{\mathbf{k},\mathbf{k}'}|^2 \left[\frac{n_{-\mathbf{q}} n_{\mathbf{k}} (1-n_{\mathbf{k}'})}{(\varepsilon_{\mathbf{k}} - \varepsilon_{\mathbf{k}'} + \hbar\omega^0_{-\mathbf{q}})} + \frac{(1+n_{\mathbf{q}}) n_{\mathbf{k}} (1-n_{\mathbf{k}'})}{(\varepsilon_{\mathbf{k}} - \varepsilon_{\mathbf{k}'} - \hbar\omega^0_{\mathbf{q}})} \right] |\Phi\rangle\,. \tag{2.40}$$

It may be assumed that $\omega_{\mathbf{q}} = \omega_{-\mathbf{q}}$, and hence that in equilibrium $\langle n_{\mathbf{q}}\rangle = \langle n_{-\mathbf{q}}\rangle$. Also, $\langle n_{\mathbf{q}} n_{\mathbf{k}} n_{\mathbf{k}'}\rangle = 0$ by symmetry. Then:

$$\varepsilon_2 = \sum_{\mathbf{k},\mathbf{k}'} |M_{\mathbf{k},\mathbf{k}'}|^2 \ \frac{\langle n_{\mathbf{q}} n_{\mathbf{k}}\rangle (\varepsilon_{\mathbf{k}} - \varepsilon_{\mathbf{k}'} - \hbar\omega^0_{\mathbf{q}}) \ + \ (\langle n_{\mathbf{k}}\rangle - \langle n_{\mathbf{k}} n_{\mathbf{k}'}\rangle + \langle n_{\mathbf{q}} n_{\mathbf{k}}\rangle)(\varepsilon_{\mathbf{k}} - \varepsilon_{\mathbf{k}'} + \hbar\omega^0_{\mathbf{q}})}{(\varepsilon_{\mathbf{k}} - \varepsilon_{\mathbf{k}'})^2 - (\hbar\omega^0_{\mathbf{q}})^2} \tag{2.41}$$

$$= \sum_{\mathbf{k},\mathbf{k}'} |M_{\mathbf{k},\mathbf{k}'}|^2 \ \frac{2\langle n_{\mathbf{q}} n_{\mathbf{k}}\rangle (\varepsilon_{\mathbf{k}} - \varepsilon_{\mathbf{k}'}) \ + \ (\langle n_{\mathbf{k}}\rangle - \langle n_{\mathbf{k}} n_{\mathbf{k}'}\rangle)(\varepsilon_{\mathbf{k}} - \varepsilon_{\mathbf{k}'} + \hbar\omega^0_{\mathbf{q}})}{(\varepsilon_{\mathbf{k}} - \varepsilon_{\mathbf{k}'})^2 - (\hbar\omega^0_{\mathbf{q}})^2}\,. \tag{2.42}$$

The total energy of the system is then given by:

$$\varepsilon = \hbar\omega^0_{\mathbf{q}} \langle n_{\mathbf{q}}\rangle + \sum_{\mathbf{k},\mathbf{k}'} |M_{\mathbf{k},\mathbf{k}'}|^2 \ \langle n_{\mathbf{k}}\rangle \left[\frac{2\langle n_{\mathbf{q}}\rangle (\varepsilon_{\mathbf{k}} - \varepsilon_{\mathbf{k}'})}{(\varepsilon_{\mathbf{k}} - \varepsilon_{\mathbf{k}'})^2 - (\hbar\omega^0_{\mathbf{q}})^2} + \frac{1 - \langle n_{\mathbf{k}'}\rangle}{(\varepsilon_{\mathbf{k}} - \varepsilon_{\mathbf{k}'} - \hbar\omega^0_{\mathbf{q}})} \right]. \tag{2.43}$$

The effect of the electron-phonon interaction on the phonon spectrum is contained in the term proportional to $\langle n_{\mathbf{q}}\rangle$ in Eq. 2.43. Now the perturbed phonon energy $\hbar\omega^p_{\mathbf{q}}$ is the energy required to increase $\langle n_{\mathbf{q}}\rangle$ by unit

$$\hbar\omega^p_{\mathbf{q}} = \frac{\partial\varepsilon}{\partial\langle n_{\mathbf{q}}\rangle} = \hbar\omega^0_{\mathbf{q}} + \sum_{\mathbf{k}} |M_{\mathbf{k},\mathbf{k}'}|^2 \ \frac{2\langle n_{\mathbf{k}}\rangle (\varepsilon_{\mathbf{k}} - \varepsilon_{\mathbf{k}'})}{(\varepsilon_{\mathbf{k}} - \varepsilon_{\mathbf{k}'})^2 - (\hbar\omega^0_{\mathbf{q}})^2}\,. \tag{2.44}$$

If we neglect the phonon energy in the denominator in comparison with the electron energies we have

$$\hbar\omega^p_{\mathbf{q}} = \hbar\omega^0_{\mathbf{q}} - \sum_{\mathbf{k}} 2|M_{\mathbf{k},\mathbf{k}'}|^2 \ \langle n_{\mathbf{k}}\rangle (\varepsilon_{\mathbf{k}'} - \varepsilon_{\mathbf{k}})^{-1}\,. \tag{2.45}$$

One may picture the origin of this change in phonon frequency by Fig. 2.10(a), in which the first interaction is represented as the creation of an electron-hole pair by the absorption of a phonon. One can then say that it is the fact that the phonon spends part of its lifetime (in the order of picoseconds) in the form of an electron-hole pair that modifies its energy.

One interesting consequence of Eq. 2.45 occurs in metals when $\mathbf{q}$ has a value close to the diameter of the Fermi surface $2k_F$. In this case, the states $\mathbf{k}$ and $\mathbf{k}' = \mathbf{k} - \mathbf{q}$

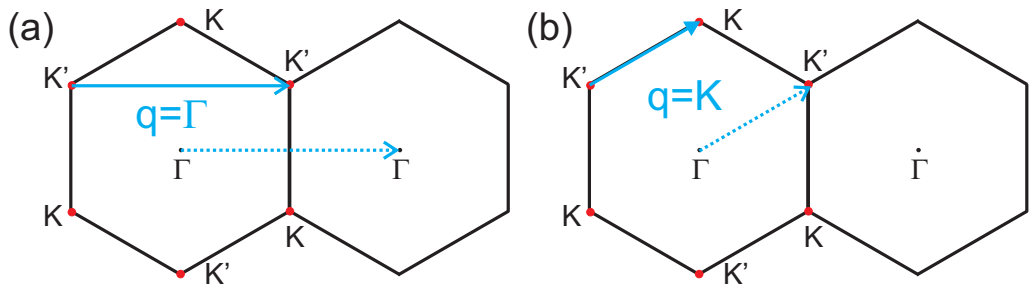

Figure 2.11: The two possible vector (a) $\mathbf{q} = \mathbf{\Gamma}$ and (b) $\mathbf{q} = \mathbf{K}$ that can connect two electronic states in the Fermi surface (red dots) in graphene.

are connected by $\mathbf{q}$ in the same Fermi surface. Evaluating $\partial\hbar\omega^p_{\mathbf{q}}/\partial\mathbf{q}$ and neglecting the variation of $M_{\mathbf{k},\mathbf{k}'}$ with $\mathbf{q}$, the electron-phonon interaction contributes an amount

$$2\sum_{\mathbf{k}} |M_{\mathbf{k},\mathbf{k}'}|^2 \ \langle n_{\mathbf{k}} \rangle \, (\varepsilon_{\mathbf{k}-\mathbf{q}} - \varepsilon_{\mathbf{k}})^{-2} \frac{\partial \varepsilon_{\mathbf{k}-\mathbf{q}}}{\partial \mathbf{q}} \,. \tag{2.46}$$

Here, $\varepsilon_{\mathbf{k}} = \hbar^2|\mathbf{k}|^2/2m$, $\varepsilon_{\mathbf{k}-\mathbf{q}} = \hbar^2|\mathbf{k}-\mathbf{q}|^2/2m$ and $|\mathbf{k}-\mathbf{q}|^2| = \mathbf{k}\cdot\mathbf{k} - 2\mathbf{k}\cdot\mathbf{q} + \mathbf{q}\cdot\mathbf{q}$. For simplicity, we can suppose that $\mathbf{q}$ is in the x-direction, so

$$(\varepsilon_{\mathbf{k}-\mathbf{q}} - \varepsilon_{\mathbf{k}}) = \frac{\hbar^2}{2m}(-2k_x q_x + q_x^2) = -\frac{\hbar^2}{m} q_x (2k_x - q_x) \,. \tag{2.47}$$

The differential in Eq. 2.46 is given by

$$\frac{\partial \varepsilon_{\mathbf{k}-\mathbf{q}}}{\partial \mathbf{q_x}} = -\frac{\hbar^2}{2m}(2k_x - 2q_x) \,. \tag{2.48}$$

Substituting Eqs. 2.47 and 2.48 into Eq. 2.46, we have

$$2\sum_{\mathbf{k}} |M_{\mathbf{k},\mathbf{k}-\mathbf{q}}|^2 \ \langle n_{\mathbf{k}} \rangle \left[\frac{-\hbar^2}{2m} q_x (2k_x - q_x)\right]^{-2} \ \frac{-\hbar^2}{2m}(2k_x - 2q_x) \tag{2.49}$$

$$= 2\sum_{\mathbf{k}} |M_{\mathbf{k},\mathbf{k}-\mathbf{q}}|^2 \ \langle n_{\mathbf{k}} \rangle \ \frac{1}{\frac{\hbar^2 q_x^2}{2m}} \left[\frac{(2k_x - q_x) - q_x}{(2k_x - q_x)^2}\right]$$

$$= 2\sum_{k=0}^{k_F} |M_{\mathbf{k},\mathbf{k}-\mathbf{q}}|^2 \ \langle n_{\mathbf{k}} \rangle \ \frac{1}{\frac{\hbar^2 q_x^2}{2m}} \left[\frac{1}{(2k_x - q_x)} - \frac{q_x}{(2k_x - q_x)^2}\right] \,. \tag{2.50}$$

When the summation is performed, we can see that the first term in Eq. 2.50 cause a logarithmic divergence, and thus a kink in the phonon dispersion is observed. This divergence when $q = 2k_F$ is the so-called *Kohn anomaly* [1].

For graphene, the Fermi surface is formed by the six K points. There are two possible phonon wavevectors that can connect two electronic states at the Fermi surface,

$\mathbf{q} = \mathbf{\Gamma}$ and for $\mathbf{q} = \mathbf{K}$, as shown in Figs. 2.11(a) and (b), respectively. In fact, Piscanec *et al.* [29] show that the Kohn anomaly occurs in graphene for the LO phonon mode around the Γ point of the Brillouin zone and for the iTO phonon mode around the K point. The Kohn anomaly gives rise to interesting effects in the Raman spectrum of monolayer and bilayer graphene and can be studied by changing the Fermi level of the system.

2.4.3 Effects of electron-phonon interaction in monolayer graphene

Now we should study the dependence of the phonon frequency as a function of the Fermi energy in the framework of non-adiabatic second order perturbation theory of the Fröhlich Hamiltonian. To do that, we can rewrite Eq. 2.44 in terms of the Fermi-Dirac distribution $f(\mathbf{k}) = \{exp[(\varepsilon_{\mathbf{k}} - E_F)/k_B T] + 1\}^{-1}$ instead of the electron occupation number. Then, we get [19]

$$\hbar\omega_{\mathbf{q}}^{p} - \hbar\omega_{\mathbf{q}}^{0} = \sum_{\mathbf{k}} \frac{2|M_{\mathbf{k},\mathbf{k}'}|^2}{\varepsilon_{\mathbf{k}} - \varepsilon_{\mathbf{k}'} + \hbar\omega_{\mathbf{q}}^{0} + i\gamma_{\mathbf{q}}} \times [f(\mathbf{k}) - f(\mathbf{k}')] \ . \tag{2.51}$$

The small damping factor $i\gamma_{\mathbf{q}}$ ($\gamma_{\mathbf{q}} \ll 1$) was introduced in the denominator in order to avoid the singular behavior of the function and is related to the phonon life time and with the line width of the spectrum. For a specific $\omega_{\mathbf{q}}$, the phonon energy correction $\Delta\omega_{\mathbf{q}}$ is given by $Re[\hbar\omega_{\mathbf{q}}^{p} - \hbar\omega_{\mathbf{q}}^{0}]$, *i.e.* the real part of Eq. 2.51. Likewise, the decay width correction $\Delta\gamma_{\mathbf{q}}$ is given by the imaginary part $Im[\hbar\omega_{\mathbf{q}}^{p} - \hbar\omega_{\mathbf{q}}^{0}]$ of Eq. 2.51 [19,30–32]. The real and the imaginary part of the Eq. 2.51 is given, respectively, by:

$$\Delta\omega_{\mathbf{q}} = Re\left[\hbar\omega_{\mathbf{q}}^{p} - \hbar\omega_{\mathbf{q}}^{0}\right] = Re\left[\sum_{\mathbf{k}} \frac{2|M_{\mathbf{k},\mathbf{k}'}|^2 \left[f(\mathbf{k}) - f(\mathbf{k}')\right]}{\varepsilon_{\mathbf{k}} - \varepsilon_{\mathbf{k}'} + \hbar\omega_{\mathbf{q}}^{0} + i\gamma_{\mathbf{q}}} \cdot \frac{\varepsilon_{\mathbf{k}} - \varepsilon_{\mathbf{k}'} + \hbar\omega_{\mathbf{q}}^{0} - i\gamma_{\mathbf{q}}}{\varepsilon_{\mathbf{k}} - \varepsilon_{\mathbf{k}'} + \hbar\omega_{\mathbf{q}}^{0} - i\gamma_{\mathbf{q}}}\right] , \tag{2.52}$$

$$= \sum_{\mathbf{k}} \frac{2|M_{\mathbf{k},\mathbf{k}'}|^2 (\varepsilon_{\mathbf{k}} - \varepsilon_{\mathbf{k}'} - \hbar\omega_{\mathbf{q}}^{0})}{(\varepsilon_{\mathbf{k}} - \varepsilon_{\mathbf{k}'} + \hbar\omega_{\mathbf{q}}^{0})^2 + \gamma_{\mathbf{q}}^2} \times [f(\mathbf{k}) - f(\mathbf{k}')] \ . \tag{2.53}$$

$$\Delta\gamma_{\mathbf{q}} = \sum_{\mathbf{k}} \frac{2|M_{\mathbf{k},\mathbf{k}'}|^2 \ \gamma_{\mathbf{q}}}{(\varepsilon_{\mathbf{k}} - \varepsilon_{\mathbf{k}'} + \hbar\omega_{\mathbf{q}}^{0})^2 + \gamma_{\mathbf{q}}^2} \times [f(\mathbf{k}) - f(\mathbf{k}')] \ . \tag{2.54}$$

The behavior of Eqs. 2.53 and 2.54 is shown in Fig. 2.12(b), where there is a resonance condition when the electron-hole pair energy matches the phonon energy. Also, the renormalization of the phonon energy and the line width is strongly dependent on the Fermi level position. Due to the Pauli exclusion principle (see Fig. 2.12(a)), when the Fermi

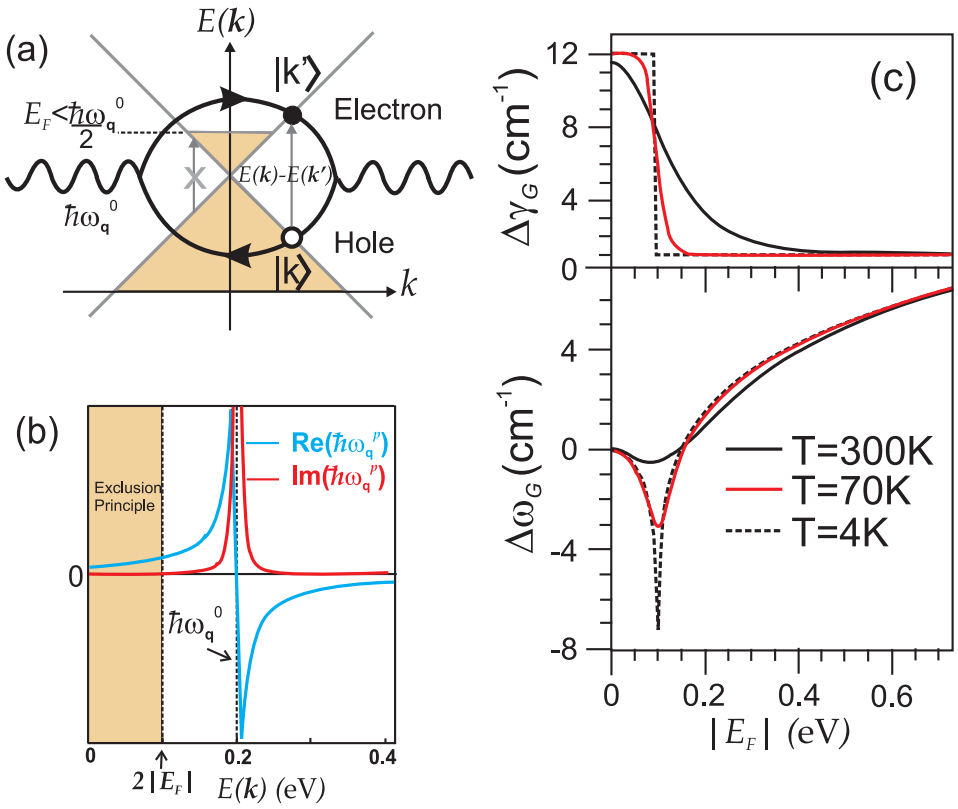

Figure 2.12: (a) Creation of a electron-hole pair by the absorption of a phonon with energy $\hbar\omega_{\mathbf{q}}^0$. Note that this process is forbidden by the Pauli exclusion principle if the Fermi energy is larger than the phonon energy. (b) Behavior of the real and the imaginary part of the phonon energy correction (Eq. 2.51). (c) The frequency $\Delta\omega_{\mathbf{G}}$ and line width $\Delta\gamma_{\mathbf{G}}$ corrections as a function of the Fermi energy and as a function of the temperature T for the G Raman band mode (adapted from [19]).

level is increased (or decreased), some electron-hole pairs are now forbidden to be created, and this affects the sum in Eqs. 2.53 and 2.54, which is performed in all the possible values of k that can create an electron-hole pair [1]. The colored region in Fig. 2.12(b) corresponds to the amount that will not be considered in the sum because of the Pauli exclusion principle.

We can evaluate Eq. 2.53 to check the dependency of the phonon energy correction with the Fermi energy. Since $\gamma_q \ll 1$, we can eliminate it from the denominator, and then, we have:

$$\Delta\omega_{\mathbf{q}} = \sum_{\mathbf{k}} \frac{2|M_{\mathbf{k},\mathbf{k}'}|^2}{\varepsilon_{\mathbf{k}} - \varepsilon_{\mathbf{k}'} + \hbar\omega_{\mathbf{q}}^0} \times [f(\mathbf{k}) - f(\mathbf{k}')] \ . \tag{2.55}$$

For monolayer graphene, the electronic dispersion is linear, $E = \hbar v_F k$, around the K point (see Section 2.2.1). Since the electron-hole pair is created by a vertical transition

(this is the case for the G band of graphene, see Section 3.2 for better explanation), $\varepsilon_{\mathbf{k}} = -\hbar v_F k$ and $\varepsilon_{\mathbf{k}'} = \hbar v_F k$. Considering that the electron-phonon matrix element does not depend on k, and substituting $\sum_{\mathbf{k}} \to \int_k d^2k = \int_0^{2\pi} \int_k k\ dk\ d\theta$ into the Eq. 2.55,

$$\Delta\omega_{\mathbf{q}} = 2|M_{\mathbf{k},\mathbf{k}'}|^2 \int_0^{2\pi} \int_k \frac{[f(\mathbf{k}) - f(\mathbf{k}')]}{-2\hbar v_F k + \hbar\omega^0_{\mathbf{q}}} k\ dk\ d\theta = 4\pi|M_{\mathbf{k},\mathbf{k}'}|^2 \int_0^k \frac{[f(\mathbf{k}) - f(\mathbf{k}')]}{-2\hbar v_F k + \hbar\omega^0_{\mathbf{q}}} k\ dk\,. \tag{2.56}$$

We can integrate over the energy instead of the wavevector, taking into account that $E = \hbar v_F k$, $dE = \hbar v_F dk$ and that the limits of integration for k $[0, k]$ becomes $[-E_F, E_F]$ for E. Also, for $T = 0$ we have

$$f(\mathbf{k}') = \begin{cases} 1, E < E_F \\ 0, E > E_F \end{cases} \quad , \quad f(\mathbf{k}) = \begin{cases} 0, E < E_F \\ 1, E > E_F \end{cases} \quad . \tag{2.57}$$

Then, Eq. 2.56 becomes

$$\Delta\omega_{\mathbf{q}} = \frac{4\pi|M_{\mathbf{k},\mathbf{k}'}|^2}{(\hbar v_F)^2} \int_{-|E_F|}^{|E_F|} \frac{E\ dE}{2E - \hbar\omega^0_{\mathbf{q}}}\,. \tag{2.58}$$

The phonon frequency renormalization is then, given by:

$$\Delta\omega_{\mathbf{q}} = \frac{4\pi|M_{\mathbf{k},\mathbf{k}'}|^2}{(\hbar v_F)^2} \left[|E_F| + \frac{\hbar\omega^0}{4} \ln\left(\frac{|E_F| - \frac{\hbar\omega^0}{2}}{|E_F| + \frac{\hbar\omega^0}{2}} \right) \right]. \tag{2.59}$$

We can see that the frequency correction shows a logarithmic divergence when the Fermi energy is equal to $\pm\hbar\omega^0_{\mathbf{q}}/2$, and, in the limit of large $|E_F|$, the phonon energy has dominantly a linear dependence on the Fermi energy, as shown in Fig. 2.12(c). The temperature also strongly affects the Kohn anomaly in $\pm\hbar\omega^0_{\mathbf{q}}/2$, which is smoothed as can be seen in the frequency and lifetime calculation shown Fig. 2.12(c) for three different temperatures. The Fermi level can be tuned by doping graphene with electrons or holes. Using a graphene device, we can move the Fermi level of the graphene by applying a gate voltage. Then, performing Raman measurements in a graphene device would be a easy way to probe the Kohn anomaly effect in those systems.

2.4.4 Effects of electron-phonon interaction in bilayer graphene

For AB stacked bilayer graphene, at $q = 0$ the E_{2g} phonon mode (G band) of monolayer graphene splits into two double degenerated modes, associated with the in-phase (E_g) and out-of-phase (E_u) displacements of the atoms in the two layers [28]. The E_u mode is not Raman active, but, as in monolayer graphene, the E_g mode can be seen

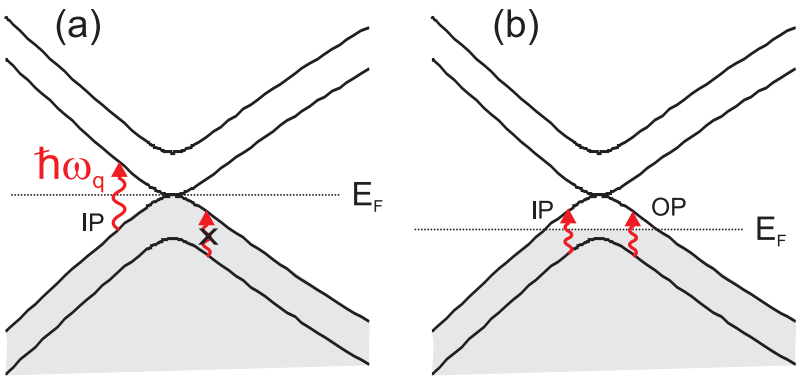

Figure 2.13: (a) When $E_F = 0$, only interband electron-hole pair creation by the absorption of a phonon is allowed. (b) When $E_F \neq 0$, intraband electron-hole pair creation by the absorption of a phonon are also allowed.

as one peak in the Raman spectrum, known as G band at $\sim 1582\,\mathrm{cm}^{-1}$. Moreover, since there are two valence (π_1 and π_2) and two conduction ($\pi_1^\star$ and $\pi_2^\star$) bands in this material, phonons can couple with electron-hole pairs produced by interband or intraband transitions. Interbands transitions are those were the hole is in the valence band and the electron in the conduction band. The intraband transitions occur when both the electron and the hole are in the conduction or in the valence band.

T. Ando [33] calculated the dependence of the self-energy for the in-phase (IP) and for the out-of-phase (OP) phonons as a function of Fermi energy. The phonon renormalization effect in bilayer graphene is understood by considering the selection rules for the interaction of the IP and OP phonon modes with the interband or intraband electron-hole pairs. The electron-phonon interaction can be described by a 2×2 matrix for each phonon symmetry given by [33]:

$$\Phi_{jj'}^{E_g}(k) = \frac{1}{2}\begin{pmatrix} \mathrm{sen}^2\psi & \cos^2\psi \\ \cos^2\psi & \mathrm{sen}^2\psi \end{pmatrix}, \quad \Phi_{jj'}^{E_u}(k) = \frac{1}{2}\begin{pmatrix} 0 & 1 \\ 1 & 0 \end{pmatrix}, \tag{2.60}$$

where each matrix element gives the contribution of electron-hole pairs involving different electronic sub-bands π_j or $\pi_j^\star$. The diagonal terms are responsible for the interband electron-phonon coupling, while the out-of-diagonal terms give the intraband coupling.

For the IP lattice vibration, all matrix elements are different from zero, and this phonon can interact with both interband or intraband electron-hole pairs (see Fig. 2.13). When $E_F = 0$, there is a couple of the phonon with the interband electron-hole pair, giving rise to the phonon energy renormalization. However, for the OP phonon mode, the diagonal terms of the matrix are null, showing that there is no electron-phonon interactions for interband transitions. Therefore, no Kohn anomaly is expected for the antisymmetric

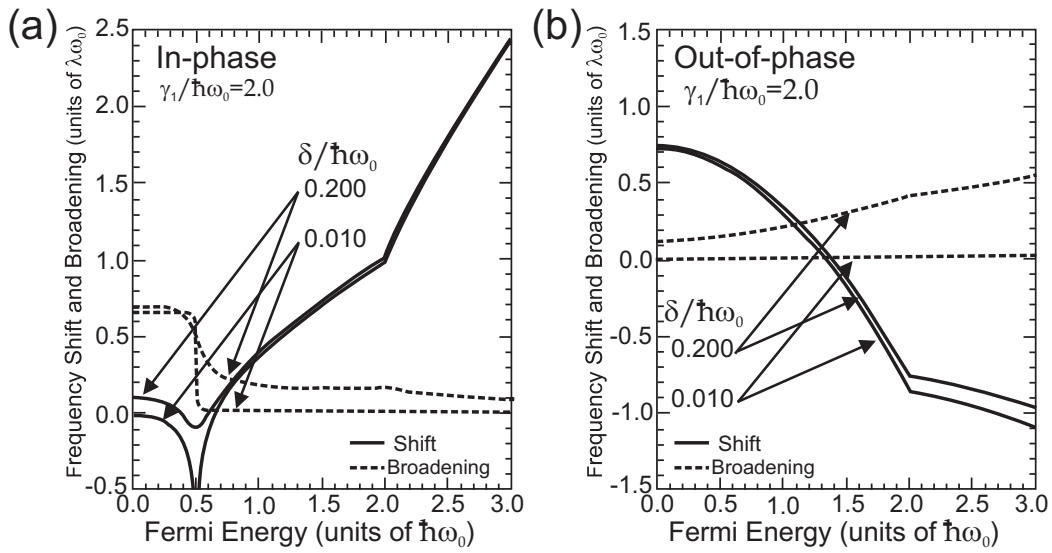

Figure 2.14: Calculated frequency shift (full lines) and broadening (dashed lines) for the (a) in-phase and (b) out-of-phase lattice vibrations of bilayer graphene as a function of the Fermi energy for two different values of crystal disorder δ. Figure adapted from Ref. [33].

phonon mode when the Fermi level is at the K point. The frequency of the out-of-phase vibration is, then, higher then the frequency of the in-phase vibration for $E_F = 0$.

If the Fermi energy is now moved away from the K point, the intraband electron-hole pairs can be produced by phonons (see Fig. 2.13). In this case, the OP phonons also have their energies renormalized, giving rise to the Kohn anomaly. Figs. 2.14(a) and (b) show, respectively, the frequency shift (solid lines) and the line width broadening (dashed lines) of the IP and OP phonon modes as a function of the Fermi energy calculated by T. Ando [33]. The δ parameter is due to disorder in the crystal. The frequency of the IP mode undergoes a hardening with increasing E_F and exhibit a logarithmic singularity at $E_F = \hbar\omega/2$, while a narrowing of the line width is observed. The renormalization for this phonon mode is analogous to the case of monolayer graphene. For the OP phonons, with the increase of E_F, the intraband transitions contributes now to the phonon self-energy, and the frequency of this mode gradually decreases, and a small broadening of the line width can be observed.

Special care must be taken to analyze the results for bilayer graphene electron-phonon coupling. The results showed in Figs. 2.14(a) and (b) are valid only if you change the Fermi level position but keep the inversion symmetry between the two layers. When there is an asymmetry between the two layers (for example, an electric field perpendicular to the layers induced by the application of an external gate voltage), the inversion symme-

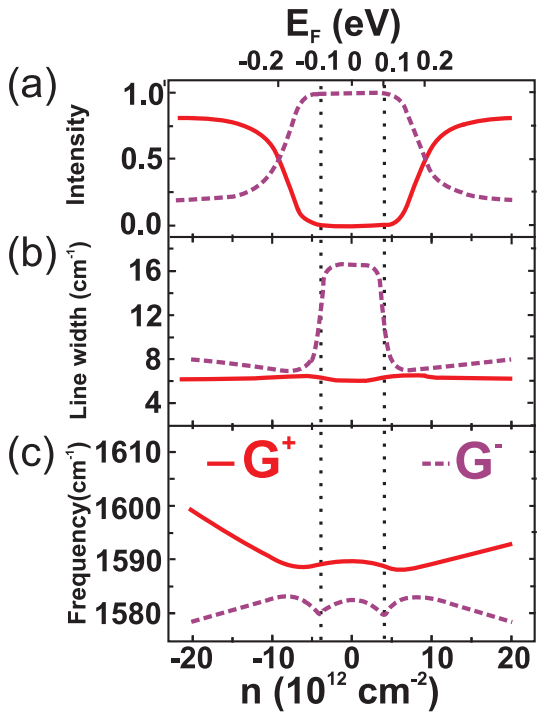

Figure 2.15: Inversion symmetry-breaking induced phonon mixing. Evolution of the G^+ (full lines) and G^- (dashed lines) (a) relative intensity, (b) line width and (c) frequency with carrier concentration and Fermi energy. The vertical dotted lines indicate a special position of the Fermi level, 0.1 eV, that corresponds to half of the G-band energy. Figure adapted from Ref. [36].

try of bilayer graphene is broken, lowering the symmetry of the system, that now belongs to the C_{3v} point group [34], and opening an electronic band gap at the K point. As a consequence, the in-phase and the out-of-phase lattice vibrations are no longer eigenstates os the system, but the resulting eigenstates can be regarded as superpositions of the IP and OP displacements [35,36]. Since the Raman active mode (in-phase) is now present in both resulting modes, there will be two peaks in the Raman spectrum: one with lower frequency G^- and another with higher frequency G^+.

The Raman spectrum can be quantitatively analyzed using a simple coupled-mode description [36]

$$\begin{vmatrix} E - E_{IP} & g \\ g & E - E_{OP} \end{vmatrix} = 0\,, \tag{2.61}$$

where $E_{IP} = \hbar\omega_{IP} - i\gamma_{IP}$, $E_{OP} = \hbar\omega_{OP} - i\gamma_{OP}$ (γ is the line width), and g is the coupling

between the IP-OP modes. Solutions to Eq. 2.61 are given by

$$E^{\pm} = \frac{E_{IP} + E_{OP}}{2} \pm \sqrt{\left(\frac{E_{IP} - E_{OP}}{2}\right)^2 + g^2}\,, \tag{2.62}$$

so that the real and imaginary parts of $E^{\pm}$, respectively, describe the energy and broadening of the G^+ and G^- modes. The behavior of the relative intensities, the width broadening and the frequency shift of the G^+ and G^- peaks as a function of the charge concentration and Fermi energy is shown in Figs. 2.15(a), (b) and (c), respectively [36]. The peak intensity is determined by the size of E_{IP} content within each mode. At $E_F = \pm 200\,\text{meV}$, the two peaks in the Raman spectrum have the same intensity as shown in Fig. 2.15(a) because the coupling partitions of the Raman active E_g mode is equally distributed to the G^+ and G^- peaks. Away from $E_F = \pm 200\,\text{meV}$, the relative intensities of the G^+ and G^- reverse, reflecting the fact that G^- (G^+) is dominated by the IP vibration at low (high) charge concentration.

Experimental results for the electron-phonon coupling in monolayer and bilayer graphene will be presented in Chapter 5.

Chapter 3

The Raman spectroscopy of graphene

The Raman spectrum of graphitic materials is known to be very sensitive to structural changes, making the Raman spectroscopy to be widely used in the past four decades for the characterization of these systems. Moreover, the physics behind the Raman spectrum of graphene is rich and can give us information about the electronic and vibrational structure, as well as the interactions about the electrons and phonons in the material. This chapter will start with a summary of the history of the Raman spectroscopy, followed by an overview of the first order and the double-resonance model, which successfully explains many features in the Raman spectra of monolayer and bilayer graphene.

3.1 Introduction of Raman Scattering

Light scattering is one of the most powerful tools for studying fundamental physics and material properties in condensed matter sciences. In the case the scattered light has the same frequency (wavelength) as the incident light, the process is elastic, and is known as Rayleigh scattering. If, however, after scattering, the light has a different frequency, the photon is then inelastically scattered, and a quantized excitation has been created or annihilated in the material and, in this case, the light scattering process is known as the Raman effect. It was discovered in 1928 by the Indian physicist Chandrasekhara Venkata Raman for which he was awarded the Nobel Prize in Physics in 1930. Nowadays, Raman spectroscopy is a widely used tool for characterization of liquids, gases, and solids, as well as for studying fundamental physics.

Fig. 3.1 shows the idea of Raman scattering of light as a tool for studying material

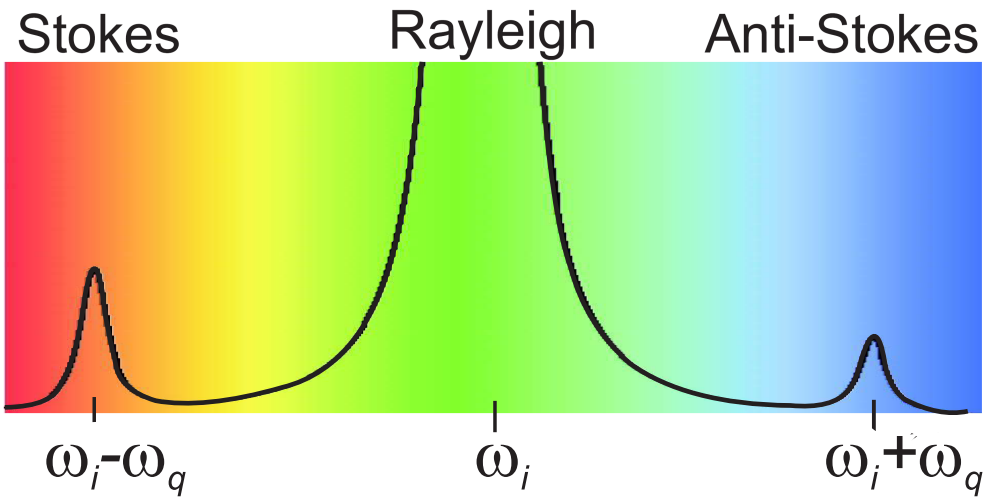

Figure 3.1: Schematics of the Raman spectrum where an incident light with frequency ω_i generates an elastically scattered light (Rayleigh) and two inelastically scattered components with frequency $\omega_i - \omega_q$ (Stokes) and $\omega_i + \omega_q$ (anti- Stokes).

properties. The incident laser light ω_i interacts with the material and creates a quantum excitation ω_q in the material system, the scattered light ω_s then has a different energy and line width from the incident photon. When the incident or scattered light coincides with the electronic gap of the material, we call this a resonant process. The energy difference between the incident ω_i and scattered photon is determined by the energy of the quantum excitation, which is a measurement of the intrinsic property of the material:

$$\omega_s = \omega_i - \omega_q \,. \tag{3.1}$$

This process is termed as the Stokes Raman scattering, where a phonon is created in the material, as illustrated in Fig. 3.1. Another possibility is that the laser light annihilates a phonon that was already in the material before the scattered light is emitted. In this case,

$$\omega_s = \omega_i + \omega_q \,, \tag{3.2}$$

and the process is known as the anti-Stokes Raman scattering. In this thesis, we will only consider the Stokes Raman scattering.

Two conservation laws must be obeyed during the Raman scattering. The first one is energy conservation which was just discussed above. The second one is momentum conservation. The selection rules associated with the momentum conservation in the anti-Stokes and Stokes one-phonon Raman are given by:

$$\mathbf{k}_s = \mathbf{k}_i \pm \mathbf{k}_q, \tag{3.3}$$

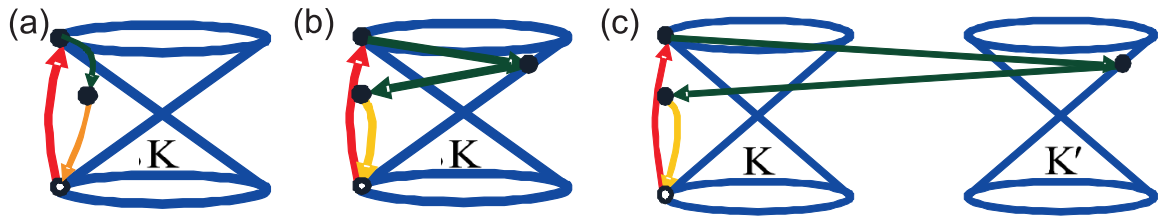

Figure 3.2: (a) First order Raman process that gives rise to the G band. Second order double resonance Raman processes involving (b) intravalley and (c) intervalley phonons.

where the ± signal stands for the anti-stokes and for the stoke scattering, respectively. In fact, these relations strongly restrict the wavevectors of phonons involved in the scattering process, as we will show below.

3.2 First order Raman scattering

The light we use in Raman scattering is typically visible or near infrared. It has a wavelength of thousands of $\mathring{A}$, which is 3 orders of magnitude larger than the unit cell size of graphene. The momentum of light is then negligible compared with the size of the Brillouin zone. Conservation of momentum then requires that the phonons have practically zero momentum. For first-order Raman scattering, this means that the only mode allowed would be the zone-center optical phonon. In a second-order Raman process, that will be explored in the next section, the phonons allowed include overtones and combinations, which are excitations with two phonons coming from the same or different phonon branch and having opposite momentum. The momentum of individual phonons may take any value.

The first order resonant Raman process can be understood as follows: a photon is absorbed by the material and excites an electron from the valence to the conduction band. The electron is then scattered by a phonon and then, recombines with the hole emitting a scattered photon. A schematics of this process can be seen in Fig. 3.2(a) for the stokes process, where the electron loses energy to create a phonon.

We now come to the phonon spectrum of graphene. Fig. 3.3 show the most prominent features in the Raman spectra of defect free monolayer graphene, the so called G band, appearing at $\sim 1582\,\mathrm{cm}^{-1}$, the G* and the G$'$ bands at about $2450\,\mathrm{cm}^{-1}$ and $2700\,\mathrm{cm}^{-1}$, respectively. In the case of a disordered or defective sample, we can also see the so-called D band, at about half of the frequency of the G$'$ band (around $1350\,\mathrm{cm}^{-1}$).

The G band of monolayer graphene is associated with the double degenerated (E_{2g})

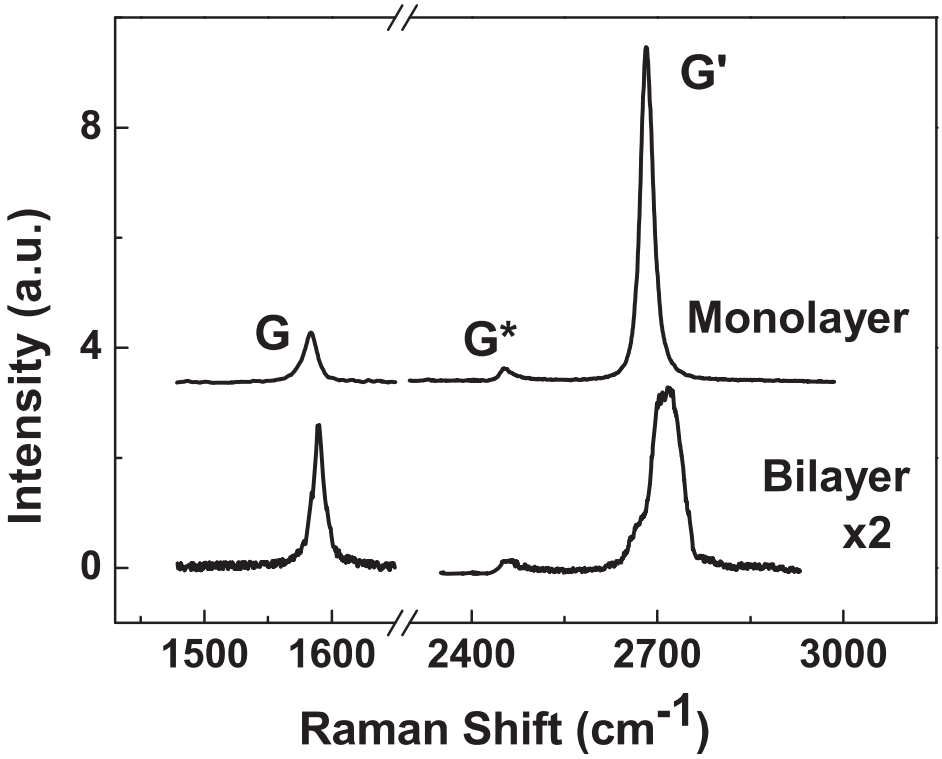

Figure 3.3: Typical Raman spectrum of defect free monolayer (upper) and bilayer (lower) graphene, showing the main Raman features G, G* and G$'$ bands.

zone-center phonon mode. The G band is the only first order feature Raman active in graphene systems. As seen in Section 2.3, the E_{2g} zone-center phonon mode is composed by the LO and iTO phonon branches. In bilayer graphene, there are now two valence and two conduction bands. Also, the E_{2g} mode splits into E_g and E_u mode. However, only the E_g mode is Raman active and the G band of bilayer graphene is still composed of one peak.

3.3 Second order Raman scattering and the double resonance process

The G* and the G$'$ bands originate from a second-order Raman process. The G* peaks is asymmetric and is composed of two peaks, one involving two iTO phonons with $q \sim 0$ (measured from the K point) and the other involving one LA and one iTO phonons with $q \approx 2k$ (also measured from the K point). The G$'$ band involves two iTO phonons near the K point with $q \approx 2k$. Check Fig. 3.4(a) for distinction between the processes

with $q \sim 0$ (processes (1) and (2)) and $q \sim 2k$ (processes (3) and (4)).

Both the iTO+LA from the G* and the G$'$ peaks exhibit a dispersive behavior, *i.e.*, their frequencies in the Raman spectra change as a function of the laser excitation energy E_L. The G$'$ frequency $\omega_{G'}$ upshifts with increasing E_L in a linear way over the visible range, with slope $(\partial\omega_{G'}/\partial E_L)$ around $100\,\mathrm{cm}^{-1}/\mathrm{eV}$ [17]. On the other hand, the iTO+LA mode of the G* band downshift with increasing the laser excitation energy, and its slope $(\partial\omega_{G^\star}/\partial E_L)$ is about $-16\,\mathrm{cm}^{-1}/\mathrm{eV}$ [37].

The dispersive behavior of the frequency of the $q \approx 2k$ bands originates from a double resonance Raman (DRR) process [38–40]. The double resonance process, shown in Figs. 3.2(b) and (c), begins with an electron of wavevector $\mathbf{k}$, measured from the K point, absorbing a photon of energy E_L. The electron is inelastically scattered by a phonon of wavevector $\mathbf{q}$ and energy E_{ph} to a point around the K' point, with momentum $\mathbf{k}'$ measured from K'. The electron is then scattered back to the $\mathbf{k}$ state, and emits a photon by recombining with a hole. The DRR mechanism can be an intervalley process, when it connects states around inequivalent K and K' points in the first Brillouin zone of graphene, as shown in Fig. 3.2(c), and this is the case for both G* and the G$'$ bands. There is also the possibility of an intravalley process, where the scattering of the electron by the phonon connects two points belonging to the same K point, as shown in Fig. 3.2(b) [39].

When E_L is increased, the resonance for the $\mathbf{k}$ vector of the electron moves away from the K point. In the DRR process, the corresponding $\mathbf{q}$ vector for the phonon increases with increasing $\mathbf{k}$. Thus by changing the laser energy, we can probe the phonon dispersion relation (ω versus $\mathbf{q}$). This effect is obtained experimentally from the dispersion of the phonon energy as a function of E_L [17]. A tunable laser system can directly show this dispersive behavior for the G* and the G$'$ bands in the Raman spectrum.

Since the monolayer graphene has only one conduction and one valence band, there is just one possible scattering process to give rise to the G$'$ band (the process shown in Fig. 3.2(c)), and then, the G$'$ band of the monolayer graphene is composed of only one peak.

In the case of AB stacked bilayer graphene, there are two valence and two conduction bands and the phonon branches split also affected by the interlayer interaction. Then, in the case of bilayer graphene, the DRR conditions involve more combinations than in the case of monolayer graphene, where there is only one main contribution to the G$'$ band.

Fig. 3.5 shows a schematic view of the bilayer graphene electronic structure where the upper (lower) and lower (upper) branches in the valence (conduction) band are labeled as π_1 ($\pi_1^\star$) and π_2 ($\pi_2^\star$), respectively. The major steps of the DRR process occur along

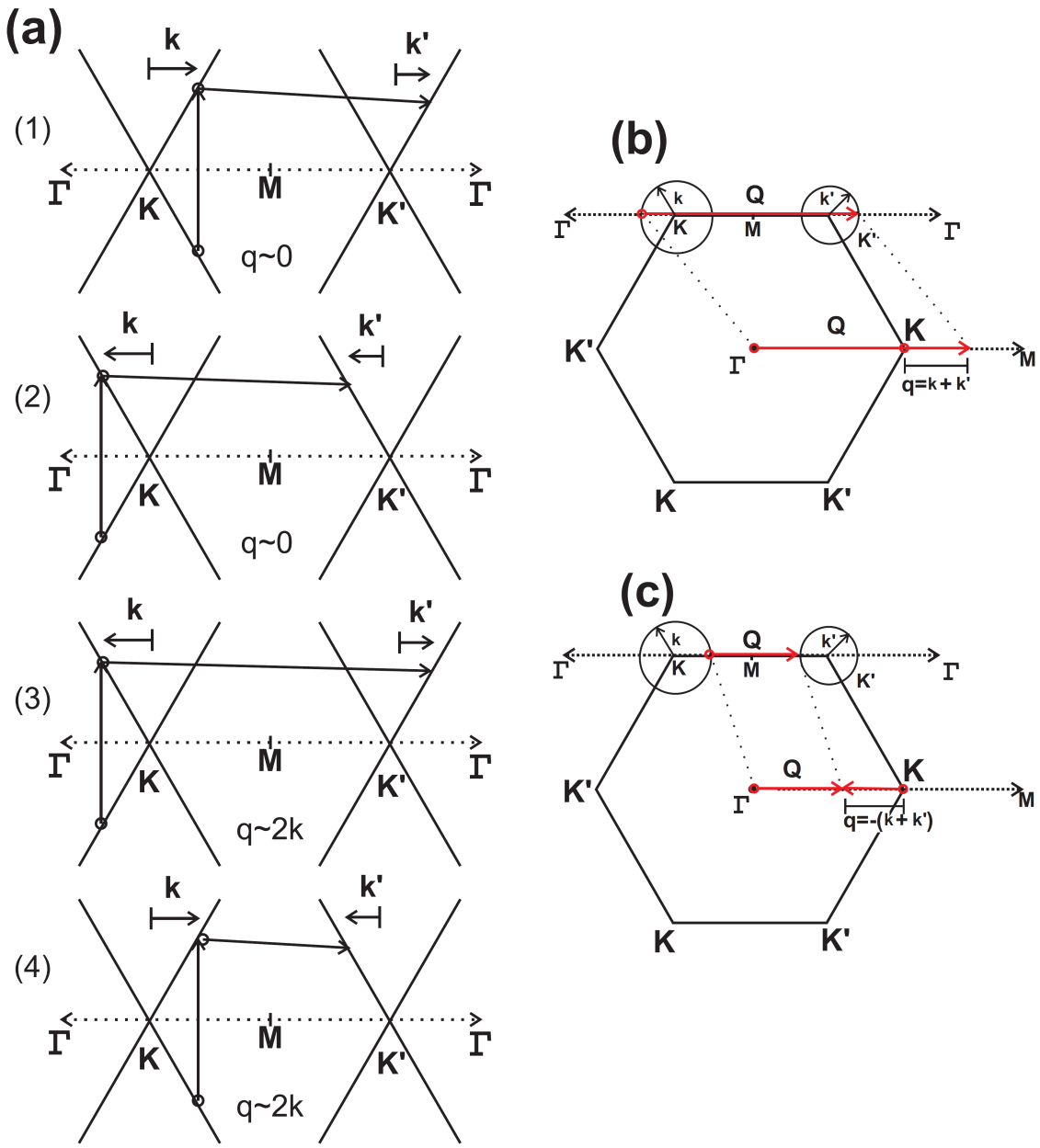

Figure 3.4: (a) The four processes along the high symmetric ΓKM line that can generate the double resonance Raman bands in monolayer graphene. (b) Top view of the process (3) in the first Brillouin zone, that involves phonon wavevector $\mathbf{q}$ along the KM direction. (c) Top view of the process (4) involving $\mathbf{q}$ along the ΓK direction.

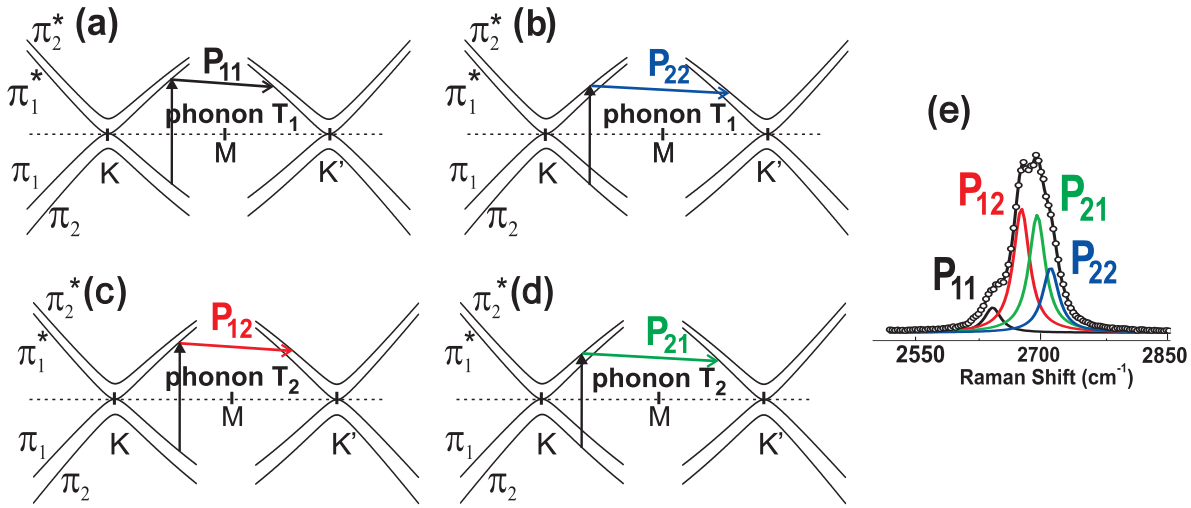

Figure 3.5: Schematic view of the electron dispersion of bilayer graphene near the K and K' points showing π_1 and π_2 valence bands and $\pi_1^\star$ and $\pi_2^\star$ conduction bands. The four DRR processes are indicated: (a) process P_{11}, (b) process P_{22}, (c) process P_{12}, and (d) process P_{21}. The phonon symmetries are also indicated in each process. (e) Measured G′ Raman band of bilayer graphene for 2.41 eV laser energy and fitted with four Lorentzians, each one corresponding to one of the possible process.

the T axis (ΓK) along which the π_2 and $\pi_1^\star$ bands belong to the T_1 totally symmetric irreducible representation, while the π_1 and $\pi_2^\star$ bands have odd T_2 symmetry relative to the inversion symmetry [28]. Now, for computing the number of resonant conditions involved in the DRR process, we are left with electrons in only two excited electronic states with **k** vectors near the K point which will be scattered by a phonon to an electronic state with wavevectors near the K' point. This electron-phonon scattering can now occur involving phonon with two symmetries T_1 and T_2. For the case of a T_1 phonon and the electron can be scattered to bands with the same symmetry, *i.e.*, $\pi_1^\star \rightarrow \pi_1^\star$ and $\pi_2^\star \rightarrow \pi_2^\star$. On the other hand, the T_2 phonon will connect electronic bands with different symmetry, *i.e.*, $\pi_1^\star \rightarrow \pi_2^\star$ and $\pi_2^\star \rightarrow \pi_1^\star$ [28].

These four different P_{ij} processes are depicted in Figs. 3.5(a)-(d), where i (j) denote the electron scattered from (to) each conduction band $\pi^\star_{i(j)}$. Processes P_{11} and P_{22} come from an iTO phonon with T_1 symmetry, while processes P_{12} and P_{21} come from an iTO phonon with T_2 symmetry. These four different scattering processes give rise to four Raman peaks in the G′ spectrum. Fig. 3.5(e) shows the Raman spectra of a bilayer graphene sample fitted with four Lorentzians with a decay line width of $\sim 25\,\mathrm{cm}^{-1}$ for each peak.

This is an interesting point that shows that the Raman spectroscopy is a powerful

and fast technique to identify the number of layers in a sample, since the shape of the G′ band depends on the number of layers of the sample [41]. It is important to notice that the identification of the number of layers by Raman spectroscopy is well established only for graphene samples with AB Bernal stacking. Graphene samples made by the mechanical exfoliation of natural or HOPG graphite leads to graphene flakes that have predominantly AB stacking, but this is not necessarily the case for graphene samples made by other growth methods [16].

3.4 Raman instrumentation

Two different comercial triple-monochromator spectrometers were used in this thesis: a Dilor XY system and a Horiba Jobin-Ivon T64000 system, both of them equipped with a N_2 cooled Charge Coupled Device (CCD) detector (the CCD needs a temperature of -140 ^{o}C to properly work), working in the backscattering configuration. The CCD can be understood as a large area of silicon photodiodes that form a bi-dimensional array of pixels. Through the photoelectric effect, the photodiodes convert photons into photoelectrons that are electronically processed. Each pixel delivers information compatible with the numbers of counts in it.

These equipments can also be used in two modes: single- or triple-monochromator. In the monochromator system, the incoming beam is reflected by the planar mirror (PM) 1 toward the spherical mirror (SM) 1 which reflects the beam toward the grating (Gr). As shown in Fig. 3.6(a) each grating is in connection with other four mirrors. Next, the grating opens the beam's spectrum and part of a previously selected spectral range is focused by the SM2 into the monochromator exit slit. It is necessary an edge or notch filter in order to eliminate the Rayleigh scattering when the single-monochromator is used.

In a triple-monochromator, two of these monochromators are coupled to form the foremonochromator (see Fig. 3.6(b)) and the last monochromator forms the spectrograph. The foremonochromator can work in an additive or subtractive mode. In the subtractive mode, which is the one used in this work, the incoming beam reaches the Gr1 and this grating disperses the beam in a way that just a selected range of frequency (or, equivalently, wavelength) undergoes the slit 2 (S2). The range of frequencies depends on the grating position which can be conveniently chosen. Besides selecting a spectral frequency range, the slit S2 basically prevents the Rayleigh component of the light from propagating into the detection system. Next, the beam is focused by the grating Gr2 before undergoing the slit 3 (S3). Finally, it arrives at the spectrograph. Inside the spectrograph,

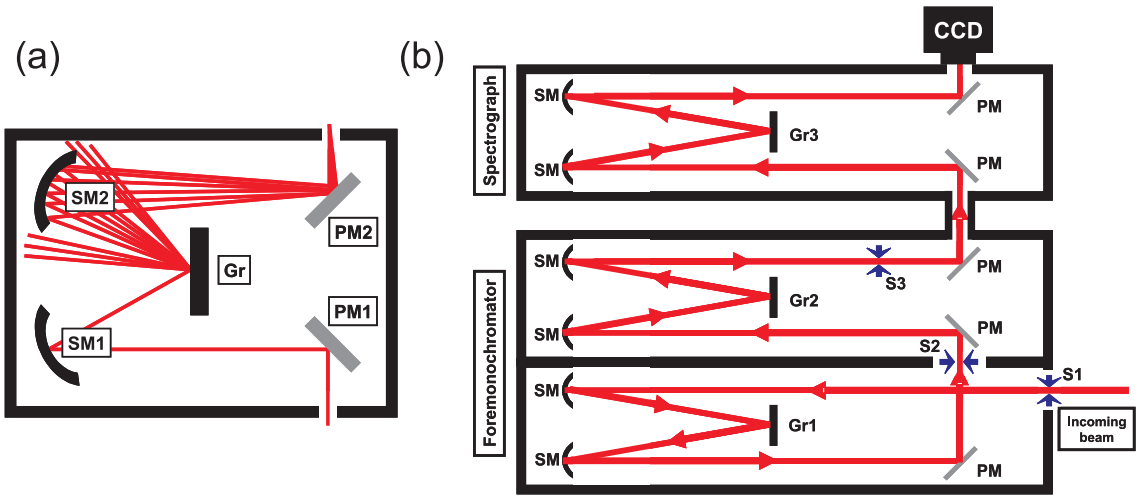

Figure 3.6: (a) In a monochromator scheme a grating (Gr) is geometrically connected to two spherical mirrors (SM1 and SM2) and two planar mirrors (PM1 and PM2). (b) The triple-monochromator is composed of a foremonochromator and a spectrograph. The foremonochromator is composed of two gratings that work harmonically in a configuration that basically filter the Rayleigh component and select a specific spectral range. The other grating composes the spectrograph where the beam is dispersed and reach a set of CCD's pixels.

the beam is dispersed by the grating Gr3. This dispersion covers a complete set of the CCDs pixels. In a triple-monochromator, the three gratings can be rotated simultaneously by a sine arm in order to chose the range of frequencies that will be covered by the CCD's pixels. Also, it is possible to measure Raman bands much closer to the Rayleigh light when compared to the single-monochromator mode. However the biggest problem of triple-monocromator is that the light intensity is reduced by a factor of 5-10 when compared to the monochromator due to the additional gratings.

In most cases, an Argon-Krypton ion laser was used to excite the Raman spectra. The laser emission has several intense discrete lines, with the wavelengths at 647.1 nm, 568.2 nm, 528.7 nm, 520 nm, 514.5 nm, 501.7 nm, 496.5 nm, 488.0 nm, 476.5 nm, 472.7 nm, 465.8 nm and 457.9 nm. A Titanium-Sapphire laser from Los Alamos National Laboratory (Los Alamos, New Mexico - USA) was also used. It is a continuous laser source ranging from 730 to 900 nm. This continuous laser system requires a high power laser to pump it, and for that we have used an Argon laser with ~ 6 W power.

Chapter 4

Graphene and device fabrication

In this chapter we discuss the experimental methods which were used in this work. Here, we describe the equipments and techniques used to prepare graphene samples and to fabricate these raw materials into the field-effect transistors studied in subsequent chapters.

4.1 Sample preparation

There are several known methods of producing graphene. The first method employed, and the one still widely used by the research community, is mechanical exfoliation [42]. The most recently developed method, and perhaps the most promising in prospects of scalability, is chemical vapor deposition [7,43,44], where the heat is used to break apart gas phase molecules and to reassemble these molecular components into a solid form. Usually, a catalyst film is used to enhance the breakdown of carbon gases beyond that possible with heat alone, and to act as a template for the self-assembly of carbon atoms into graphene.

Another possible graphene fabrication method is the annealing of SiC [45]. When a crystal of this material is annealed under the right conditions, the Si atoms will evaporate leaving behind a carbon-rich surface. The carbon atoms will self-assemble into graphene sheets, guided by lattice matching with the SiC surface. Also, there is the graphene oxide method [46], in which a chemical treatment is used to oxidize the graphite. The layers are then dispersed in water, and are carried off in dispersion. This solution may be filtered or cast onto a substrate to recover the graphene oxide material. Treatment with reducing chemical agents recovers much of the graphene to its original form.

From all of these methods, the mechanical exfoliation give us the highest quality

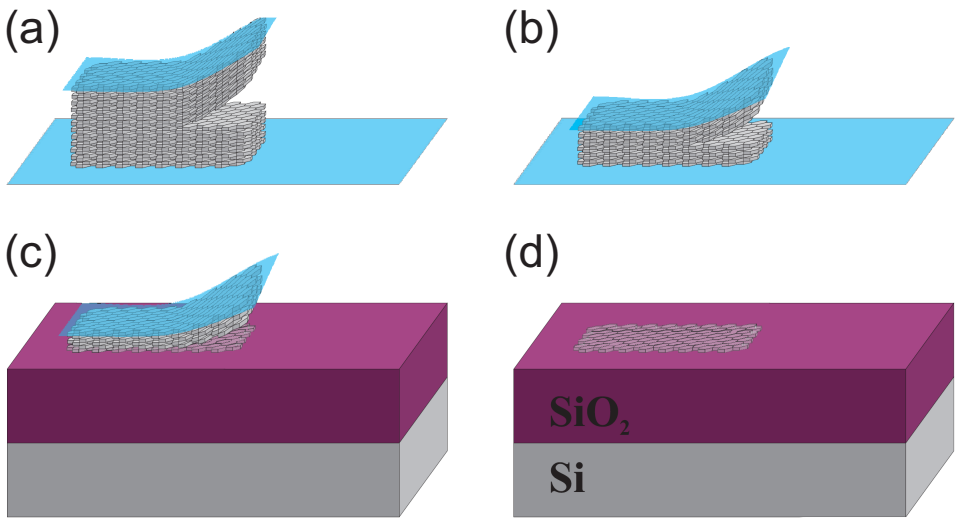

Figure 4.1: Mechanical cleavage of graphite into graphene using a scotch tape. After successively exfoliation, the graphene is then deposited on a silicon substrate.

graphene sheet (the quality is determined primarily by the starting material). Since we are interested in the basic properties of graphene, this is the method of fabrication used in this thesis, and will be discussed in detail below.

4.1.1 Mechanical exfoliation

The mechanical exfoliation of graphite is possible due to the weak van der Waals interlayer coupling in layered materials like graphite [5]. By using a scotch tape it is possible to separate the graphite layers until you reach only one layer of graphene. This technique is exemplified in Fig. 4.1, where a thick piece of natural graphite is successively cleaved using a scotch tape and then deposited on a silicon/silicon dioxide substrate. Although being only one atom thick, contrast in the optical microscope is possible because the presence of the graphene changes the interference condition for light passing through the silicon dioxide and reflecting off the silicon [42,47]. The scotch tape used here was the Medium Tack Blue from the Semiconductor Equipment Corporation, USA, and the graphite was from the Nacional de Grafite Ltda., Brazil.

In our experiments we have used a p-doped silicon wafers covered with silicon dioxide of thickness 300 nm. It is important that the substrate is clean before the deposition, so that the graphene can adhere more to the surface of the substrate, yielding larger graphene flakes. The silicon chips are rinsed with acetone for 30 seconds, then immediately rinsed with isopropanol (IPA) for another 30 seconds, then immediately blown dry from

above with nitrogen. For a better cleaning, the substrate can be exposed to an oxygen plasma or to an UV-ozone camera (a small concentration of ozone gas generated by an ultraviolet lamp) for about 10 minutes. After the deposition, optical inspection in the optical microscope is performed over the substrate to localize the graphene flakes. The number of layers of the flake is confirmed by Raman spectroscopy as described in Section 3.3 [41].

4.1.2 Lithography

After the flakes identifications, the fabrication of electronic devices from graphene draws strongly from conventional silicon processing and microfabrication. The first part of the device fabrication consists of doing the lithography, in which a beam exposes a resist that has been coated onto the surface. Immersion of the resist in a developing solution causes the pattern to be revealed in a manner depending on the type of resist used. I have used two types of lithography for the device patterning in this work. During my period in Universidade Federal de Minas Gerais (UFMG), the optical lithography was used, while the e-beam lithography was used when I was at Massachusetts Institute of Technology (MIT). The two processes are described below as used in this work.

Optical Lithography

For the optical lithography, a photosensitive resist is deposited over the substrate and exposed by an ultraviolet light. The resist used here was the S1805 positive resist (areas exposed to the optical beam develop away and are removed). S1813 can also be used with the same parameters described here. The resist is spun in the substrate using two steps in the spin-coater: the first one with 1000 rpm spinning speed for 5 seconds, and the second one with 8000 rpm for 40 seconds. The samples are then baked at 115 ^{o}C for 90 seconds. With these parameters, the thickness of the resulting deposited resist is $\sim$ 500 nm.

The pattern was drawn using a Microtech Laser Writter LW405. This machine has two light sources: one with 653 nm wavelength that does not expose the resist and is used to locate the flakes or marks that will be used in the lithography, and another one with 405 nm wavelength that is responsible for the exposure. The dose for this thickness of resist is 80 units of gain. After exposure, the samples are developed in MF-321 for 25 seconds. A post-development rinse by deionized water for 30 seconds is followed by blowing the chip dry with nitrogen.

E-Beam Lithography

Similar to the optical lithography, the e-beam lithography reproduces an image in a resist, but the exposure element is no longer ultraviolet light. In this case, an electron beam from an Scanning Electron Microscope (SEM) column is scanned across a surface in a pattern defined by a software file. There are two common resists: the first is the poly(methyl methacrylate) (PMMA), that is a positive resist; the second is the hydrogen silsesquioxane (HSQ), which is a negative resist (areas not exposed to the electron beam develop away and are removed). The resist used in this work was exclusively a 4% by weight solution of 996,000 molecular weight PMMA in anisole solvent.

First, the substrate to be coated is annealed at 175 ^{o}C for 5-10 minutes in order to remove surface adsorbates (mostly water). Then the substrate is transferred to a spin-coater and a bead of resist is deposited on the substrate using a pipette. The chip is accelerated quickly ($\sim$ 5000 rpm/s) to the spinning speed of 4000 rpm where it remains for 60 seconds. These values give a resist thickness of $\sim$ 200 nm. After the spin-coater comes to a stop, the sample is removed and baked on a hotplate at 175 ^{o}C for 5 minutes.

Exposure of PMMA by electron beam was performed at 10 keV accelerating voltage using a JEOL 5910 SEM machine. The lithography aspect is controlled by a separate computer equipped with a commercial lithography-enabling system called NPGS. At this accelerating voltage and for the development procedure described below, a 200 nm PMMA film was found to have an optimum exposure dose of 150 μC/cm^2. Development was performed in a solution of 2 parts IPA and 1 part methyl isobutyl ketone (MIBK). The sample is immersed in this solution for 20 seconds and immediately removed and rinsed with IPA from a squirt bottle for 20 seconds. The sample is then blown dry from above with compressed nitrogen.

4.1.3 Metal evaporation

After the lithography, metal is evaporated on the substrate to make the device contacts. Three techniques are commonly used to deposite metals to a surface: thermal (or resistive) evaporation, e-beam evaporation and sputtering. In the evaporation processes (both thermal and e-beam), the substrate is placed inside a vacuum chamber, in which a block of the material (source) to be deposited is also located. The source material is then heated to the point where it starts to boil and evaporate. The vacuum is required to allow the molecules to evaporate freely in the chamber, and they subsequently condense on all surfaces. Only the method used to heat (evaporate) the source material differs from

the thermal to the e-beam evaporation. In thermal evaporation, a boat containing the source material is heated electrically with a high current to make the material evaporate. In e-beam evaporation, an electron beam is aimed at the source material causing local heating and evaporation.

On the other hand, sputtering is a deposition technique in which the material is released from the source at much lower temperature than evaporation. The substrate is placed in a vacuum chamber with the source material, named a target, and an inert gas (such as argon) is introduced at low pressure. A gas plasma is struck using an radio-frequency (RF) power source, causing the gas to become ionized. The ions are accelerated towards the surface of the target, causing atoms of the source material to break off from the target in vapor form and condense on all surfaces including the substrate.

In this thesis, we have used the thermal evaporation to deposit 5 nm of chromium (Cr) and 80 nm of gold (Au). The Cr is necessary to guarantee the adhesion of the metals to the substrate. Liftoff of the resist after metal evaporation is accomplished by immersion of the substrate in acetone at 50 ^{o}C until the metal is removed, followed by rinses of acetone for 10 seconds and IPA for 10 seconds. The sample is then blown dry for 10 seconds with compressed nitrogen.

Usually, liftoff of both photoresist and PMMA e-beam resist leaves a residue on both the silicon dioxide substrate and the graphene film. It is possible to remove most of the undesirable resist residue after liftoff by annealing the sample. The standard annealing process used for graphene device fabrication is done putting the sample inside a sealed quartz tube with a flux of a mixture of 900 sccm of Ar and 100 sccm of H_2 at 300 ^{o}C for two hours.

The resist liftoff is the final step of a graphene device preparation. Fig. 4.2 shows a schematic procedure for all the fabrication process.

4.2 Back gated devices

Charges in graphene can be induced by applying a potential difference V_g between the graphene and the silicon substrate [5,6,42]. We can model the amount of charge induced in graphene by considering the system as a parallel plate capacitor, where one plate is the graphene sheet and the other one is the conducting p-doped silicon substrate. The silicon dioxide layer works as the dielectric medium between them. The geometric

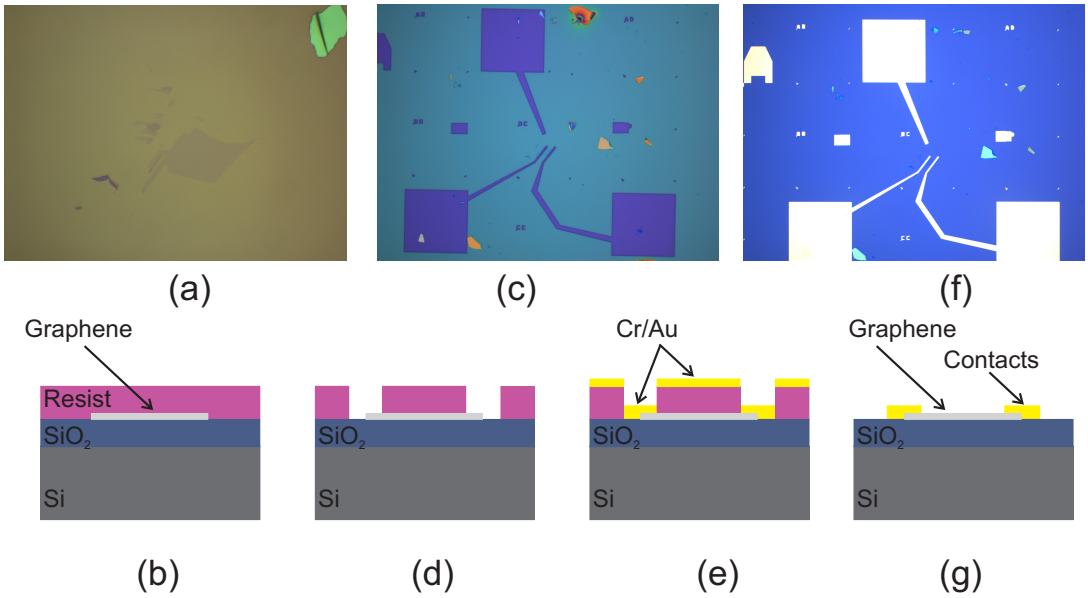

Figure 4.2: Schematic diagrams of the lithography process. (a) Exfoliated graphene sample on the Si/SiO_2 substrate. (b) The resist is spun on the substrate. (c) and (d) After the development, the resist is removed from the exposed regions. (e) Metal evaporation over the substrate. (f) and (g) Liftoff of the remaining resist.

capacitance per unit area C_G of this system is given by

$$C_G = \frac{\varepsilon\varepsilon_0}{d}\,, \tag{4.1}$$

where $\varepsilon_0 = 8.854 \times 10^{-12}\,\mathrm{Fm}^{-1}$ and ε are the permittivity of the free space and of the dielectric material, respectively, and d is the dielectric thickness. Then, the number of electrons per unit of area n of charge $e = 1.602 \times 10^{-19}\,\mathrm{C}$ transferred to the graphene by applying a voltage V_g is given by [42]

$$n = \frac{\varepsilon\varepsilon_0(V_g - V_0)}{ed} = 7.2 \times 10^{10}\mathrm{cm}^{-2}\mathrm{V}^{-1}(V_g - V_0)\,, \tag{4.2}$$

where we have used $d = 300\,\mathrm{nm}$ and $\varepsilon = 3.9$ for the silicon dioxide [48]. Here, V_0 is the necessary voltage to move the Fermi level to the Dirac point, *i.e.*, the charge neutrality point.

In the same way, the Fermi energy E_F can also be related to the gate voltage. We first must note that the number of states per unit of area in a two-dimensional system is given by [49]:

$$n = \frac{N}{A} = \frac{gk_F^2}{4\pi}\,, \tag{4.3}$$

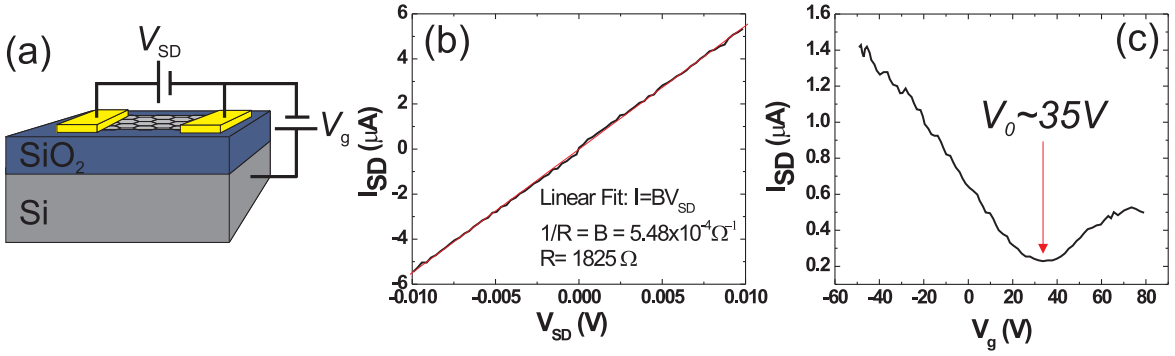

Figure 4.3: (a) Schematic view of the back gate graphene device. A variable voltage V_g can be applied between the graphene and the p-type silicon substrate. The device is treated as a parallel plate capacitor where the silicon oxide layer is the dielectric medium. Also, a source-drain voltage V_{SD} can be applied between two gold contacts. A typical response for the bilayer graphene devices used in this work under an applied (b) V_{SD} and (c) V_g, taken at T=300 K.

where N is the total number of states, A is the area of the unit cell of the reciprocal space, $g = 4$ is the spin and valley degeneracy and k_F is the wavevector at the Fermi level. For monolayer graphene, assuming the linear dispersion $E_F = \hbar v_F k_F$, and substituting k_F and Eq. 4.2 into Eq. 4.3, the Fermi energy E_F can be written in terms of V_g as

$$E_F = \hbar v_f \sqrt{\pi C_G |V_g - V_0|/e}\,. \tag{4.4}$$

For bilayer graphene, considering only the coupling between the first neighbors in the same layer $\gamma = \sqrt{3}\gamma_0 a/2$ and the first neighbors of the adjacent layers γ_1 (see Section 2.2.2), the two electronic bands near the neutrality point (π_1 and $\pi_1^\star$) are given by $E_F = \pm\left(-\gamma_1/2 + \sqrt{\gamma^2 k_F^2 + \gamma_1^2/4}\right)$ [25]. Making the same procedure done for monolayer graphene, we have the Fermi energy as a function of the gate voltage:

$$|E_F| = -\frac{\gamma_1}{2} + \frac{1}{2}\sqrt{\frac{4\pi\gamma^2 C_G}{e}|V_g - V_0| + \gamma_1^2}\,. \tag{4.5}$$

Fig. 4.3(a) shows the schematic view of a graphene device, where an applied gate voltage V_g can induce the potential difference between the silicon substrate and the graphene with a gold contact. A source-drain voltage V_{SD} can also be applied between the two gold contacts. From the dependence of the source-drain current I_{SD} on V_{SD}, it is possible to obtain the resistance R of the system. Figs. 4.3(b) and (c) show a typical response for the bilayer graphene samples used in this work of the current passing through

the device under an applied V_{SD} and V_g, respectively, at room temperature. We can see from Fig. 4.3(b) that the system has a ohmic response, and the resistance is given by the inverse of the slope of the curve. For this specific sample this value is $R = 1825\Omega$. The resistance is due to the contacts resistance plus imperfections in the crystal lattice. From the dependence of the I_{SD} with V_g, we can estimate V_0 (the minimum of the curve), *i.e.* the value of the voltage necessary to bring the Fermi level to the neutrality point, that for this sample is around 35 V.

4.3 Top gated devices

To induce charges in graphene, it is also possible to apply a top gate instead of a back gate. A traditional top gate is achieved by depositing a dielectric layer followed by a metallic contact evaporation on the top of the graphene sheet after the lithography to make the contacts in the graphene (Fig. 4.4(a)). In this work, we have used another option for the top gate: an electrolyte solution (Fig. 4.4(b)). The advantages of using a polymer electrolyte instead of the traditional solid top gate is that the polymer electrolyte is a top transparent gate and enables the application of large electric fields that induces enormous carrier densities well beyond $10^{13}\,\mathrm{cm}^{-2}$ and isolates the graphene from air avoiding adsorption of molecules like O_2 that can introduce defects. On the other hand, the polymer electrolyte has potential problems as well, and electrochemical reactions may occur between the electrolyte and the device during gating, and the reaction may accelerate under illumination.

The polymer electrolyte is formed by dissolving salts in soft polymeric materials. The electric conduction mechanism involves motion of oppositely charged ions in opposite directions in the polymer matrix. At the electrode-polymer interface, the ion flow is stopped before chemical reactions could occur. A double layer (also known as Debye layer) of opposing charges is then formed between the gate material and the polymer matrix as shown in Fig. 4.4(c), and is held as long as the gate voltage does not exceed the threshold for electrochemical reactions. The distance between the oppositely-charged layers at the electrodes is given by the Debye screening length which is typically of the order of few nanometers [50]. Because of the small Debye length, the geometric capacitance (Eq. 4.1) of the system is much larger than in the usual back gating using Si/SiO_2, where the distance between the two oppositely-charged layers is about 300 nm. It is then possible to charge the sample with a much higher density of carriers.

We have used two different kinds of polymer electrolyte in this work. The first is

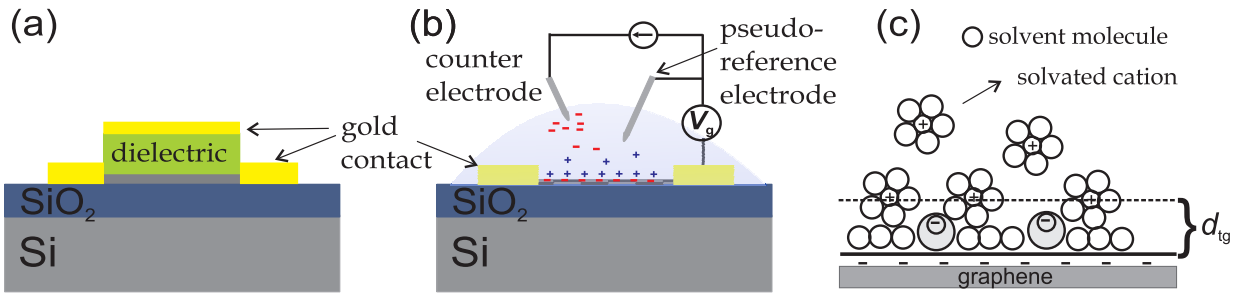

Figure 4.4: Schematic view of the top gate graphene devices using (a) solid dielectric and solid contacts and (b) electrolyte solutions. (c) Proposed model of the double-layer region, where d_{tg} is the Debye length.

a mixture of sodium perchlorate ($NaClO_4$) and polyethylene glicol (PEG, molar weight 900000) with a weight ratio of 0.25:1 and dissolved in tetrahydrofuran (THF) to form a precursor. The second alternative used here is to dissolve lithium perchlorate ($LiClO_4$) and poly(methyl methacrylate) (PMMA, molar weight 120000) with a weight ratio of 0.30:1 in propylene carbonate (PC). In both cases, it is important that the components are very dry, so the electrolyte shows a better stability. Once the precursor is done, we apply it to the graphene device. The solvent evaporates and a thin film of transparent polymer electrolyte is formed on top of the device. The device can be baked at about 90 ^{o}C to remove residue moisture and alcohol. The transparency of the film makes it convenient for optical studies of these devices.

Using the polymer electrolyte, the voltages are applied using a potentiostat. The configuration of the experimental setup is shown in Fig. 4.4(b). The contacted graphene sample is made using the method described in Section 4.1 and is the working electrode. Two additional electrodes which is not in contact with the graphene sample is defined on the SiO_2 substrate for the purpose of polymer gating. The additional electrodes can be either designed during lithography or obtained by inserting a metal wire in the polymer electrolyte film. One of these electrodes is the counter-electrode, responsible for the voltage source, and the other one is the pseudo-reference electrode, used to monitor the electrostatic potential in the working electrode [51].

We now discuss how the applied top gate voltage using a polymer electrolyte is converted to the doping n in graphene. In general, the application of a gate voltage V_g creates an electrostatic potential difference ϕ between the graphene and the gate electrode, and the addition of charge carriers leads to a shift in the Fermi level E_F. Therefore, V_g is

given by

$$V_g = \frac{E_F}{e} + \phi\,, \tag{4.6}$$

with E_F/e being determined by the chemical (quantum) capacitance of the graphene, and $\phi = ne/C_G$ being determined by the geometrical capacitance C_G [52].

If we remember the back gating situation, the graphene on a Si/SiO_2 substrate with 300 nm of SiO_2 has a very low value for the geometric capacitance per unit area $C_G = 1.15 \times 10^{-8}\,\mathrm{Fcm^{-2}}$ (see Eq. 4.1). Therefore, for a typical value of $n = 1 \times 10^{13}\,\mathrm{cm^{-2}}$, the potential drop is $\phi = 140\,\mathrm{V}$, much larger than E_F/e. $E_F/e \sim 0.37\,\mathrm{V}$ for monolayer graphene and $E_F/e \sim 0.22\,\mathrm{V}$ for bilayer graphene. Hence, for back gate $V_{bg} \approx \phi$ and the doping concentration becomes $n = \eta V_{bg}$, where $\eta = C_G/e$.

We shall now consider the present case of top gating. Similar to the back gate system, where we consider a parallel-plate capacitor with the silicon dioxide being the dielectric material, the top gate system can also be model as a parallel-plate capacitor, but now the Debye layer is the dielectric layer. The Debye length is given by $d_{tg} = (2ce^2/\varepsilon\varepsilon_0 kT)^{-1/2}$ for a monovalent electrolyte [52], where c is the concentration of the electrolyte, e is the electric charge and kT is the thermal energy. In principle, d_{tg} can be calculated if the electrolyte concentration is known. However, in the presence of a polymer, the electrolyte ions form complexes with the polymer chains and the exact concentration of ions is not amenable to measurement. For polymer electrolyte gating the thickness of the Debye layer is reported to be a few nanometres ($\sim 1 - 5\,\mathrm{nm}$) [52]. The dielectric constant ε of PEG is ~ 5 [52] and of PMMA is ~ 2.6 [53]. Assuming a Debye length of 2 nm, we obtain a gate capacitance per unit area $C_G = 2.2 \times 10^{-6}\,\mathrm{Fcm^{-2}}$ for PEG and $C_G = 1.2 \times 10^{-6}\,\mathrm{Fcm^{-2}}$ for PMMA, which is much higher than the geometric capacitance for the back gate system. Therefore, the first term in Eq. 4.6 cannot be neglected.

For monolayer graphene, substituting ϕ and Eqs. 4.2 and 4.4 into Eq. 4.6, we get

$$V_g = \frac{\hbar v_F \sqrt{\pi n}}{e} + \frac{ne}{C_G}\,. \tag{4.7}$$

Using the numerical values $C_G = 2.2 \times 10^{-6}\,\mathrm{Fcm^{-2}}$ and $v_F = 1.0 \times 10^6\,\mathrm{m/s}$

$$V_g = 1.16 \times 10^{-7}\sqrt{n} + 0.728 \times 10^{-13} n\,, \tag{4.8}$$

where n is in units of $\mathrm{cm^{-2}}$.

In the case of bilayer graphene, additional care must be taken when compared to the back gated devices. With the use of the polymer electrolyte as top gate it is possible to charge the sample with a much higher density of carriers. Then, it is possible to reach

the second valence (or conduction) band π_2 ($\pi_2^\star$) of bilayer graphene with this gating mechanism, where the charge density reaches more than the energy between the first and the second valence (conduction) band, *i.e.* γ_1 ($n \sim 3 \times 10^{13}\,\mathrm{cm}^{-2}$) [25]. There are now two regimes for the dependence of the E_F with n that are given by [25]

$$E_F = -\frac{\gamma_1}{2} + \frac{1}{2}\sqrt{4\pi\gamma^2|n| + \gamma_1^2} \qquad \text{, for} \quad E_F < \gamma_1 \tag{4.9}$$

$$E_F = \sqrt{\frac{\pi\gamma^2|n|}{2}} \qquad \text{, for} \quad E_F > \gamma_1 \tag{4.10}$$

Hence, substituting Eqs. 4.9 and 4.10 and ϕ into Eq. 4.6, we get

$$\begin{aligned} V_g &= -\frac{\gamma_1}{2e} + \frac{1}{2e}\sqrt{4\pi\gamma^2|n| + \gamma_1^2} + \frac{ne}{C_G} \qquad (4.11)\\ &= -0.175 + \sqrt{0.51 \times 10^{-13}|n| + 0.1225} + 0.728 \times 10^{-13} n \qquad \text{, for} \quad E_F < \gamma_1 \\ V_g &= \frac{1}{e}\sqrt{\frac{\pi\gamma^2|n|}{2}} + \frac{ne}{C_G} \qquad (4.12)\\ &= 0.79 \times 10^{-7}\sqrt{|n|} + 0.728 \times 10^{-13} n \qquad \text{, for} \quad E_F > \gamma_1 \end{aligned}$$

where $C_G = 2.2 \times 10^{-6}\,\mathrm{Fcm}^{-2}$, $\gamma_1 = 0.40\,\mathrm{eV}$ and $\gamma = \sqrt{3}\gamma_0 a/2$ were used in the right part of the equation.

Chapter 5

Electron-phonon interactions in graphene

Electron-phonon (el-ph) interactions are responsible for many important effects in condensed matter physics [1]. In particular, the phonon self-energy, which is mainly due to the el-ph coupling, is a remarkable effect which contributes to both the phonon frequency and decay width renormalizations due to the creation (annihilation) of electron-hole (e-h) pairs through phonon absorption (emission). These phonon self-energy corrections are needed to explain a set of well-known effects, such as the Kohn anomaly [1,19], the Peierls transition [1,54,55], polaron formation [1,56,57], and other types of phonon renormalizations and perturbations caused by el-ph interaction processes [3,58–60]. In this chapter, we will present the experimental results found for the electron-phonon coupling in monolayer graphene and in bilayer graphene. General predictions for the electron-phonon interactions are well described in Section 2.4.

5.1 Monolayer graphene

Particularly special, single-layer graphene (1LG) has linear electronic energy dispersions $E(\mathbf{k})$ around the non-equivalent high symmetry points K and K' in the Brillouin zone, which can be described by the Dirac equation considering massless particle behavior [61]. However, one cannot properly solve the electronic and vibrational structure for most nanocarbon materials near the Dirac points when considering the adiabatic approximation, which decouple the ionic motion of the carbon ions and the electronic structure [5,32,62]. When the adiabatic approximation cannot be applied [1,19], the el-ph interactions must take into account non-adiabatic processes, which give rise to important

and strong phonon self-energy corrections [1]. Within second-order perturbation theory, the phonon self-energy can be approximately described as (see Eq. 2.51) [1,3,19,60]:

$$\Pi(\omega_{\mathbf{q}}, E_F) = 2\sum_{\mathbf{kk'}} \frac{|M_{\mathbf{k},\mathbf{k'}}|^2}{\hbar\omega_{\mathbf{q}}^0 - E^{eh} + i\gamma_{\mathbf{q}}} \times [f_h - f_e] \ , \tag{5.1}$$

where $\mathbf{k}$ and $\mathbf{k'}$ are, respectively, wavevectors for the initial and final electronic states; $\mathbf{q} \equiv \mathbf{k} - \mathbf{k'}$ is the phonon wavevector; $E^{eh} \equiv (E^e_{\mathbf{k'}} - E^h_{\mathbf{k}})$ is the electron-hole (e-h) pair energy; $\omega^0_{\mathbf{q}}$ is the phonon frequency; $\gamma_{\mathbf{q}}$ is the phonon decay width; $f_h(f_e)$ is the Fermi distribution function for holes (electrons) and $M_{\mathbf{k},\mathbf{k'}}$ gives the electron-phonon (el-ph) coupling matrix element. For a specific $\omega^0_{\mathbf{q}}$, the phonon energy correction due to its self-energy is given by $\Delta\omega = \mathrm{Re}[\Pi(\omega_{\mathbf{q}}, E_F)]$, which is the real part of Eq.5.1. Likewise, the decay width correction $\Delta\gamma_{\mathbf{q}}$ is given by the imaginary part $\mathrm{Im}[\Pi(\omega_{\mathbf{q}}, E_F)]$ of Eq. 5.1 [1,19,60].

These phonon renormalizations occur anytime we have non-zero matrix elements $M_{\mathbf{k},\mathbf{k'}}$, *i.e.*, anytime that an electron-hole pair can be created (annihilated) by a phonon absorption (emission) process. In Eq. 5.1, although the summation is performed over all the electronic states, the combination of electronic states that fulfills the momentum and energy requirements for a given phonon will be the ones to significantly contribute to the phonon self-energy. In other words, this combination of states will present a non-null $M_{\mathbf{k},\mathbf{k'}}$ and a resonant behavior given by the denominator of Eq. 5.1. There are two types of electron-phonon interactions, namely intravalley (AV) (Fig. 5.1(a) and Fig.5.2(b)) and intervalley (EV) (Figs. 5.2(a) and (c)) processes [63]. For AV processes, the initial and final states both occur within the region close to the same K point, while for EV processes, K is connected to an inequivalent K' by a $q \neq 0$ phonon. Thus the AV (EV) process corresponds to phonons around the Γ (K) point. The phonon wavevector $\mathbf{q}$ for an AV (EV) process is measured from the Γ (K) points and can assume both the $q = 0$ or $q \neq 0$ conditions (see Fig. 3.4 for details).

5.1.1 Phonon renormalization in the second order Raman processes

Most of the discussions of the phonon self-energy renormalizations have been for zone-center phonons (Γ point) with $q = 0$, which can be appreciated by observing the G-band Raman feature evolution in monolayer graphene (1LG) as the Fermi level energy (E_F) is varied (see Figs. 5.1(b) and (c)) [3,31,34,58,64]. In the present work, we use gate-modulated resonant Raman spectroscopy to address the effect of the E_F variation due

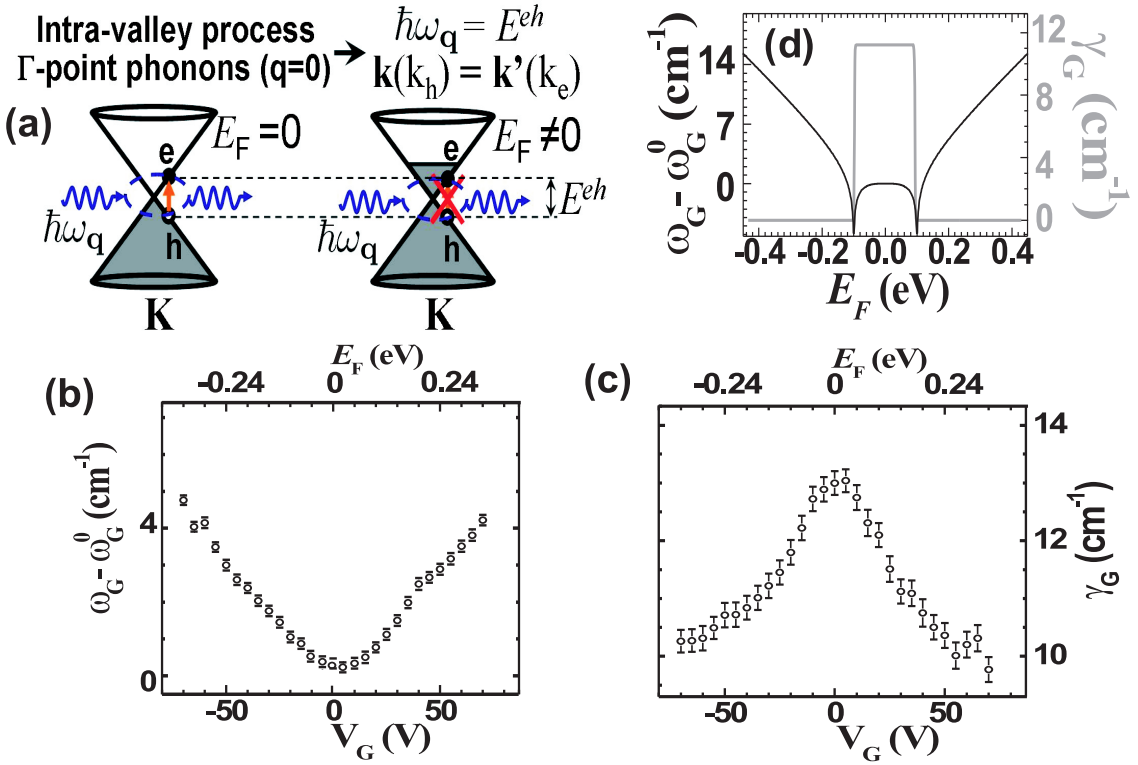

Figure 5.1: (a) Possible ($E_F = 0$) and not possible ($E_F \neq 0$) AV $q = 0$ processes for e-h pair creation due to phonon (with energy $\hbar\omega_{\mathbf{q}}$) absorption. E^{eh} stands for the e-h pair energy. (b) The frequency ω_G hardening and (c) the decay width γ_G narrowing for the G-band Raman feature as a function of gate voltage V_g. (d) Theoretical predictions based on Ref. [19] of the E_F dependence of $\Delta\omega$ and $\gamma_{\mathbf{q}}$ for an AV $q = 0$ process for $T = 10K$.

to an applied gate voltage (V_g) on the phonon self-energy (Eq.5.1), for 1LG systems, in cases where $q \neq 0$ (AV and EV processes). These are cases which have not been sufficiently studied previously. Here, we study the double resonance Raman frequency ranges between 2350 and 2850 cm^{-1}, which contain the G* and the G$'$ bands as shown in Fig. 5.3(a) [17,61,65]. We show below that the phonon renormalization for the $q \neq 0$ phonons gives an E_F dependence different from that for the $q = 0$ measured from the Γ point phonons. We also show that these differences in behavior can be used to show that the G* feature is composed of two Raman peaks which behave differently from one another as $|V_g|$ is varied.

The graphene devices used in this experiment were produced as described in Section 4.1 and a back gate voltage was applied. For each V_g value, Raman spectra were taken with a 532 nm wavelength laser source in the backscattering geometry using a 100× objective and laser power around 1.5 mW. The spectra were analyzed using Lorentzian

line-shapes from which frequencies and decay widths were extracted. Figs. 5.1(b) and (c) and Figs. 5.3(a)-(e) show the experimental results. We show that, due to the difference in behavior between the $q = 0$ and $q \neq 0$ processes, this combination of techniques provides a precise way to verify the assignments of either overtones and/or a combination of phonon modes.

The G* and G$'$ features were intentionally chosen for this discussion because: (1) they are the most prominent double-resonance Raman features in the graphene spectrum, offering a convenient platform, together with the G band, to observe experimentally the two different types of phonon renormalizations, one found for the $q = 0$ phonons and the other for $q \neq 0$ phonons, and (2) as a consequence of these different phonon renormalization effects, we have solved a long-time discussion in the literature about the G* feature, showing that the G* feature is composed of <u>both</u> the iTO+LA ($q = 2k$) and 2iTO ($q = 0$) Raman active modes, both measured from the K point. In the literature, the G* feature around 2450 cm^{-1} has been assigned to either the iTO+LA phonon combination mode ($q = 2k$ EV process) [17], or to the 2iTO phonon overtone mode ($q = 0$ EV process) [65]. However, Fig. 5.3(a) shows that indeed the G* feature is asymmetric, suggesting that it consists of two Lorentzians peaks rather than just one. The iTO+LA ($q = 2k$) combination mode presents a dispersion of -(16±1) cm^{-1}/eV (measured in this work), while the 2iTO ($q = 0$) overtone mode (also measured in this work) is not dispersive (see Fig. 5.3(b)).The G$'$ feature at 2670 cm^{-1} is widely known to be an overtone of the iTO phonon mode ($q = 2k$) [17,61,65]. It gives a dispersive phonon frequency as a function of laser excitation energy E_L which exhibits the value of 103 cm^{-1}/eV [66].

As discussed in the Section 2.4.3, the phonon energy correction $\Delta\omega$ has previously been explored for the cases where the phonon momentum $\mathbf{q}$ vanishes ($q = 0$) for the AV intravalley process and, at zero temperatures ($T = 0$), is described by:

$$\Delta\omega = \alpha|E_F| + \frac{\alpha\hbar\omega^0_{\mathbf{q}}}{4} ln\left(\left|\frac{|E_F| - \frac{\hbar\omega^0_{\mathbf{q}}}{2}}{|E_F| + \frac{\hbar\omega^0_{\mathbf{q}}}{2}}\right|\right) \quad , \tag{5.2}$$

where $\alpha = 4.43 \times 10^{-3}$ [19] and $\gamma_{\mathbf{q}}$, which will be proportional to the el-ph coupling strength, gives the damping of the phonon mode due to real e-h pair creation [19,31, 60,64]. Fig. 5.1(d), which was based on Ref. [19], give the results illustrated for the renormalization of $\omega_{\mathbf{q}}$ and $\gamma_{\mathbf{q}}$, respectively. From Fig. 5.1(d) and Eq.5.2, we observe that when $|E_F| < \hbar\omega_{\mathbf{q}}/2$, real e-h pairs can be created, which leads to a stronger electron-ion interaction screening. As a consequence, the phonon mode softens [19,31,60,64]. However, when $|E_F| > \hbar\omega_{\mathbf{q}}/2$ the production of real e-h pairs becomes forbidden due to the Pauli

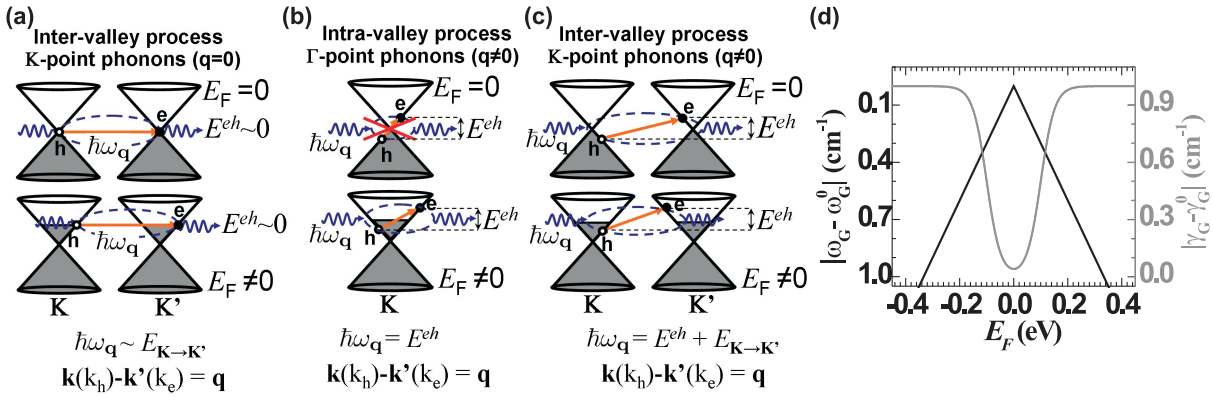

Figure 5.2: (a) Possible ($E_F = 0$ and $E_F \neq 0$) $q = 0$ (measured from the K point) EV processes. (b) Not possible ($E_F = 0$) and possible ($E_F \neq 0$) AV processes for electron-hole pair creation due to phonon (with energy $\hbar\omega_{\mathbf{q}}$) absorption when the phonon wavevector is not zero ($q \neq 0$). (c) Possible EV processes for electron-hole pair creation due to phonon (with energy $\hbar\omega_{\mathbf{q}}$) absorption when the phonon wave-vector is not zero ($q \neq 0$). (d) Illustrative predictions for the V_g-dependence of the phonon frequency correction $\Delta\omega$ (black line) and the corresponding decay width $\gamma_{\mathbf{q}}$ (grey line) when $q \neq 0$, both as a function of E_F. The $\Delta\omega$ and $\gamma_{\mathbf{q}}$ values in (d) were normalized to illustrate the concept of $\omega_{\mathbf{q}}$ softening and $\gamma_{\mathbf{q}}$ broadening. E^{eh} is the e-h pair energy and $E_{K\to K'}$ is the energy required to translate an electron from K to K'. Remember that the energy is not conserved when going from K to K'. They are inequivalent points under a time-reversal symmetry operation. Physically, this means that there is an energetic cost (charged to the system) to go from K to K'. This would not happen if the points were equivalent.

exclusion principle. This leads to a phonon mode hardening where the phonons are not damped any more (they are now long lived) [19,31,60,64]. As an example of phonon renormalization when $q = 0$ for the AV process (see Fig. 5.1(a)), the ω_G and γ_G variations of the G Raman band are shown in Figs. 5.1(b) and (c), respectively, as $|E_F|$ is varied due to different V_g values. The G band corresponds to the first order $q = 0$ iTO and iLO phonon branches around the Γ point. The experimental results (Figs. 5.1(b) and (c)) are in good agreement with theory [19,31,34,64], which shows a ω_G hardening and γ_G narrowing when V_g increases. Next, we report the new experimental results for phonons corresponding to the cases $q = 0$ EV (intervalley) and $q \neq 0$ AV/EV processes.

Both the G* iTO+LA mode at $\sim$ 2450 cm^{-1} and the G$'$ mode at $\sim$ 2670 cm^{-1} are EV double-resonance Raman processes with $q \neq 0$ and, as shown in Figs. 5.3(c)-(e), and they both show a different behavior when V_g increases compared to the behavior observed for the AV $q = 0$ process. Starting with the G$'$ band, it is seen that its frequency $\omega_{G'}$ decreases with increasing $|V_g|$ (Fig. 5.3(c)), while its decay width $\gamma_{G'}$ increases with

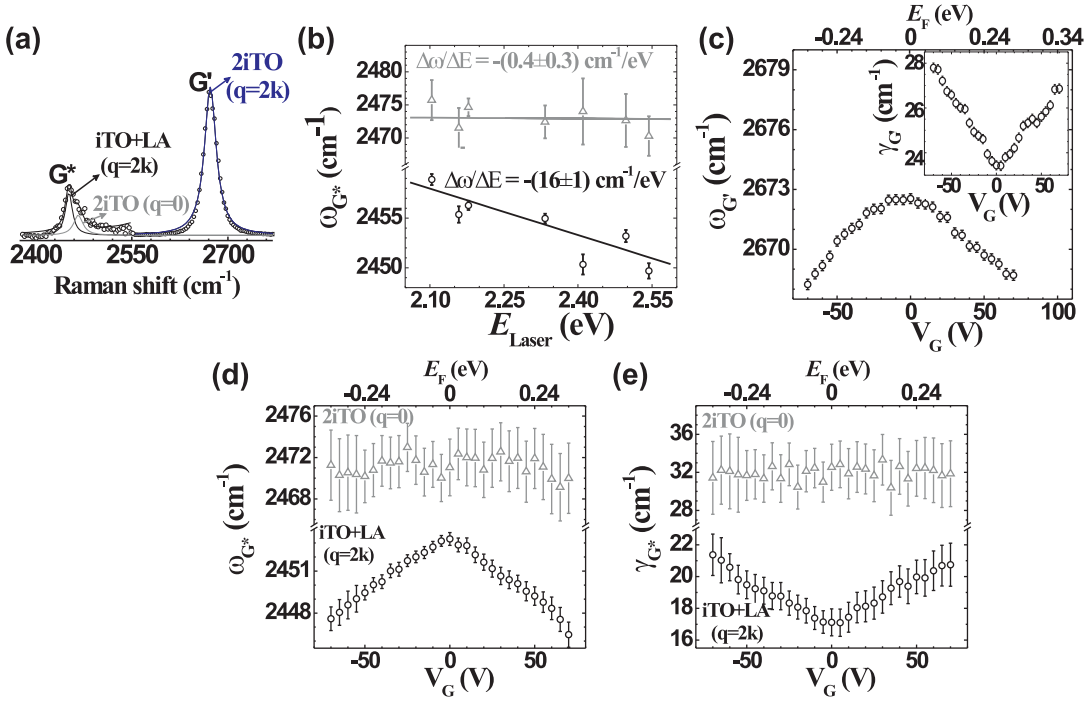

Figure 5.3: (a) The experimental G* and the G$'$ bands as they appear in the resonant Raman spectrum. The asymmetric G* feature is a combination of the iTO+LA ($q = 2k$ read from the K point) mode and the 2iTO ($q = 0$ read from the K point) mode. The G$'$ mode is an overtone of the iTO mode ($q = 2k$). For illustrative purposes, the signal of the G* feature was multiplied by a factor of 10 and the Lorentzian profiles used to fit the spectrum are shown in constructing (a). (b) The frequency dispersion of the G* peaks as a function of laser energy ($E_{\rm Laser}$) and shows that the iTO+LA ($q = 2k$) is a dispersive mode [$-(16 \pm 1)\,{\rm cm}^{-1}/{\rm eV}$], while the 2iTO ($q = 0$) is non-dispersive [17,65]. (c) The gate voltage V_g dependence of the 2iTO ($q = 2k$) $\omega_{\mathbf{G}'}$ and $\gamma_{\mathbf{G}'}$ (inset in (c)). (d) and (e) show, respectively, the $\omega_{\mathbf{q}}$ and $\gamma_{\mathbf{q}}$ dependencies on $|E_F|$ seen for the iTO+LA and 2iTO modes. The error bars come from the fitting procedure.

increasing $|V_g|$ (see the inset in Fig. 5.3(c)). Here, we see that the same behavior is observed for the iTO+LA mode frequency $\omega_{\rm iTO+LA}$, as shown in Fig. 5.3(d), and for its decay width $\gamma_{\rm iTO+LA}$, as shown in Fig. 5.3(e). For the 2iTO G* feature at $\sim 2470\,{\rm cm}^{-1}$, which is a $q = 0$ EV process around the K point, it is observed in Figs. 5.3(d) and (e) that the frequency $\omega_{\rm 2iTO}$ and the decay width $\gamma_{\rm 2iTO}$ almost do not change with increasing $|V_g|$. This behavior shows that the 2iTO ($q = 0$) mode couples only weakly to the electronic states in graphene and therefore its phonon self-energy corrections are negligible.

To explain our experimental findings, a phenomenological formulation for the phonon self-energy for the EV $q = 0$ and AV/EV $q \neq 0$ processes in single-layer graphene are presented. If we remember the case of AV processes for the $q = 0$ phonons (Fig. 5.1(a)),

which applies to the G-band feature (see Figs. 5.1(b) and (c)), the creation of a real e-h pair is very high when $E_F = 0$, which implies a $\omega_{\mathbf{q}}$ softening and a $\gamma_{\mathbf{q}}$ broadening. With increasing $|E_F|$, $\omega_{\mathbf{q}}$ hardens and $\gamma_{\mathbf{q}}$ narrows, which means that the real e-h pair creation is being halted by the Pauli principle because the phonon energy is becoming smaller than $2|E_F|$. Next, we see that this approach can now be used to understand the $q \neq 0$ processes considering a small difference: now, instead of the Pauli principle, the density of phonon and electronic states, as well as the energy and momentum conservation requirements, will be responsible for halting the real e-h pair creation.

As shown above, a different behavior is expected for the $q = 0$ phonon (measured from K-point) in the EV process shown in Fig. 5.2(a), which explains the G* 2iTO mode behavior as $|E_F|$ is varied with varying V_g. According to the Fermi golden-rule, the probability that a real electron-hole pair exists at $E_F = 0$ (upper line of Fig. 5.2) is quite small since the density of states of both, electrons and phonons, at $E_F = 0$ almost vanishes [3,61]. Therefore, no softening of $\omega_{\mathbf{q}}$ and no broadening of $\gamma_{\mathbf{q}}$ is expected, since almost no real electron-hole pair is being created. When $|E_F|$ increases (lower line in Fig. 5.2), the probability for a K point $q = 0$ phonon to connect inequivalent energy $\mathbf{k}$ and $\mathbf{k}'$ states increases, because the density of phonon and electron states also increases as we move away from the K point [3,61]. This means that the number of real e-h pair creations increases and thus the phonon mode softening and damping effects could be observed with increasing $|E_F|$. However, for EV processes with $q = 0$ (measured from the K point), the phonon energy and momentum are not enough to create an e-h pair. This means that $\Delta\omega$ will be a small correction and, therefore, small $\omega_{\mathbf{q}}$ softening and small $\gamma_{\mathbf{q}}$ damping are expected for any $|E_F|$ value (weak E_F-dependence).

By considering phonon modes with $q \neq 0$ (AV and EV processes) as shown in Figs. 5.2(b) and (c), the phonon wavevectors are either around the Γ point or around the K point. These cases explain the G$'$ and the G* iTO+LA mode behaviors as $|V_g|$ is varied. Since the phonon and electron density of states are small close to the K point and since the phonon energy dispersion for graphene has a much smaller slope than that for the electronic energy dispersions [61], there is essentially no coupling between $q \neq 0$ phonons and e-h pairs (there is no $\mathbf{q}$ such that $\mathbf{q} = \mathbf{k} - \mathbf{k}'$) if $E_F = 0$ and therefore the softening and damping of the phonon mode in this case does not take place in a resonant way, *i.e.*, where $E^{eh} = \hbar\omega_{\mathbf{q}}$. If no phonons with $q \neq 0$ can connect electronic states with different $\mathbf{k}$ and $\mathbf{k}'$ at $E_F = 0$, the matrix elements $M_{\mathbf{k},\mathbf{k}'}$ in Eq. 5.1 are close to zero and essentially no self-energy corrections occur. Precisely speaking, in the case of the EV process (Fig. 5.2(c)), the e-h pair creation is possible for $E_F = 0$ but, as stated above, the

density of phonon and electron states is very small at $E_F \sim 0$ which makes the probability for the e-h pair creation also small. However, when $E_F \neq 0$, the density of phonon and electron states increases and phonon modes with $q \neq 0$ can now connect electronic states with different $\mathbf{k}$ and $\mathbf{k}'$, in the sense that there is a $\mathbf{q}$ such that $\mathbf{q} = \mathbf{k} - \mathbf{k}'$ (the differences between slopes in the electron and phonon dispersion decrease when we move away from the K point [61]). This gives rise to a strong electron-phonon coupling which enhances the creation of real e-h pairs. As a consequence, the phonon mode softens ($\omega_{\mathbf{q}}$ decreases) and gets damped ($\gamma_{\mathbf{q}}$ broadens) as shown in Figs. 5.2(b) and (c). This $q \neq 0$ (AV and EV processes) behavior is illustrated in Fig. 5.2(d), where it is seen that the frequency softening (black solid line) must increase with increasing $|E_F|$ while the decay width (grey solid line) must broaden with increasing $|E_F|$.

5.1.2 Electron-phonon coupling of combination modes

In this section, we will show a new technique to assign phonon modes in materials using gate-dependent and laser dependent Raman spectroscopy. We will use the results of electron-phonon coupling for the second order Raman process presented in the last section to study some combination modes with $q \neq 0$ in monolayer graphene.

Gate modulated and laser excitation energy (E_L) dependent Raman spectroscopy have been both widely used to distinguish the numbers of layers of a graphene flake [41], to distinguish the stacking order in flakes [67–70], and to study the phonon self-energy as well as electron-phonon interactions [19,29,30,32,52,64,71]. Recently, attention has been given to studying some weak Raman features in the frequency range $1650 < \omega < 2300\,\mathrm{cm}^{-1}$, which are associated with Raman combination and overtone modes [67–69]. Indeed, it has been shown that such studies on few layer graphene (FLG) can give us information about both the number of graphene layers in FLG and their stacking order [67,68]. However, these works disagree with each other regarding the number of phonon peaks and the phonon assignments attributed to each peak [67–69]. Since there are many possible combination modes in this frequency region and since the double resonance Raman (DRR) mode frequencies are dispersive as a function of E_L [39], it has not been easy to determine the number of peaks and their individual dispersions. Additionally, there are two DRR conditions for the phonon wavevector: $q \approx 2k$ (measured from the Γ and K points) and $q = 0$ (measured from the K point) which give different Raman peaks with and without dispersive behaviors [72,73], respectively. The peaks around the Γ point come from an intravalley process, in which the photo-excited electron is scattered by a

phonon to another point of the conduction band near the same Dirac point and the peaks around the K point come from an intervalley process, where the electron is scattered from the K point to an inequivalent K' point of the Brillouin zone (BZ). Moreover, the phonon self-energy and the electron-phonon (el-ph) coupling associated with these combination modes have not yet been explored in detail.

Concerning single layer graphene (1LG), the first study of the combination modes in this frequency region between 1690 and 2150 cm^{-1} was reported by Cong *et al.* [68], where they show only three peaks (which are denoted in the present paper by peaks 1, 3 and 4, from the lowest to the highest frequency). They [68] proposed their assignments to be combinations of the $q \neq 0$ phonon branches LO+iTA, iTO+LA and LO+LA, from the lowest to the highest frequency, around the Γ point of the BZ, *i.e.*, all their peaks come from intravalley DRR processes. Rao *et al.* [67] showed that there are two more peaks in this region, one around 1880 cm^{-1} (peak 2 in the present paper) and the other one around 2220 cm^{-1} (our peak 5). The 1880 cm^{-1} and 2220 cm^{-1} peaks were tentatively assigned by them [67] to the $q \neq 0$ oTO+LO and iTO+iTA phonon branch, respectively, both being an intervalley DRR process, *i.e.*, around the K point of the BZ. However, by performing only E_L-dependent Raman experiments, it is not easy to properly assign the combination modes when these combination modes are close together in frequency. Moreover, an experiment limited to E_L-dependent measurements does not tell us in which directions in k space the various scattering processes are happening.

In this work, it is shown that the **k**-dependent electron-phonon interaction as investigated by studying the Raman spectra, as a function of both Fermi energy E_F by variation of the gate voltage V_g and laser energy E_L, is important to give accurate/reliable information about the combination modes. Besides this, we show that gate-modulated Raman spectroscopy of $q = 0$ and $q \neq 0$ phonons is a new and powerful approach to understand the nature and to assign phonon modes as well as their overtones and mutual mode combinations. We apply this new approach to solve the uncertainty behind the phonon assignments of the Raman features between 1700-2300 cm^{-1}. The well known E_L-dependent experiment tells us which phonon branches could be involved in the processes, giving also their respective dispersion slopes, that depend on graphene phonon velocities. First, we confirm the number of Raman peaks observed experimentally in this frequency range and we check that the mode assignment is correct for each Raman peak by making a direct comparison between the experimental data and theoretical phonon dispersion calculations [27]. Further, for the Raman peaks that come from an intervalley DRR process, a discussion about the scattering directions, in terms of the high symmetry

directions $K\Gamma$ and KM, of the various processes is important because the el-ph scattering matrix elements have a large **k** dependence, which gives more precise information on **q** phonon wavevector dependence, and we find that the **q** vectorial dependence is relevant for the DRR process.

Finally, we explore the phonon self-energy and electron-phonon (el-ph) coupling for these modes in 1LG by varying E_F of the system by an applied gate voltage (V_g). For all the five observed Raman peaks in this frequency range, we can see a softening of the phonon frequency ω_q and a broadening of the phonon decay width γ_q as a function of E_F. These behaviors give us important and accurate information on the relevant Raman scattering processes, *i.e.*, whether a given Raman feature involves zone-center $q = 0$ phonons or if it is rather a DRR process involving $q \approx 2k$ wavevector phonons [37]. We show that, by combining the DDR theory with these anomalous phonon renormalization effects, we obtain a new technique of Raman spectroscopy for the assignment of combination phonon modes and overtones in monolayer graphene.

The Raman measurements were done in the back scattering configuration using a 2.10 and 2.16 eV (590 and 575 nm, respectively) dye laser, a 2.33 eV (532 nm) Nd:YAG laser, and a 2.54 eV (488 nm) Argon laser, with a 100 × objective and laser power around 1.5 mW to avoid heating effects. The device was fabricated as described in Section 4.1. Back gate measurements were done near room temperature with voltages in the range from -70 to 70 V.

Fig. 5.4(a) shows the combination modes in the spectral region from 1700 to 2300 cm^{-1} for four different laser lines: 488 nm, 532 nm, 575 nm and 590 nm. Each spectrum was fitted with five Lorentzians, in agreement with the number of peaks proposed by Rao *et al.* [67]. The experimental frequency dispersion of the five peaks taken from the fitting procedure applied to the Raman features in Fig. 5.4(a) were plotted together with the theoretical phonon dispersions of 1LG adapted from Popov and Lambin [27] (see Figs. 5.4(b) and (c)). The symbols correspond to the frequencies of peaks 1 to 5 for each E_L along the high symmetry $K\Gamma$ and KM directions. Squares, circles, triangles, diamonds and stars denote peaks 1 to 5, respectively. The full lines are the theoretical phonon branches [27] for the combination modes LO+iTA (black), iTO+LA (red), LO+LA (blue), oTO+iTO (purple), oTO+LO (grey) and iTO+iTA (green). The peak numbers given in Fig. 5.4(a) are written below the corresponding phonon branch assigned to each combination mode. When the peaks can be fitted to a phonon dispersion for either direction of $K\Gamma$ or KM, we can assign the peak to the corresponding combination mode.

In Fig. 5.4(c), the experimental data were plotted considering the phonon assign-

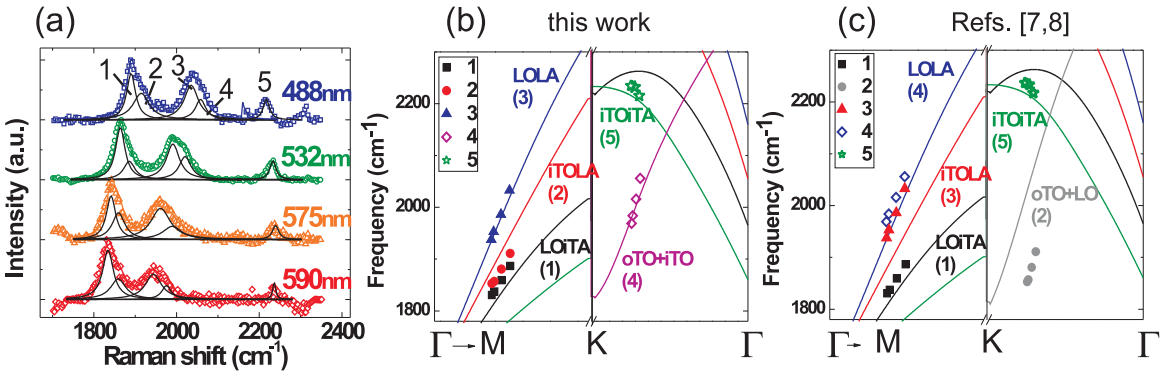

Figure 5.4: (a) The Raman spectra for the combination modes in the frequency region from 1700 to 2300 cm^{-1} for four different laser lines: 488 nm (2.54 eV), 532 nm (2.33 eV), 575 nm (2.16 eV) and 590 nm (2.10 eV). (b) and (c) Phonon dispersion of 1LG (solid lines) adapted from Popov and Lambin [27] showing the phonon branches combinations LO+iTA (black), iTO+LA (red), LO+LA (blue), oTO+iTO (purple), oTO+LO (grey) and iTO+iTA (green) near the Γ and the K point. (b) The phonon assignments of the present work for the experimental results obtained from the spectra in (a). Squares, circles, triangles, diamonds and stars correspond to peaks from 1 to 5, respectively. The peaks 1, 2 and 3 come from an intravalley DRR process, while the peaks 4 and 5 come from an intervalley DRR process. (c) The experimental data from this work plotted considering the assignments proposed in the literature [67,68]: peaks 1, 3 and 4 coming from an intravalley DRR process and the peaks 2 and 5 coming from an intervalley DRR process. The peak numbers are written below the corresponding phonon branch assigned to it.

ments reported in the literature by Cong *et al.* [68] and by Rao *et al.* [67]: peaks 1, 3 and 4 coming from an intravalley DRR process and the peaks 2 and 5 coming from an intervalley DRR process. Fig. 5.4(c) shows that the assignments proposed in the literature [67,68] for the peaks 1 and 5 as LO+iTA around the Γ point and as iTO+iTA around the K point, respectively, are in good agreement with the theoretical curve as regards both the frequency values and dispersion slopes. On the other hand, we can clearly see that peak 2 does not match well the proposed [67] assignment of the oTO+LO combination mode around the K point, and the peak 3 is not in good agreement with the combination phonon branch iTO+LA around the Γ point. Due to the small energy difference between peaks 3 and 4 (around 30 cm^{-1}) and the similar dispersion values (see Table 5.1), there is an ambiguity in the experimental assignment when made by using only laser dependent measurements, as is now in common usage.

Here, we propose different assignments for the peaks 2, 3 and 4, which are based on and supported by phonon self-energy renormalization calculations and by angle depen-

Table 5.1: Combination mode assignments, including region in the BZ, scattering directions and dispersion (cm^{-1}/eV) for the five $q \neq 0$ combination Raman modes in single layer graphene (1LG) from this work and from works published in the literature [67,68].

Peaks (ω_q cm^{-1})[1]	1 (1887)	2 (1913)	3 (2036)	4 (2064)	5 (2214)
This work	LO+iTA	iTO+LA	LO+LA	oTO+iTO	iTO+iTA
BZ point	Γ	Γ	Γ	K (KΓ)	K (KM)
Dispersion	128 ± 2	135 ± 6	213 ± 5	214 ± 5	-50 ± 5
Cong *el al.* [68]	LO+iTA	-	iTO+LA	LO+LA	-
BZ point	Γ		Γ	Γ	
Dispersion	140		198	221	
Rao *el al.* [67]	LO+iTA	oTO+LO	iTO+LA	LO+LA	iTO+iTA
BZ point	Γ	K	Γ	Γ	K
Dispersion	135	150	204	223	-56

[1]All the peak position references were taken with the laser line 488 nm (2.54 eV).

dent el-ph scattering matrix element calculations, that provide more precise information that was not considered in the previous works [67,68]. It is worth commenting that these angle dependent scattering calculations give us the direction along which the scattering processes have the highest probability of happening (see the brightest spots in the calculated Figs. 5.5(d)-(f), where θ_i and θ_f are, respectively, the initial and final scattering angles at the K point measured from the k_x axis). Here we select the phonon dispersion in the direction of q ($q = k_i - k_f$) that gives the maximum el-ph matrix element. From Fig. 5.4(b), we can see that the experimental peak 2 (red circles) is in better agreement with the combination phonon branch iTO+LA around the Γ point. Also, as shown in Fig. 5.4(b), by comparing the experimental and the theoretical phonon dispersions, we can see that peak 3 matches more accurately the phonon branch LO+LA around the Γ point, while peak 4 is in good agreement with the intervalley DRR process around the K point involving the oTO+iTO phonons. In Table 5.1 we summarize the new assignments found in this work and compare them to the assignments published in the literature for 1LG [67,68]. Also given in Table 5.1 are values for the E_L-dependent phonon dispersion rate ($\partial\omega/\partial E_L$) for each combination mode. The most likely el-ph scattering directions are also addressed for the intervalley DRR processes assigned in this work and included in the table as $K\Gamma$ and KM.

In order to make reliable combination mode assignments, it is also important to specify the direction along which the scattering process is happening. As discussed above, we have assigned the peaks 4 and 5, respectively, as oTO+iTO and iTO+iTA $q \neq 0$

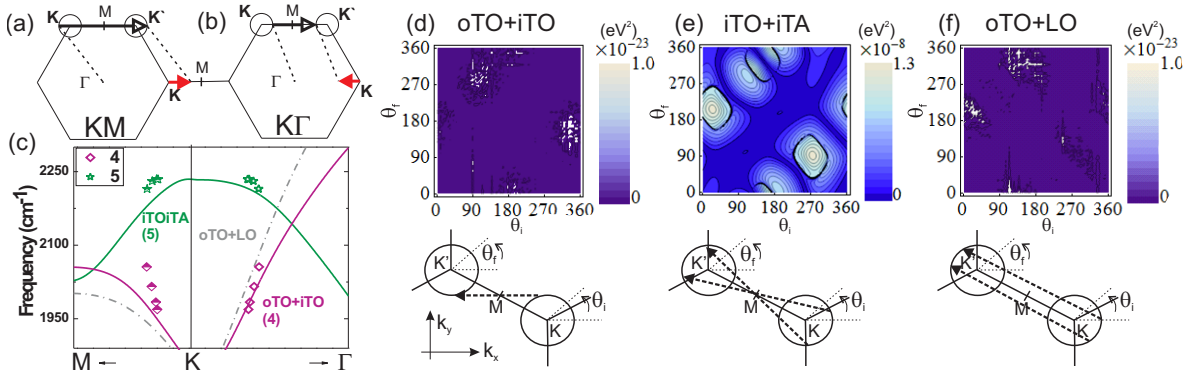

Figure 5.5: DRR processes involving phonons in the (a) KM or in the (b) $K\Gamma$ direction, respectively, measured from the K point (red full arrows). (c) The phonon dispersion relation for the two intervalley combination modes: peaks 4 (purple diamonds) and 5 (green stars)). The half colored symbols correspond to the DRR process in the KM direction and the open symbols correspond to the DRR process in the $K\Gamma$ direction. The absolute value for the angular dependence of the intervalley el-ph scattering matrix elements for the (d) oTO+iTO, (e) iTO+iTA and (f) oTO+LO phonon combination modes for $E_L = 2.54\,\text{eV}$. θ_i and θ_f are, respectively, the initial and final scattering angles. The diagrams in (d), (e) and (f) show the scattering directions for which the el-ph matrix elements are maximum [76].

combination modes around the K point generated by an intervalley process. However, the phonon wavevector which is mainly involved in the DRR process lies along either the KM or the $K\Gamma$ directions (considering the high symmetry directions, for simplicity) measured from the K point [74,75] (see Figs. 5.5(a) and (b) for the distinction between a $K\Gamma$ and a KM process). In Fig. 5.5(c) we plot the experimental phonon dispersion for peaks 4 and 5 considering both the KM and $K\Gamma$ directions. Besides the different attributions among the various peaks, our results differ from the results in the literature [67,68] specially because we use the oTO+iTO combination mode instead of the oTO+LO combination mode proposed in Refs. [67].

Fig. 5.5(c) shows that for peak 4, the agreement between the experimental data and the theoretical phonon dispersion strongly suggests that the scattering events are happening in the $K\Gamma$ direction. However, it could be hard to decide whether it is the oTO+LO or the oTO+iTO that is the correct assignment for this phonon mode, since the frequencies of these combination modes and their dispersions are very close to each other. In our assignment, we use the fact that the directions of the maximum el-ph matrix elements, as well as their phonon self-energy corrections studied by varying E_F (as shown later in the text), are different for oTO+LO and oTO+iTO. Figs. 5.5(d), (e) and (f) show

the absolute values for the angular dependence of the intervalley el-ph matrix elements for the oTO+iTO, iTO+iTA and oTO+LO phonon combination modes for $E_L = 2.54\,\text{eV}$, where θ_i and θ_f are, respectively, the initial and final scattering angles defined at the K and K' points. The diagrams in Figs. 5.5(d)-(f) show the scattering directions for which the el-ph matrix elements are maximum (brightest spots in the figures) for the corresponding combination mode. Looking at the el-ph matrix elements for the oTO+iTO combination mode in Fig. 5.5(d), we can see that the direction for which the el-ph matrix elements are maximum is closer to the $K\Gamma$ direction. On the other hand, if we look at the scattering diagram for the oTO+LO combination mode in Fig. 5.5(f), the el-ph matrix elements are a maximum closer to the KM direction. From Fig. 5.5(c), we can see a better agreement of peak 4 along $K\Gamma$ than along the KM direction. Then, by first combining the el-ph matrix elements with the theoretical phonon dispersion, we can conclude that peak 4 comes from a DRR process involving the oTO+iTO phonon combination mode in the $K\Gamma$ direction. It is worth commenting that the matrix elements for the oTO+iTO and oTO+LO combination modes are much weaker than those for the iTO+iTA modes because the oTO mode does not have strong el-ph coupling in graphene.

In Fig. 5.5(c), the experimental data for peak 5 is seen to be close to the theoretical curve for both the $K\Gamma$ and KM directions and we must use other information to decide the direction for which the main contribution to the Raman scattering occurs. In this case, the correct assignment is also decided based on the phonon renormalizations, the theoretical predictions for the scattering processes and the most important el-ph matrix elements. In Fig. 5.5(e), we can see that the direction for which the iTO+iTA combination mode has a maximum is closer to the KM direction, from which we conclude that the main contribution to peak 5 comes from an intervalley DRR process in the KM direction.

Next, we explore the phonon self-energies and the el-ph coupling for those combination modes, which provide fundamental information about el-ph interactions and is also fundamental to verify the accuracy of the assignment procedure. Figs. 5.6(b)-(f), respectively, show the experimental data for the dependence of the phonon frequency ω_q (black solid triangles) and the phonon decay width γ_q (open dots) on V_g (or on the Fermi energy) for the five combination modes. The phonon frequencies of the combination modes are shown using the same scale so that a better comparison can be made regarding the strength of the phonon renormalization phenomena for each combination mode. The dashed lines are guides for the eyes. Fig. 5.6(a) shows the gate-modulated response of the G band, where we can see that, when the charge carrier density increases, ω_G undergoes a hardening, while the γ_G narrows, consistent with previous works [52,64].

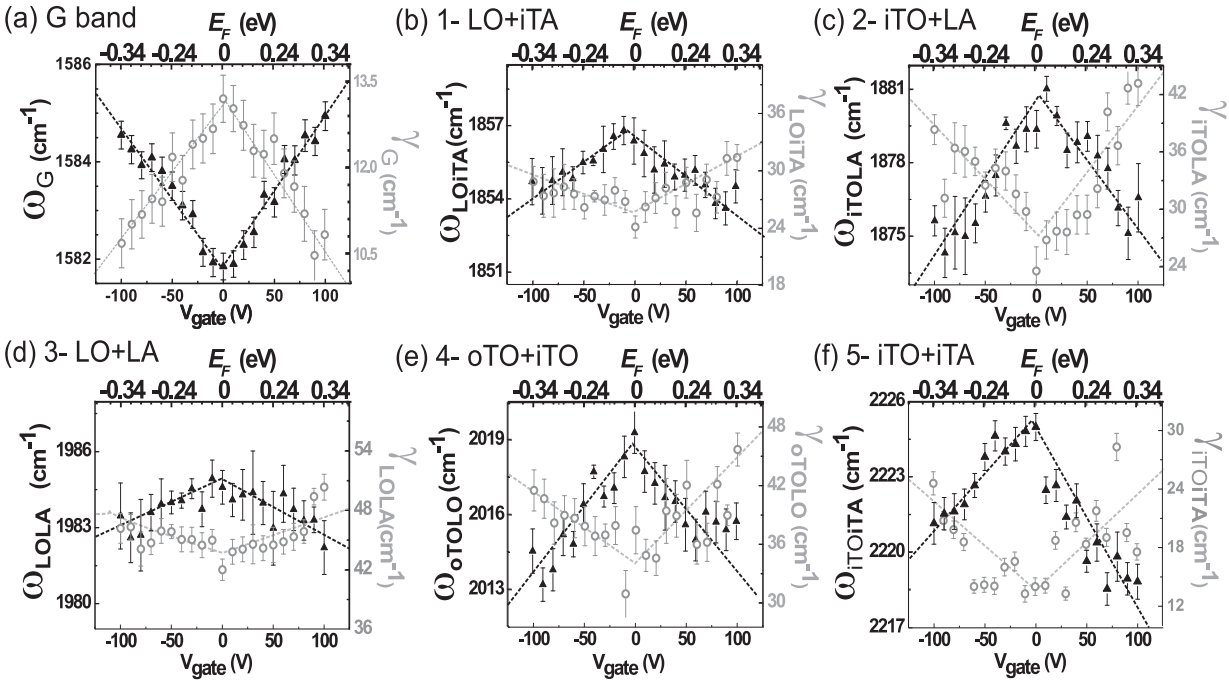

Figure 5.6: The dependence of the phonon frequency ω_q (black solid triangles) and phonon decay width γ_q (open dots) on gate voltage (V_g) for the (a) G band and phonon combination modes (b) 1, (c) 2, (d) 3, (e) 4 and (f) 5. All the graphics, except for the G band, are on the same scale for better comparison between the five combination modes. Notice that all five combination modes show a decrease of the ω_q and a broadening of the γ_q with increasing V_g. The dashed lines are guides for the eyes and the error bars come from the fitting procedure.

Also, the neutrality point can be estimated from the ω_G dependence. From Fig. 5.6(a) one can see that the minimum of the frequency occurs around 0 V, indicating the charge neutrality point.

In contrast, by observing Figs. 5.6(b) to (f), it is seen that ω_q is softened for all the five Raman combination features from 1700 to 2300 cm^{-1}, and that the ω_q softening is accompanied by a broadening of γ_q with increasing carrier concentration (increasing $|V_g|$). As explained in the last Section, this behavior observed for all five combination modes in the present study is common to Raman modes that come from an intravalley or intervalley DRR process with $q \approx 2k$ and is opposite to the behavior observed for the Γ point $q = 0$ phonons, such as for ω_G. In the case of $q \neq 0$, the electronic and vibrational density of states, together with energy and momentum conservation requirements, are determining if the el-h pair creation due to a $q \neq 0$ phonon absorption will happen or not. Namely, when the Fermi level is around zero, either no el-h pair can be created by the absorption

of a phonon or the probability of an el-h pair creation is very small because the density of states vanishes at the Dirac point. However, when the charge concentration increases, the renormalization of the phonon energy occurs by the creation of an el-h pair through the absorption of a phonon, then a softening of ω_q and a broadening of γ_q are observed, in contrast to what happens for $q = 0$ phonons at the Γ point [37].

The results in Figs. 5.6(b)-(f) confirm that the Raman combination modes come from a DRR process with $q \approx 2k$ phonons, in accordance with the predictions of the Ref. [37] and explanations given above. We also can see that the ω_q and γ_q renormalizations due to the change in the Fermi level position are weak for peaks 1 (Fig. 5.6(b)) and 3 (Fig. 5.6(d)), when compared to the other three peaks. In accordance to the assignments given to the peaks and since both of these peaks involve the LO phonon branch, we can conclude that the coupling of this phonon to all the other relevant phonon modes is not large compared to the other peaks. Moreover, the LO mode is not expected to show a strong el-ph coupling when **q** moves away from the Γ point (LO will present a strong coupling for $q = 0$ at the Γ point) [29], which confirms the reason for our assignments to peaks 1 (LO+iTA) and 3 (LO+LA). It is worth saying that the acoustic modes have zero (small) energy at the Γ point (around Γ point) so that a negligible contribution to the phonon renormalizations could be expected coming from these acoustic modes.

On the other hand, the ω_q and γ_q renormalizations for the peaks 2, 4 and 5 are of the same order of magnitude as that for the G band, which has a strong el-ph coupling [19,30,32,52,64]. The behavior observed for peaks 4 (oTO+iTO) and 5 (iTO+iTA) is due to the strong el-ph coupling of the iTO phonon branch expected for the K point phonons in 1LG. Another interesting observation: peak 2 (iTO+LA), which is a $q \neq 0$ mode around the Γ point, shows that the renormalizations due to the iTO mode become strong when moving away from the Γ point. This is fully consistent with what we observed for peaks 1 and 3 around the Γ point. While the LO mode renormalization weakens, the iTO mode renormalization is strengthened in moving away from the Γ point (remember that for $q = 0$ Γ point phonons LO has a strong renormalization while the iTO has not). The observed gate-dependent behavior consistently confirms the assignments given to the combination modes in this work, since there is a consistency between the phonon modes assigned to each peak and the strength of the el-ph coupling in each mode.

This result shows that the gate-modulated Raman scattering is indeed a powerful technique to confirm the phonon mode assignments attributed to Raman peaks when the gate voltage and E_L dependence are both measured. This is clearly the case for the peaks 3 and 4 in this work. It is worth mentioning that, especially as regards peak 4, the

gate-modulated results are important to decide which is the correct combination mode assignment for this peak. This feature could have been assigned to the oTO+LO phonon combination mode, as stated earlier [67]. However, if this assignment were correct, the el-ph coupling would be expected to be similar to what is seen in Figs. 5.6(b) and (d), which are combinations that contain the LO phonon mode. Note that the oTO mode is not expected to show a strong el-ph coupling [29]. The sizeable renormalization effect seen experimentally in Fig. 5.6(e) therefore strengthens the oTO+iTO choice for that feature.

5.2 Mixing of the optical modes in bilayer graphene

In this section we will show experimental results about the electron-phonon interaction in bilayer graphene. In particular, it will be shown that the Raman spectroscopy together with gate voltage is a powerfull technique to estimate the degree of symmetry breaking of bilayer graphene (2LG) and to estimate the environment influence in a 2LG device.

Bilayer graphene has attracted a lot of attention recently because of its special low energy electronic dispersion, in which a tunable band gap can be opened by application of a transverse electric field (see Section 2.2.2) [3,10,26,77–81]. Such device is desirable for low energy photo-emitters and detectors possessing a high tunability by the control of charge concentrations on the graphene layers. Recent experimental demonstration of this tunable band gap in 2LG was based on the absorption measurements in the infrared region [10,80,81] or by electric transport measurements [78,79]. However the tunable band gap bilayer graphene device operation can be greatly influenced by the surrounding environment.

Typically, unintentional doping charges coming from the top and the bottom of the system can accumulate on 2LG, giving rise to an unintentional electric field which determines a non-homogeneous doping between the layers and the opening of a band gap in the band structure, without any applied external electric field [82]. In this work we use Raman spectroscopy to monitor the unintentional charge coming from the top and the bottom of the system, which gives information on the electrostatic environment of the sample and which helps to characterize the bilayer devices for further applications. The band gap opening and tunability in bilayer graphene is based on the application of an electric field E perpendicular to the layers, given by

$$E = \frac{(n_{top} - n_{bot})|e|}{\varepsilon_0} \tag{5.3}$$

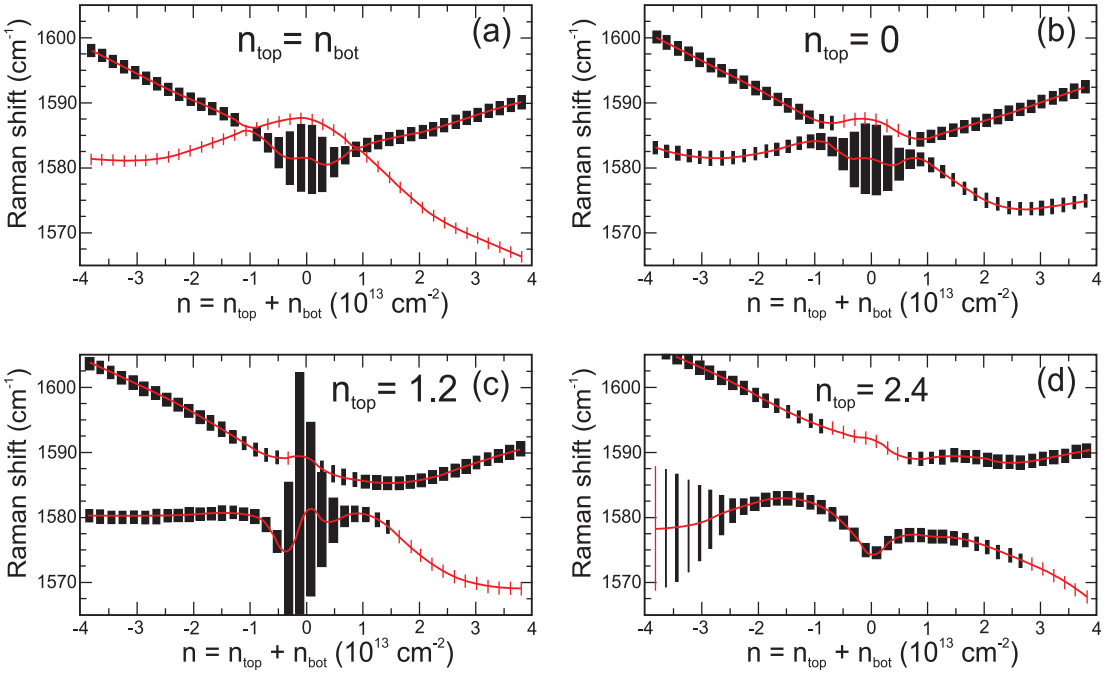

Figure 5.7: Raman shift in bilayer graphene as a function of the electron concentration n, for (a) $n_{top} = n_{bot}$, (b) $n_{top} = 0$, (c) $n_{top} = 1.2$ and (d) $n_{top} = 2.4$ calculated by Gava *et al* [82]. Calculated values of the shifts are connected by lines. For a given value of n there are two phonon modes represented with two rectangles. The height of the rectangles is the decay width and the areas are proportional to the relative Raman intensities (*i.e.*, the integrated area of each peak) of the two modes. Thus, the ratio of the widths of the two rectangles is equal to the ratio of the maximum heights of the two Raman peaks. When the ratio is less than 0.1, the mode with the smallest intensity is red, otherwise is black. Figure adapted from Ref. [82].

where n_{top} and n_{bot} are the charge carriers densities coming from the top and the bottom layers of 2LG, respectively, ε_0 is the vacuum permittivity, and e is the electronic charge ($e = -|e|$). Raman spectroscopy has already shown to be a fast and non-destructive tool to characterize graphene samples [16,41] and doping effects [25,32,52,64,83], however no carefully analysis has been done to demonstrate the effect of non-homogeneous doping in 2LG devices.

Recent theoretical calculations made by Gava et al. [82] suggest that from the analysis of the Raman spectra of gated bilayer graphene it is possible to quantitatively identify the amount of non-intentional charges coming from the atmosphere and from the substrate and to characterize the electrostatic environment of few-layers graphene. According to Gava et al. [82], the dependence of the two peaks of the G band of bilayer graphene is different depending on the initial doping of the two layers. The Raman shift

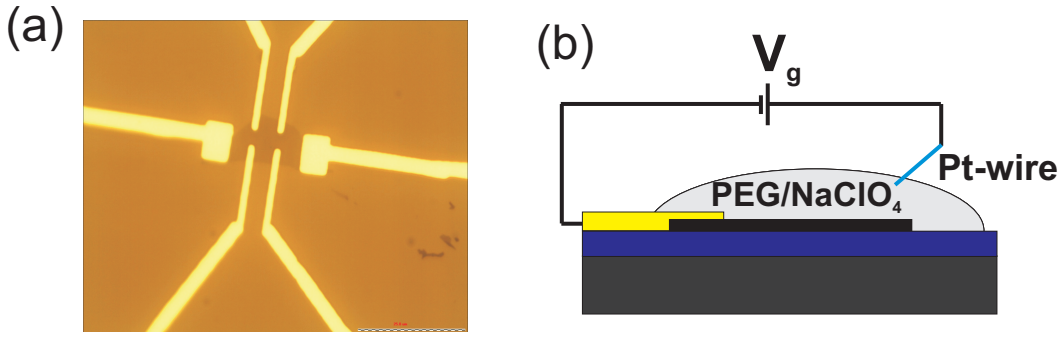

Figure 5.8: (a) Optical microscope image of the graphene sample before application of the polymer electrolyte. (b) Schematic illustration of the device and the experimental setup.

as a function of the electron concentration is shown in Fig. 5.7 for four different values of n^0_{top}.

In this section we study the dependence of the G band of bilayer graphene on the gate voltage. From the direct comparison between the experimental and the theoretically simulated Raman spectra, and from the analysis of the frequency ω, decay width γ and relative intensities I of the Raman features as a function of the electron concentration n, we were able to estimate the charge unintentionally accumulated on the device from the environment. Fig.5.8(a) shows the bilayer graphene field-effect transistor (FET) used in the experiment. The device was produced as explained in Section 4.1 and top gating was performed by using a polymer electrolyte consisting of polyethylene glycol (PEG) and $NaClO_4$ with ratio concentration of 1:0.25. The Raman measurements were done in the back scattering configuration at room temperature using 2.41 eV as excitation laser energy. The spot size of the laser was $\sim$1 μm using a 80$\times$ objective and the laser power was kept at 1.4 mW.

Capacitance measurements of the polymeric electrolyte used in the experiment were performed by Impedance Spectroscopy with frequency analyzer AUTOLAB PGSTAT30 by using a symmetrical cell with two Au electrodes and a polymer electrolyte layer. The impedance (Z) measurements for the electrolytes were carried out with frequency ranging from 50 kHz to 0.5 Hz at 0 V with 10 mV amplitude. The expression $Z = 1/i\omega C_G$, where ω is the frequency, was used to determine the capacitance C_G and the value obtained for capacitance per unit area for the interface electrolyte/bilayer was $C_G = 1.5 \times 10^{-6}$ F cm^{-2}. However, the shape and the thickness of the dielectric double layer depend on the specific surface at contact with the electrolyte. Therefore, from the measured value of impedance,

we can only have the order of magnitude of C_G of the electrolyte in contact with bilayer graphene. We can see that the order of magnitude of the capacitance is in accordance with the predictions for the top gate systems using polymer electrolyte (see Section 4.3) [52].

In the case of 2LG with AB layer stacking, both the electronic and phonon bands split into two sub-bands [28]. The E_{2g} phonon mode of monolayer graphene splits into two distinct modes, associated with the in-phase (IP) and out-of-phase (OP) displacements of the atoms in the two layers with respect to inversion symmetry [34]. The IP and OP modes belong to the two double degenerated representation E_g and E_u of the D_{3d} point group, respectively [34–36,82]. The E_u mode is not Raman active and, therefore, the G band of isolated bilayer graphene is composed of only one peak. However, when the two layers of bilayer graphene have different charge carrier concentration, induced by the application of an external gate voltage, the inversion symmetry of bilayer graphene is broken, lowering the symmetry of the system. As a consequence of the induced asymmetry between the two layers, the two IP and OP modes are mixed each other, and the two new eigen-modes have the Raman active IP component. Therefore, two peaks are observed in the G band of bilayer graphene [34–36,82] (more details are available in Section 2.4.4).

In Fig.5.9(a) we show the experimental Raman spectra (red dashed curves) taken with the application of top gate voltage (V_g) from -1.50 to 1.00 V. The G band splitting into two components G^+ and G^- (higher and lower frequency peak, respectively) can be clearly observed for V_g below -0.6 V. In this work we compare our experimental spectra with theoretical calculations from Ref. [82]. In particular, in Ref. [82] the authors considered the Γ phonon self-energy in order to compute the electron-phonon coupling contribution to the variation of the frequency, broadening, and relative Raman intensity of the two phonon modes in bilayer graphene, as a function of the electron concentration n and as a function of the induced charge from the bottom of the system, n_{bot}. The phonon self-energy and the band structure of gated bilayer graphene are computed using a tight-binding scheme as described in details in Ref. [82]. In order to compare the experimental spectra and theoretical calculations, we need to convert V_g into electron concentration n using the expression

$$\beta V_g = (n - n_0)e\,. \tag{5.4}$$

The total capacitance per unit area β, which includes the quantum capacitance C_Q and geometrical capacitance C_G [52], and the intrinsic doping at the zero gate n_0 are used as fitting parameters. Moreover, by the comparison between experimental and theoretical results from Ref. [82] we can estimate the charges unintentionally adsorbed, at zero gate,

from the top and bottom layers of the device, n^0_{top} and n^0_{bot} respectively. These quantities are related to n_0 by

$$n_0 = n^0_{top} + n^0_{bot}\,, \tag{5.5}$$

and therefore we only used n^0_{bot} as additional fitting parameter. n^0_{bot} and n_0 are the two independent fitting parameters characterizing the charge transfer on the system. Finally, the theoretical decay width γ_{th} calculated as a function of n and n^0_{bot} is given by electron-phonon and anharmonic phonon-phonon interaction [82]. Therefore, in order to take into account other factors determining a finite lifetime and neglected in the calculations, we used in the fitting procedure a parameter γ^0, independent on the total charge n and equal for the two peaks, related to the total decay line width by $\gamma = \gamma_{th} + \gamma^0$.

In Fig.5.9(a) we show the comparison between the experimental spectra (red dashed curve) and the theoretical calculation (black continuous curve). For each V_g, the theoretical spectra is obtained as the sum of two Lorentzians, $L^+(\omega)$ for the G^+ peak and $L^-(\omega)$ for the G^- peak. The two Lorentzians are centered in $\omega^{+/-}$, with decay width $\gamma^{+/-} = \gamma^{+/-}_{th} + \gamma^0$, and with integrated area $I^{+/-}$, as follows:

$$L^{+/-}(\omega) = \frac{I^{+/-}(\gamma^{+/-}/2)}{(\omega - \omega^{+/-})^2 + (\gamma^{+/-}/2)^2}\,. \tag{5.6}$$

$\omega^{+/-}$, $\gamma^{+/-}_{th}$, and $I^{+/-}$ are evaluated according to the theory from Ref. [82], where they are calculated as a function of n and n^0_{bot}. In order to convert n and n^0_{bot} into V_g we have used Eq. 5.4. In particular, we have used two different parameters, β^+ and β^-, for positive and negative V_g, respectively, which induce positive and negative n, *i.e.*, electron and hole doping charge. The fit is performed computing the χ^2, *i.e.*, the square of the difference between the experimental and theoretical spectra, averaged over all the measured Raman range and over different V_g. We considered V_g in the range of $\pm 0.5\,\mathrm{V}$. This choice is motivated by the fact that for large values of V_g the linear relation between gate voltage and charge could be modified, and charges from the electrolyte could accumulate on the bottom of the sample, making the fit results less reliable. The values for the parameters used in the fit, *i.e.*, β^+, β^-, n_0, n^0_{bot}, and γ^0, are varied in uniform and dense grids.

Fig.5.9(a) shows the best fit (black solid curves) obtained for the experimental data.

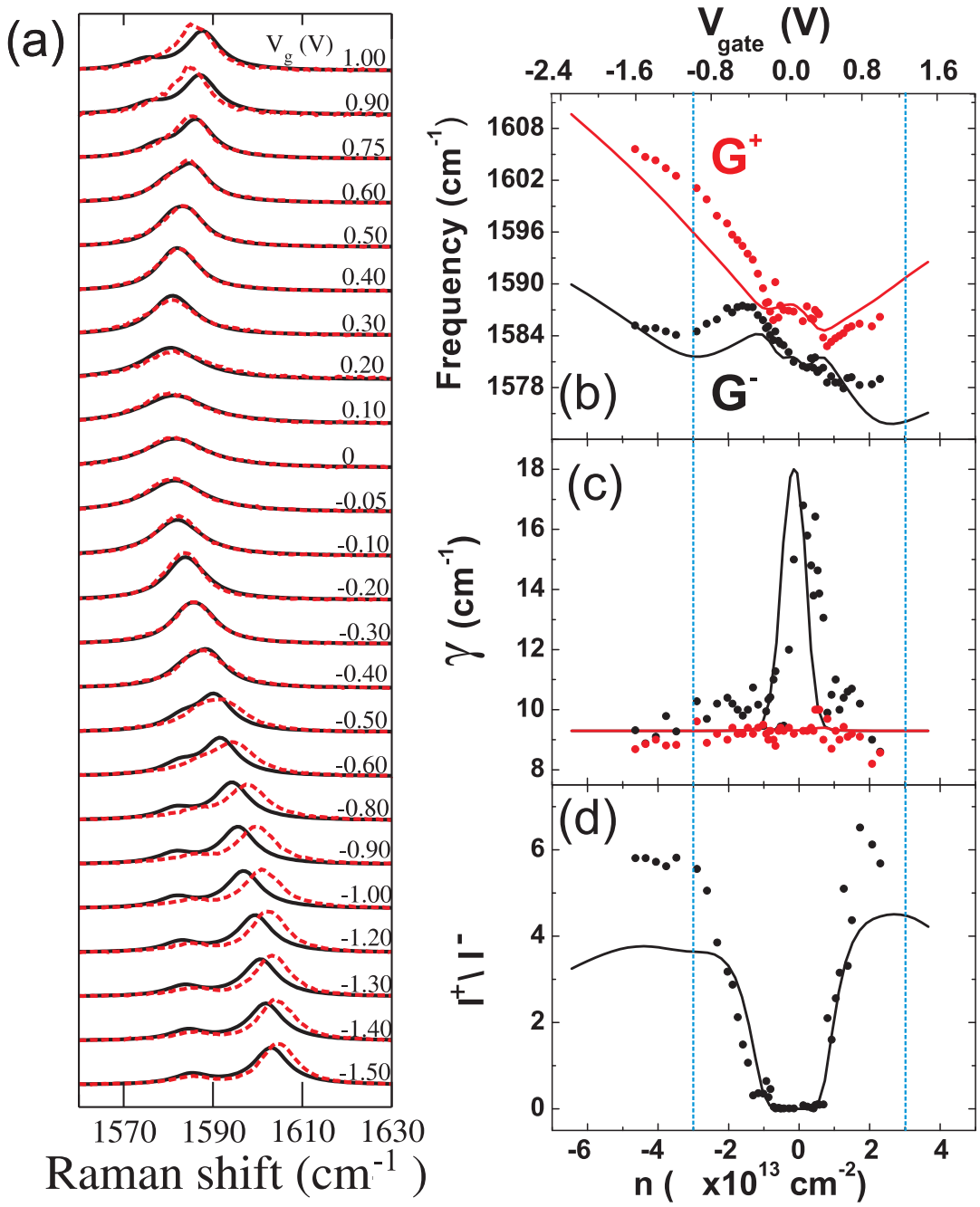

Figure 5.9: (a) Comparison between experimental (red dashed line) and theoretical (black continuous line) spectra for different V_g as obtained from the direct fit of spectra; (b-c-d) Frequency $\omega^{+/-}$, decay width $\gamma^{+/-}$ and ratio of intensity $I^{+/-}$ as obtained fitting the experimental spectra with two Lorentzians and compared with theory. The dots are the experimental data and the full curves are the theoretical calculations from Ref. [82]. The blue dashed line corresponds to the values of n to which we expect a jump in the quantum capacitance.

For this fit, the values of the fitting parameters are:

$$\begin{aligned}
\beta^{+} &= (3.7 \pm 0.2) \times 10^{-6}\,\mathrm{F\,cm^{-2}}\,, \\
\beta^{-} &= (4.6 \pm 0.2) \times 10^{-6}\,\mathrm{F\,cm^{-2}}\,, \\
n_0 &= (-0.15 \pm 0.02) \times 10^{13}\,\mathrm{cm^{-2}}\,, \\
n_{bot}^{0} &= (0.00 \pm 0.02) \times 10^{13}\,\mathrm{cm^{-2}}\,, \\
\gamma^{0} &= (7.5 \pm 0.1)\,\mathrm{cm^{-1}}\,.
\end{aligned}$$

The different values of β^{+} and β^{-} can be ascribed to the different mobilities of the positive (Na^{+}) and negative (ClO_4^{-}) ions. For this values found for β, the range of V_g used in the experiment, from -1.6 V to 1.0 V, corresponds to a change in the Fermi level position of about -0.51 eV to 0.38 eV and a change in the charge concentration of about $-4.7 \times 10^{13}\,\mathrm{cm^{-2}}$ to $2.3 \times 10^{13}\,\mathrm{cm^{-2}}$. Notice that the agreement between the experimental and simulated spectra is excellent in the range -0.5 to 0.5 V. The slight shifts out of this range can be ascribed to a possible hysteresis in the experiment, and to the fact that we did not consider in our model the expected jump of the quantum capacitance C_Q when, increasing (decreasing) the Fermi level, we reach the second conduction (valence) band in bilayer graphene [52]. The Fermi level value to when the second conduction (valence) band starts to be filled (emptied) is ± 0.4 eV [44,84]. This corresponds to a charge concentration of about $n = \pm 3 \times 10^{13}\,\mathrm{cm^{-2}}$ (see the blue dashed vertical line in Figs.5.9(b)-(d)), and according to our values of n_0 obtained from the fit, the gate values at which the jumping of the quantum capacitance is expected are around $V_g = 1.3$ V for positive gate voltage and $V_g = -1.0$ V for negative gate voltage.

The fact that $n_{bot}^{0} = 0$ shows that the amount of charge transferred from the substrate to the bottom layer of the sample in this case is negligible. On the other hand, the unintentional doping concentration found for the top layer is $n_{top}^{0} = -0.15 \times 10^{13}\,\mathrm{cm^{-2}}$. Although it is known that the polymer electrolyte diminishes both hysteresis and influence of external effects, such as changes in gas adsorption from ambient [85], the polymer electrolyte layer itself can, for instance, contain residual water or absorb water from the humid air [86], and this will contribute to an unintentional charge transfer, because water can diffuse through the polymer and be adsorbed in the graphene layer.

All the G band experimental spectra of Fig.5.9(a) were fitted using two Lorentzians in order to extract the frequency and decay width of the two components G^{+} and G^{-}, as well as the relative Raman intensity, *i.e.*, the ratio between the Raman intensities of the modes with higher frequency (I^{+}) and lower frequency (I^{-}). Figs.5.9(b) and (c)

show, respectively, the dependence of the G^+ (red dots) and G^- (black dots) frequency ω and width γ as a function of the electron concentration n. The full lines are the theoretical calculations based on Ref. [82]. The dependence of the frequency of the G^+ and G^- Raman peaks (Fig.5.9(b)) is well described by the calculation of the phonon self energy as a function of charge concentration. The distinct behaviors of the G^+ and G^- is qualitatively explained by the different electron-phonon couplings for the in-phase and out-of-phase phonon modes with inter-band and intra-band electron-hole pairs, as explained in Ref. [35] and in Section 2.4.4 (see Fig. 2.15 for theoretical predictions). While G^+ blueshifts with charge carrier concentration, the G^- mode redshifts when E_F is changed.

For the width dependence, while γ^+ does not change with n, γ^- is maximum near $n = 0$ and minimum for values of n corresponding to values of E_F larger than half of the phonon energy, as has been observed before in both monolayer and bilayer graphene. It is worth commenting that the scattered data points for the frequency, line width and relative intensity shown in Figs.5.9(b), (c) and (d) are mostly caused by charge carrier fluctuation during the measurement, where a hysteresis of the charge neutrality point is found by sweeping the gate voltage up and down. The shift of the neutrality point can reach 0.25 V in a range of 1 V of gate voltage due to hysteresis effect [87]. Fig.5.9(d) shows the dependence of I^+/I^- as a function of n. The quantity I^+/I^- shows a minimum value between $n \sim -1$ to $1 \times 10^{13}\,\mathrm{cm}^{-2}$ and increases more strongly for positive carrier concentration. The underestimation of the theoretical results for high negative and positive charge concentrations can be ascribed to the approximations made in the theoretical model. These results show how the Raman spectroscopy can be used to fully characterize the bilayer graphene device and its interaction with the environment.

5.3 Summary

In summary, we have shown experimental results of electron-phonon coupling in monolayer and bilayer graphene. For monolayer graphene, we have studied the phonon self-energy correction for phonon modes with $q \neq 0$ from a phenomenological and experimental point of view. In the $q \approx 2k$ cases (oppositely to what is observed for the $q = 0$ intravalley process), the phonon softening and damping is a minimum when $E_F = 0$ and increases with increasing $|E_F|$. For the intervalley $q = 0$ case (measured from the K point), $E^{eh} \sim 0$ and a weak and small $\omega_{\mathbf{q}}$ and $\gamma_{\mathbf{q}}$ dependence with E_F is expected. Due to these different phonon self-energy behaviors, gate-modulated resonant Raman spectroscopy of overtones and of a combination of phonon modes provides a powerful technique to assign

the phonons participating in the formation of each overtone or combination mode, to identify whether a Raman feature is associated with the $q = 0$ or the $q \neq 0$ processes and to determine how a given phonon mode is coupled to the electronic states of single layer graphene. We applied these combined techniques to study the G* and G$'$ modes. Our theoretical approach satisfactorily explains the experimental results and within this framework, we also showed that the G* mode is an asymmetric peak composed by both, the iTO+LA combination mode, which is an intervalley $q = 2k$ process with a strong phonon renormalization, and the 2iTO overtone mode, which is an intervalley $q = 0$ process with a weak phonon renormalization, thereby resolving a long-time discussion in the literature. This work is published in *Physical Review Letters* **109**, 046801 (2012).

The phonon renormalization for $q \approx 2k$ cases were also applied to five combination modes in the region from 1700 to 2300 cm^{-1}. By exploring the $q \neq 0$ phonon anomalous self-energy corrections and by comparing the experimental data with the theoretical phonon dispersion and making use of the angle dependent electron-phonon (el-ph) scattering calculations, we have assigned properly the five combination modes observed in this frequency region. For all five phonon combination modes, we observed a decrease of the phonon frequency and a broadening of the phonon decay width with increasing gate voltage occurs, as is predicted for a double resonance Raman process with $q \neq 0$. We show that the el-ph coupling is larger for peaks 2, 4 and 5 mostly due to the strong el-ph coupling of the iTO phonon branch. The renormalizations for peaks 1 and 3 are small due to the weak el-ph coupling of the LO phonon branch. These el-ph dependencies on gate voltage support our assignments when compared to the assignments in the current literature [67,68]. This work is under review in the *Nano Letters* journal.

For bilayer graphene, a detailed analysis of the top gated G band is presented. We observed that, unlike in the unbiased case where the G Raman band is composed by only one peak, the gate voltage breaks the inversion symmetry and the G band splits in two modes, that are combinations of the in-phase and out-of-phase modes of the unbiased bilayer graphene. We analyze the dependence of the frequency, line width and the relative intensities of the peaks with higher and lower frequency as a function of the electron concentration and we compared the experimental results with theoretical calculations from Ref. [82]. From this comparison, we could estimate the unintentional carrier concentration adsorbed on the device, at zero gate, from the substrate, n^0_{bot}, and from the electrolyte, n^0_{top}, and we found $n^0_{bot} = 0.0$ and $n^0_{top} = -0.15 \times 10^{13}\,\mathrm{cm}^{-2}$, showing that Raman spectroscopy is a powerful technique to study the electrostatic environment of graphene. This work is published in *Carbon* **50**, 3435 (2012).

Chapter 6

Probing the electronic and vibrational structure of bilayer graphene

Resonance Raman scattering (RRS) has been widely use to probe the electronic and the phonon structures of carbon materials like carbon nanotubes , graphite, diamond-like carbon and linear carbon chains [16]. Also, the double resonance G′ Raman band provide rich information about the energy and momentum of the participating electrons and phonons. In this chapter we review the combination of RRS and DRR processes to probe information about phonons and electrons in bilayer graphene. From the DRR model (see Section 3.3), we have a set of two coupled quantities: the electron and phonon frequencies and their dispersion relations. From the knowledge of one of these quantities (for example, the phonon energies and their dispersion), it is possible to get the other quantity (which, for this example, would be information about the electronic structure). The information comes from the experimental Raman band originated from a specific double Resonance scattering process. By changing the laser excitation energy, different points in momentum space for the electronic and phonon dispersion are probed, and in this way, it is possible to map the phonon or electronic dispersion relations by this method.

In recent years, the physics of monolayer graphene has been thoroughly investigated, unveiling a wealth of interesting and unusual properties, most of which are related to graphene's distinct electronic properties, consisting of a linear and isotropic dispersion of the electronic states around the Fermi level (E_F) near the K point in the Brillouin zone (BZ). On the other hand, bilayer graphene is also an interesting material. While in the unbiased bilayer the valence and conduction bands touch each other at the Fermi level,

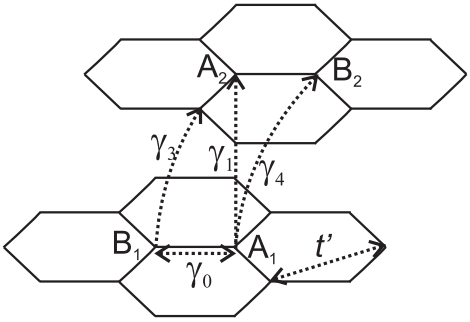

Figure 6.1: The intra- (γ_0 and t') and inter-layer (γ_1, γ_3 and γ_4) tight-binding parameters in bilayer graphene.

a gap can be opened and tuned, for example, by the application of an external electric field perpendicular to the layers [3,10,11,35], which makes bilayer graphene a promising system for the fabrication of nanoelectronic devices. However, the development of bilayer graphene based devices depends on the detailed understanding of its electronic properties.

Since the unit cell of AB stacked bilayer graphene is the same as that of graphite, we can model the bilayer electronic structure using a tight-binding model for graphite [21], by adapting the Slonczewski-Weiss-McClure (SWM) parametrization [22,23] of relevant couplings. There are several theoretical [24,88,89] and experimental [18,44,84,90–92] studies of the nearest-neighbors hopping SWM parameters, but the agreement between the reported values, obtained with different experimental techniques, is not entirely satisfactory. In a previous resonance Raman study of bilayer graphene performed in the visible range by Malard *et al.* [18], the electronic structure of bilayer graphene was probed by analyzing the dispersion of the G′ Raman band as a function of the laser energy, and the electronic band dispersion was described within a tight-binding approximation by determining the SWM parameters γ_0, γ_1, γ_3 and γ_4 (see Fig. 6.1). They [18] have shown that a linear iTO phonon dispersion provides a good fit of the experimental data obtained with visible photons.

In the present work, we have extended the range of laser energies, measuring the G′ Raman band with many laser lines in the range 1.33 to 2.81 eV (932 to 440 nm). We used He-Cd, Ar-Kr and dye lasers for the laser lines in the visible range 1.91-2.81 eV and a Ti:Sapphire laser (from Los Alamos National Laboratory - New Mexico - USA) for the excitation in the near-infrared (IR) range 1.33-1.72 eV. Fig. 6.2 shows the Raman G′ band of bilayer graphene recorded with 19 different laser lines between 1.33 and 2.81 eV. We can see that both the frequency and the shape of the G′ band are strongly dependent on the laser excitation energy E_L.

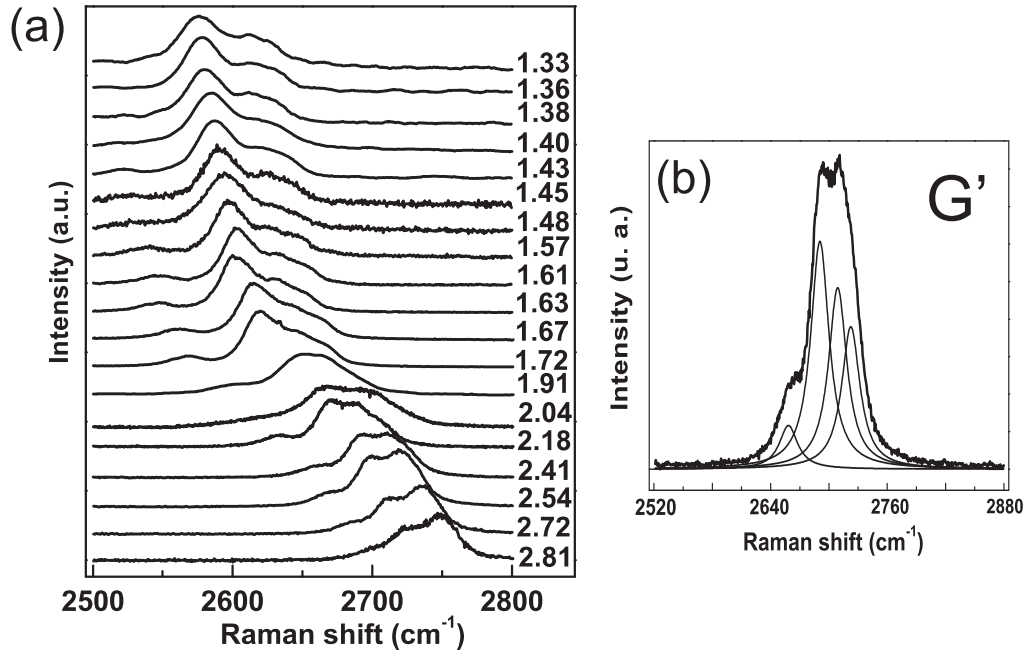

Figure 6.2: (a) The Raman G′ band of bilayer graphene recorded with 19 different laser lines between 1.33 and 2.81 eV (932 to 440 nm). (b) G′ Raman band of bilayer graphene measured with 2.41 eV laser energy and fitted with four Lorentzian peaks originated from the P_{11}, P_{12}, P_{21} and P_{22} processes.

The measurements in the near-IR range are especially relevant since we can probe phonons that are much closer to the K point. The analysis of the low energy data allowed us to observe a non-linear softening of the phonon branch near the K point, and the significant splitting of the symmetric (S) and anti-symmetric (AS) phonon branches. In particular, we show that the phonon softening is stronger for the symmetric branch. Concerning the electronic structure, we have also considered the in-plane second-neighbor hopping parameter t' (see Fig. 6.1), which is expected to be of the same order as the out-of-plane nearest-neighbor parameters, to describe the G′ Raman band dispersion. The parameter Δ, which represents the difference between the on-site energies of the sublattices A and B, was also taken into account.

6.1 The historical background

The G′ Raman band in graphene systems comes from an intervalley double resonance Raman process [39,40] that involves one initial electronic state with wavevector $\mathbf{k}$ near the K point, one intermediate electronic state with wavevector $\mathbf{k}'$ near the K' point,

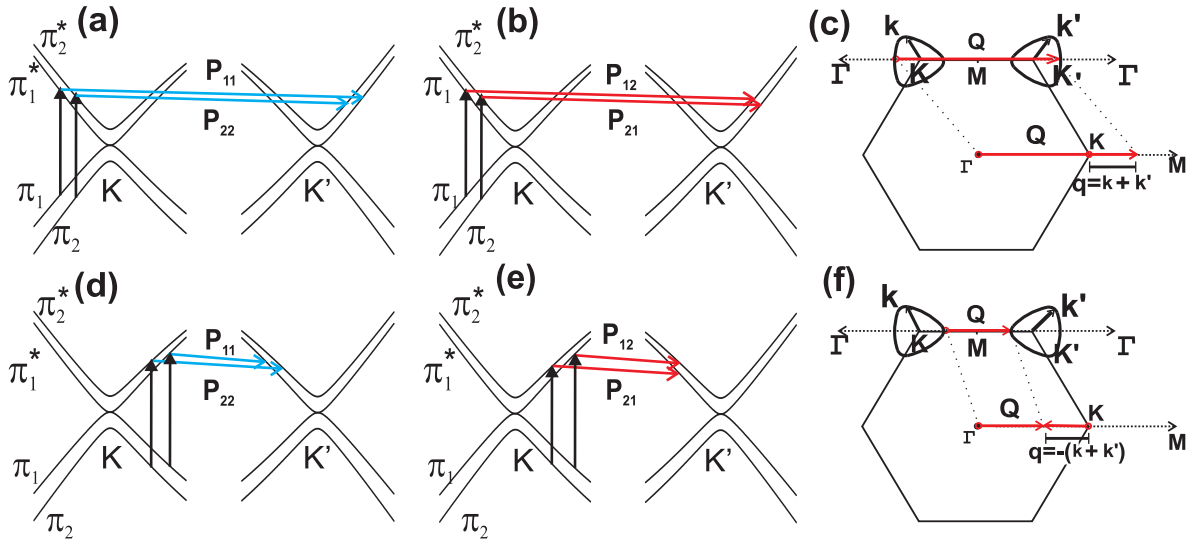

Figure 6.3: (a) P_{11} and P_{22} DRR outer processes involving the symmetric phonon. (b) P_{12} and P_{21} DRR outer processes involving the anti-symmetric phonon. (c) DRR outer process involves electrons in the $K\Gamma$ direction and phonons in the KM direction. (d) P_{11} and P_{22} DRR inner processes involving the symmetric phonon. (e) P_{12} and P_{21} DRR inner processes involving the anti-symmetric phonon. (f) DRR inner process involves electrons in the KM direction and phonons in the $K\Gamma$ direction.

and two in-plane transverse optical (iTO) phonons with wavevectors $q = k + k'$, measured from the K point (see Figs. 6.3(c) and (f)) [16]. Since photons with different energies excite electrons with different wavevectors $\mathbf{k}$, the DRR process probes phonons with different $\mathbf{q}$ values near the K point. Therefore, the dispersion of electrons and phonons can be investigated in a resonance Raman experiment, when the energy of the photons can be tuned [16].

In the case of bilayer graphene, there are two electronic valence bands (π_1 and π_2) and two conduction bands (π_1^* and π_2^*) [3]. There are also two iTO phonon branches, one related to the symmetric (S) and the other one with the anti-symmetric (AS) phonons, with respect to inversion symmetry. Group theory analysis for bilayer graphene predicts four distinct DRR processes, P_{11}, P_{22}, P_{12}, and P_{21}, which are illustrated in Fig. 6.3. The triangularly-shaped isoelectronic curves around the K and K' points in Figs. 6.3(c) and (f) are the equienergy contours of the π electrons involved in the scattering process. The value of the equienergy in a given DRR process is determined by the laser excitation energy E_L, that creates the electron-hole excitation. Since the lower and upper conduction bands (π_1^* and π_2^*) belong to different irreducible representations, the symmetric phonons (T_1 symmetry) are associated with the P_{11} and P_{22} DRR processes (Figs. 6.3(a) and (d))

involving electronic states with same symmetry ($\pi_1^* \rightarrow \pi_1^*$ or $\pi_2^* \rightarrow \pi_2^*$), whereas the anti-symmetric phonons (T_2 symmetry) occur for the P_{12} and P_{21} processes (Figs. 6.3(b) and (e)) involving electronic states with different symmetries ($\pi_1^* \rightarrow \pi_2^*$ or $\pi_2^* \rightarrow \pi_1^*$) [28].

Each one of these processes (P_{11}, P_{22}, P_{12} and P_{21}) is responsible for one peak in the G′ band. Fig. 6.2(b) shows the Raman spectrum of the G′ band measured with 2.41 eV laser energy and fitted with four peaks. All the peaks have the same decay width of $\sim 24\,\mathrm{cm}^{-1}$, which is the line width of the single G′ band in monolayer graphene [16,41]. If the analysis of the DRR process is done considering only backscattering of electronic states along the $K\Gamma$ direction with phonons along the KM direction (Fig. 6.3(c)), this process is called *outer* DRR process (scattering shown in Figs. 6.3(a) and (b)). On the other hand, if the analysis is done considering the scattering of the electrons along the KM direction with phonons along the $K\Gamma$ direction (Fig. 6.3(f)), this process is called *inner* DRR process (scattering shown in Figs. 6.3(d) and (e)).

In the literature, the analysis of the DRR process used to be done considering only the scattering of electronic states along the high symmetric ΓKM line. This restricted one-dimensional analysis of the DRR process rests on the following assumptions: (i) that a one-dimensional integration along the ΓKM direction captures the essential features of the DRR process, as found in Ref. [74]; (ii) that some of the graphically determined double-resonant $\mathbf{q}$ vectors, related to forward-scattering processes (connecting points on the electronic equienergy curves surrounding the K and K' points in Figs. 6.3(c) and (f)), vanish by destructive interference, as also found in Ref. [74]. (iii) that, by plotting the phonon density of states (PDOS) of graphene, for phonons satisfying the DRR process, one can identify a strong singularity at the phonon $\mathbf{q}$ vector involved in the outer process, and a much smaller PDOS value for the phonon $\mathbf{q}$ involved in the inner process [17]. This is the reason why attention is usually paid solely to the one-dimensional outer process [17,41,93]. While the analysis in Ref. [74] did consider both outer and inner processes, and the calculation of the Raman cross section considered all possible resonant and non-resonant processes, a critical approximation was employed: the matrix elements involved, related to electron-photon and electron-phonon couplings, were assumed to be constant and independent of the wavevectors $\mathbf{k}$ and $\mathbf{q}$ of the electrons and phonons, respectively.

Moreover, recent experiments [94,95] have shown that their results can only be explained if the inner process is the main responsible for the G′ feature. In both works [94,95], a comprehensive analysis by combining polarized Raman measurements with an analysis based on first-principles calculations of the changes in electronic energy bands and phonon dispersion of a single-layer graphene under homogeneous uniaxial strains is

presented and the dominant scattering path of the double resonance Raman scattering process is determined. Yoon *et al.* [94] and Mohr *et al.* [95] observed a splitting of the G′ band with increasing strain and they explained that the splitting, the shift rates, the polarization effects, and the crystallographic orientation dependence do not solely come from a movement of the Dirac cones or their deformation, but rather from an orientation-dependent softening of the involved iTO phonon branch. The large magnitude of the splitting can only be explained with phonons from the branches between the Γ and K points (phonons involved in the inner process) that contribute to the double resonant G′ mode.

This state of affairs indicates that some of the conventional wisdom related to the DRR process in carbon based systems needs to be reevaluated. In the present work, we analyze our experimental data considering both the outer and the inner process. For each approach, the SWM parameters are obtained through the analysis of the dependence of the G′ Raman band with the laser excitation energy E_L.

6.2 Experimental results

In order to understand the experimental results obtained in this work, it is important to build a bridge between experiment and theory. To achieve this, we must find a relation between the electronic and the phonon dispersions of bilayer graphene. The electronic dispersion of bilayer graphene can be described in terms of the standard SWM model for graphite, using a tight-binding model, as described in the Section 2.2.2 using Eq. 2.13 and Eq. 2.14 [21].

For any of the P_{ij} $(i, j = 1, 2)$ processes, we seek the dependence of the phonon energy E_{ph} with E_L. In the initial step of the DRR process (electron-hole pair creation), the incident photon is in resonance with the excitation of the electronic state from the valence to the conduction bands at the $\mathbf{k}_i$ point. In the following, we drop the vectorial notation for the $\mathbf{k}$ and $\mathbf{q}$ vectors, since we are considering only the ΓKM direction. The laser energy can then be written as:

$$E_L = E_{\pi_i^*}(k_i) - E_{\pi_i}(k_i) \,, \tag{6.1}$$

which allows us to determine the momentum k_i of the excited electron in the process. The electron is then scattered from a state in the vicinity of the K point to a state in the vicinity of the K' point by emitting an iTO phonon with energy

$$E_{ph}^{ij}(q_{ij}) = E_{\pi_i^*}(k_i) - E_{\pi_j^*}(k_j') \,, \tag{6.2}$$

where q_{ij} depends on k_i and k'_j. This equation uniquely determines the momentum k'_j of the scattered electron, provided that $E^{ij}_{ph}(q_{ij})$ is known. The phonon energy can be computed, and is directly related to the Raman shift for a specific P_{ij} process, obtained with a given E_L. Physically, the difference between the outer and inner processes lies in the phonon wavevector q_{ij}.

As can be inferred from the geometry in Figs. 6.3(c) and (f), $q_{ij} = k_i + k'_j$ for the outer process, and $q_{ij} = -(k_i + k'_j)$ for the inner process, both measured from the K point. In both cases, q_{ij} has a maximum amplitude of $\approx 2k_i$. The outer and inner processes have their vectors k_i and k'_j pointing in opposite directions. Interestingly enough, this means that calculations for the inner process can be done simply by switching k_i into $-k_i$ and k'_j into $-k'_j$ in Eqs. 2.13 and 2.14 and looking for values of k'_j satisfying Eq. 6.2.

In a previous resonance Raman study in bilayer graphene performed in the visible range by Malard *et al.* [18], the electronic bands were obtained by considering the first-neighbor parameters γ_0, γ_1, γ_3, γ_4 considering the outer process. A linear phonon dispersion was used in this previous study [18] to fit the G′ peak frequencies versus E_L data. Fig. 6.4(a) shows the fitting of the data of the present study (data from Fig. 6.2(a)), fitted with four Lorentzians, considering the linear phonon dispersion and the SWM parameters used in reference [18]. We can see that this fit fails for the experimental data in the near-IR region and, in particular, for the data associated with the lower energy phonon, that involves phonons closer to the K point.

In order to fit the low energy experimental data in Fig. 6.4, we consider a non-linear relation for the iTO phonon dispersion, given by a second-order polynomial ($w(q) = A + Bq + Cq^2$) where A, B and C are fitting parameters. Fig. 6.4(b) shows the fit considering the same phonon dispersion for the symmetric and anti-symmetric phonon branches, and the γ_0, γ_1, γ_3, γ_4 parameters, also considering the outer process as Ref. [18]. Fig. 6.4(c) shows the fit using the same SWM parameters as in Fig.6.4(b) but considering two distinct phonon dispersions for the symmetric and anti-symmetric branches. As we can see in Figs. 6.4(b) and (c), the fitting in the low energy range is improved considering the non-linear dispersion, but different dispersions for the S and AS branches are needed to obtain a good fit of the experimental data. All fitting parameters of Fig. 6.4 (that considers the outer process) are shown in Table 6.1.

In the fittings shown in Figs. 6.4(a)-(c), we have considered only the first-neighbor parameters γ_0, γ_1, γ_3, γ_4. In principle, we could also introduce higher-order terms and, in particular, the in-plane second-neighbor interaction t', which is expected to be of the same order of magnitude as the out-of-plane first-neighbor interaction. Fig. 6.4(d) shows the fit

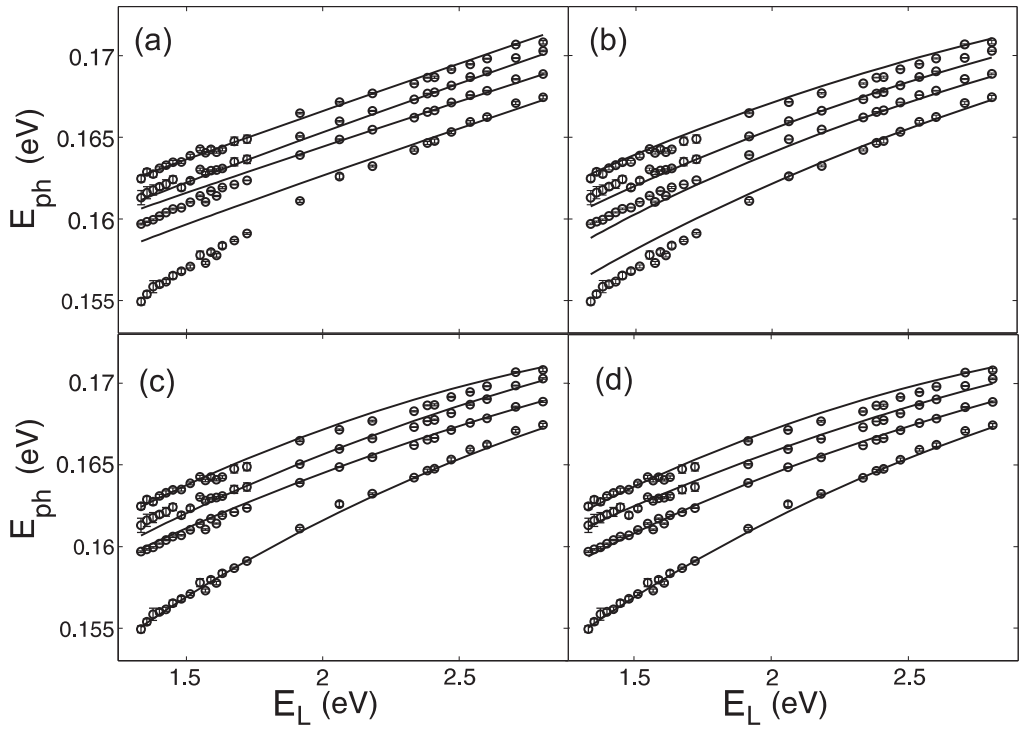

Figure 6.4: Laser energy dependence of the peaks of the G′ bands, fitted considering the outer process and three different approximations: (a) linear phonon dispersion and the SWM parameters γ_0, γ_1, γ_3, γ_4 (same approximation as in Ref. [18]); (b) same non-linear phonon dispersion for the symmetric (S) and anti-symmetric (AS) phonon branches, and the SWM parameters γ_0, γ_1, γ_3, γ_4; (c) non-linear and distinct phonon dispersions for the S and AS phonon branches, and the same SWM as in (b). (d) Fitting using the same phonon dispersion as in (c), the first-neighbor SWM parameters γ_0, γ_1, γ_3 and γ_4, second-neighbor in-plane t' parameter and the Δ parameter, which represents the difference in energy of sublattices A and B. All fitting parameters used in approximations (a), (b), (c) and (d) are shown in Table 6.1.

Table 6.1: Values of the SWM parameters (in units of eV) and the iTO phonon dispersion parameters ($w(q) = A+Bq+Cq^2$) obtained from the three different fits of the experimental data shown in Figs. 6.4(a), (b), (c) and (d) and considering outer process.

							symmetric			anti-symmetric		
	γ_0	γ_1	γ_3	γ_4	Δ	t'	A(meV)	B(meV$\AA$)	C(meV$\AA^2$)	A(meV)	B(meV$\AA$)	C(meV$\AA^2$)
(a)	2.9	0.30	0.1	0.12	-	-	153.7	38.5	-	154.0	38.8	-
(b)	3.0	0.35	0.1	0.15	-	-	149.3	69.5	-46.6	149.3	69.5	-46.6
(c)	3.0	0.35	0.1	0.15	-	-	146.3	86.9	-70.3	150.5	66.3	-44.8
(d)	3.0	0.35	0.1	0.10	0.01	0.15	146.3	86.9	-70.3	150.5	66.3	-44.8

of the experimental data considering also the t' and Δ, which represents the difference in energy of the sublattices A and B. As we observe in Fig. 6.4(d), the resultant fit is slightly improved, mainly due to the use of larger number of fitting parameters.

It is important to emphasize that different values of the γ parameters are found when we include t' and Δ. Therefore, the numerical values of the tight-binding parameters obtained from the fit of the experimental data depends on the approximation used to analyze the data. For the outer process, a good fit can always be obtained for γ_0 values ranging between 2.9 and 3.1 eV. Concerning the γ_1 parameter, reasonable fits could only be obtained for $\gamma_1 < 0.35$ eV, which is slightly smaller than that usually found in the literature $\gamma_1 \approx 0.40$ eV [24,44,84] from other techniques and calculations. However, the major discrepancy is in the value of γ_3. The best fit is obtained when $\gamma_3 \approx 0.1$ eV, and a reasonable fit cannot be obtained for values of $\gamma_3 > 0.15$ eV. Once again, this value is smaller than others found in the graphite literature ($\gamma_3 \approx 0.30$ eV [89,96,97]). Also recent infrared measurements in exfoliated bilayer graphene consider $\gamma_3 \approx 0.30$ eV [24,88].

If we consider only nearest neighbor parameters, the best fit is obtained for $\gamma_4 \approx 0.15$ eV, which is in close agreement with previous experiments [18,44,84]. However, smaller values of γ_4 provide a good fit when the second-neighbor t' parameter is included. In fact, both γ_4 and t' parameters are associated with the asymmetry between electrons and holes in bilayer graphene. Finally, reasonable fits can be obtained for different small positive and negative values of Δ ($|\Delta| < 0.01$eV).

Due to the discrepancies of the values of the SWM parameters found considering the outer process and the results found in the literature using different experimental techniques and calculations, we reanalyzed the same data of Fig. 6.2(c) but now considering the inner process. We also have used two distinct non-linear phonon dispersions for the symmetric and the anti-symmetric phonon branches, since the best fit was obtained when we consider different dispersions for the two iTO phonon branches of bilayer graphene.

Fig. 6.5 shows the experimental data (dots) and the tight-binding fitting results (curves) comparing both the outer and the inner processes. Fig. 6.5(a)*outer* shows the fit considering the outer process for the DRR scattering. The values obtained for γ_0, γ_1, γ_3, γ_4, Δ, and t' are shown in Table 6.2(a). Note that, in Fig. 6.5, the fittings considering the two different DRR scattering processes produce rather different results. In the inner process case, we cannot fit the data with the same parameters that produce the best fit for the outer process shown in Fig. 6.5(a)*outer*. This is shown in Fig. 6.5(a)*inner*, where the theoretical curve (obtained using the values of γ_1 and γ_3 from Table 6.2(a)) differs considerably from the experimental values. The best fit for the inner process is shown in

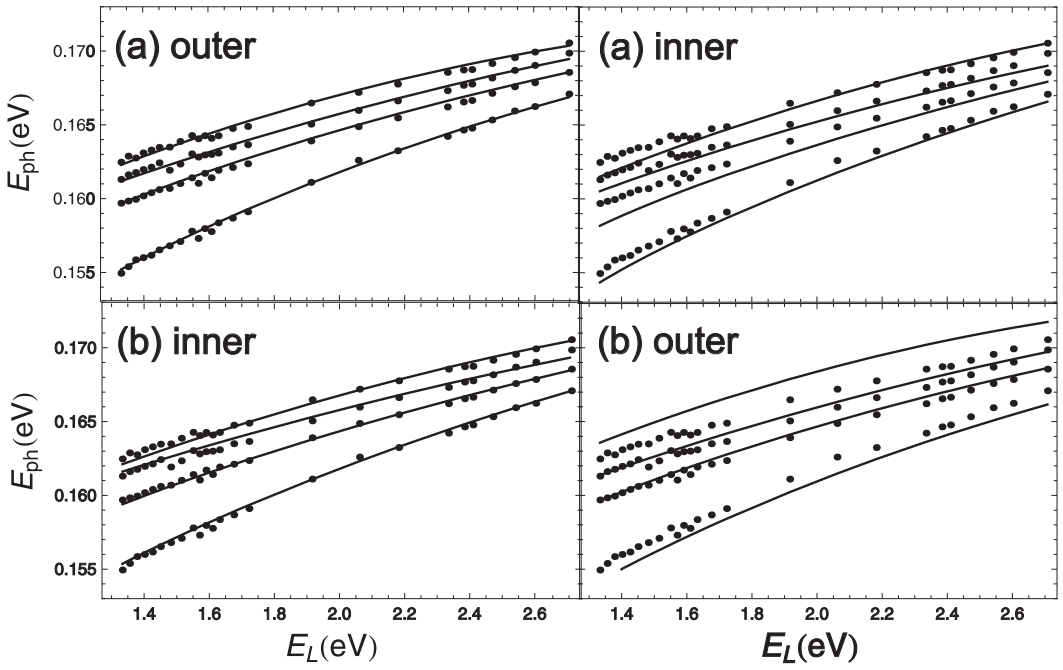

Figure 6.5: Laser energy dependence of the G′ band peaks, with four different fittings, considering: ((a) outer) The outer scattering process with the best SWM parameters for this case, in Table 6.2(a); ((a) inner) The inner process fitted using the best SWM parameters for the outer process (Table 6.2(a)). ((b) inner) The inner scattering process with the best SWM parameters for this case, shown in Table 6.2(b). ((b) outer) The outer process fitted using the best SWM parameters for the inner process (Table 6.2(b)).

Table 6.2: Best values of the SWM parameters (in units of eV) obtained for (a) the outer and (b) the inner scattering processes.

	γ_0	γ_1	γ_3	γ_4	Δ	t'
(a)	3.0	0.35	0.10	0.10	0.01	0.15
(b)	3.0	0.40	0.30	0.10	0.01	0.15

Fig. 6.5(b)*inner* and gives values of $\gamma_1 = 0.40\,\text{eV}$ and $\gamma_3 = 0.30\,\text{eV}$, the same values found in the literature by other techniques, and with the same values of γ_0, γ_4, Δ and t′ of the outer process. In a similar manner, the outer process cannot be fitted using the best fit parameters for the inner process case: deviations from the experimental results are again observed, as shown in Fig. 6.5(b)*outer*.

The above discussion shows that the inner DRR process gives tight-biding parameters in better agreement with those obtained by other experimental techniques. In principle, there is a large number of phonon wavevectors that satisfy the DRR process, connect-

Table 6.3: Best values of the iTO phonon dispersion parameters ($w(q) = A + Bq + Cq^2$) obtained for (a) the outer and (b) the inner scattering processes.

	symmetric			anti-symmetric		
	A (meV)	B (meVÅ)	C (meVÅ^2)	A (meV)	B (meVÅ)	C (meVÅ^2)
(a)	146.3	86.9	-70.3	150.5	66.3	-44.8
(b)	150.1	-65.9	-46.9	152.0	-54.4	-34.0

ing electronic states in equienergy contours around the K and K' points. The calculation of the DRR profile must take into account all these possible DRR phonon wavevectors, by doing the full two-dimensional integration with the correct **q** wavevector dependence of the associated electron-phonon matrix elements. Some interference effects also appear when the Raman expression is squared out in order to calculate the Raman intensity [73]. Until this work was done, to our knowledge, there was only one full calculation of the shape of the DRR bands that takes into account the **q** wavevector dependence of the electron-phonon matrix elements, and this calculation predicts an asymmetric shape for the G$'$ band in monolayer graphene [73]. However, the experimental G$'$ band obtained with visible photons are nicely fitted by a single Lorentzian line. This shows that some ingredients were missing in order to fully explain the DRR process in graphene systems. Later, a more precise calculation was performed by Venezuela *et al.* [98] in which the intensity and line shape of defect-induced and two-phonon bands were well described quantitatively. In that work [98], contrary to the previous findings in literature that the phonons which mostly contribute to the G$'$ band are outer phonons, Venezuela *et al.* showed that, in fact, the inner phonons are the most important for the G$'$ band in graphene, in accordance with our work. This finding stems from the complex behavior of the scattering matrix elements in graphene.

The results obtained in this work could be the starting point to investigate other systems which constitute a hot subject in graphene physics, such as the inner DRR process in strained or twisted bilayer graphene. In the former case, bilayer graphene is grown on an insulating material (such as SiO_2), which imposes a strain on the graphene system. This setup has been considered as a building block for microelectronics [99–101]. In the latter case, the stacking of the two layers is different from the usual AB (Bernal) stacking. In both cases, there is a significant modification in the electronic and optical properties of the systems, which directly influences the double resonance Raman bands. This produces

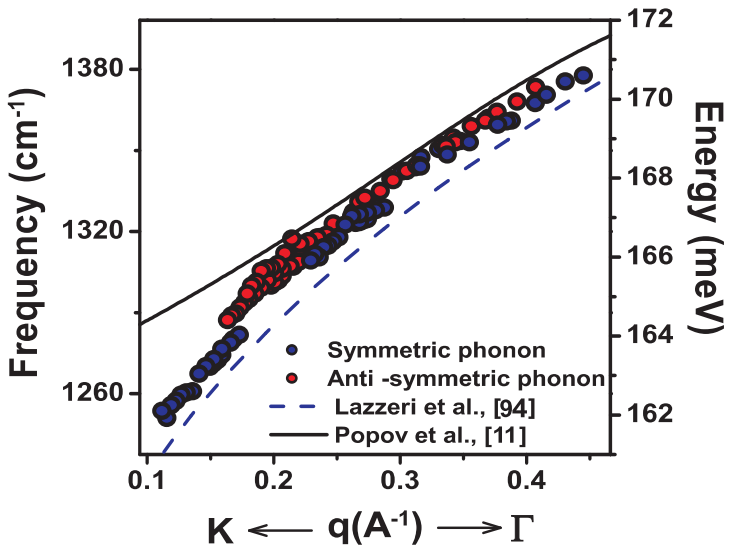

Figure 6.6: Phonon dispersion relation of bilayer graphene near the K point of the symmetric (blue points) and the anti-symmetric (red points) phonon branches obtained from the double resonance Raman spectroscopy. The black and blue solid curves correspond respectively to the phonon dispersion near the Dirac point of the iTO phonon branch of monolayer graphene calculated using tight-binding by Popov *et al.* [27] and using DFT by Lazzeri *et al.* [102] within the GW approximation.

different G′ peaks that can be theoretically studied by looking at the P_{ij} processes.

Another interesting result that we can obtain from this work is about the distinct dispersions of the symmetric and anti-symmetric phonon branches. Table 6.3(b) shows the parameters obtained for the S and AS phonon branches. Note that the S phonon branch is more sensitive to the change of scattering process than the AS mode, *i.e.*, when going from the outer process to the inner process. We observe that the quadratic coefficients C assume negative values, showing that the slope of the phonon dispersion increases with decreasing $\mathbf{q}$ values. This is direct evidence of the Kohn anomaly for the iTO phonon branches, which are expected to drop discontinuously at the K point.

The experimental data shown in Fig. 6.5 can be directly plotted in a phonon energy dispersion relation (ω_{ph} versus $\mathbf{q}$ plot) [17]. Fig. 6.6 shows the phonon dispersion of the symmetric (blue points) and the anti-symmetric (red points) phonon branches obtained from the DRR results. Fig. 6.6 also shows the phonon dispersion near the Dirac point of the iTO phonon branch of monolayer graphene calculated using the tight-binding approximation by Popov *et al.* [27] (black solid curve) and using DFT by Lazzeri *et al.* [102] (blue solid curve) within the GW approximation, where electron-electron interactions are taken into account more precisely. It is interesting to see that the theoretical phonon dispersion

calculated by tight-binding is in better agreement with the experimental data for higher phonon energies. However, this model fails to describe the data for lower phonon energies, which are in good agreement with the calculations within the GW approximation. This result shows the importance of considering electron-electron interactions in order to correctly describe the Kohn anomaly near the K point of graphene.

Another interesting observation is that the Kohn anomaly is stronger for the S phonon branch, as shown in Fig. 6.6. This result is in agreement with the calculation performed by T. Ando [33], which predicts a stronger phonon renormalization for the symmetric phonons, due to distinct selection rules for interaction of S and AS phonons with intra-valley and inter-valley electron-hole pairs.

6.3 Summary

In summary, the dispersion of electrons and phonons of bilayer graphene was investigated by performing a resonance Raman study of the the G′ Raman band, using laser energies from the visible to the near-IR range. The electronic structure was analyzed within the tight-binding approximation and within the Slonczewski-Weiss-McClure (SWM) parametrization [22,23] considering both the outer and the inner double resonance Raman (DRR) process. Considering the outer process, our values for γ_1 and γ_3 are lower than the values obtained by other experimental techniques and calculations in the literature. On the other hand, when considering the inner process, the values for all the SWM parameters are the same of those found in the literature, strongly suggesting that the main contribution for the G′ band comes from the inner DRR process. Also, we have measured the phonon dispersion of the iTO branches near the it K point, and it was observed two distinct dispersions for the iTO phonon branches. The softening of the phonons reveals the K point Kohn anomaly in bilayer graphene, and also shows that the phonon renormalization is stronger for the symmetric phonon branch. Our results agree with the phonon dispersion calculation [102] that takes into account electron-electron interaction in graphene systems, which plays a major role to correctly describe the Kohn anomaly near the K point. The work about the outer process was published in *Physical Review B (Rapid Communications)* **80**, 241414 (2009), and the study of the inner process was published in *Carbon* **49**, 1511 (2011).

Chapter 7

Using the G′ Raman Cross-Section To Understand the Phonon Dynamics in Bilayer Graphene Systems

Graphene systems are known to be excellent electrical conductors with mean free paths at room temperature usually larger than one micron [3,9,103]. They have therefore attracted strong interest for possible applications in nanoscale electronics [104,105]. Graphene is also a great thermal conductor and its thermal conductivity has been reported to reach around 2,000 $\mathrm{W\,m^{-1}K^{-1}}$ at room temperature [106–108]. It is thus important to consider temperature T dependent effects because the high performance of graphene can be compromised due to T-dependent changes in its properties. Some relevant works [108,109] have been done on monolayer graphene (1LG) and bilayer graphene (2LG) regarding T-dependent effects. In those works [108,109], Raman spectroscopy was used to study the temperature dependence of the frequency ω_G and line width γ_G of the optical E_{2g} phonons at the Γ point of the Brillouin zone (BZ), known as the G band. The A_1' mode at the K point (known as the G′ or 2D band) was also studied to give information about the thermal properties of these systems [108,109]. In particular, Yoon *et al.* [109] showed that the thermal expansion coefficient of 1GL strongly depends on T and is negative at least in the temperature range of their measurements ($200<\mathrm{T}<400\,\mathrm{K}$).

Also, it has been shown that the relative Raman cross-sections σ of the four G′ peaks depend on the laser excitation energy E_L [92]. The four peaks are related to different electron $\mathbf{k}$ and phonon $\mathbf{q}$ wavevectors. Since the electron-phonon interaction matrix elements depend on the electron wavevector, we expect that the $\mathbf{k}$ dependence of

the matrix element can be examined by experiment through the combination of power, temperature and laser wavelength dependencies, which is the motivation of the present work. The σ is obtained through the integrated area (IA) under the Raman peak and should not depend on its broadening. The difference of the σ between the four G′ peaks [41] is responsible for the special lineshape of the G′ band of AB stacked 2LG, which is usually used to identify the 2LG regions within typical samples by Raman spectroscopy (see Sectio, 3.3) [41]. Thus, it is very important to understand all the processes that give rise to the G′ band as well as their dependence on temperature T and laser energy E_L. In this chapter, we use Raman spectroscopy to study both the E_L-dependent and the T-dependent effects in AB Bernal stacked 2LG and we use the relative IA of the four peaks of the G′ band to understand the electron inelastic scattering processes in bilayer systems. In particular, we show that the dependence of the IA of the four peaks on both E_L and laser power gives us important information about the electron-phonon (el-ph) interaction and the relaxation time τ of the photo-excited electrons.

7.1 Thermalization effects by emission of low-energy phonons in carbon-systems

It is known that, in graphite, the dynamics of photo-excited carriers are dominated by both electron-electron (el-el) and electron-phonon (el-ph) scattering. After optical excitation, the electrons are thermalized by el-ph scattering, in such a way that the electron and hole distributions relax to their respective band extrema and this relaxation process takes about 1 ps [110,111]. These electron relaxation processes cause a significant reduction of the ballistic conductance of graphene and carbon nanotubes at bias potentials larger than ~ 0.2 V, severely limiting interconnect performance [19,112]. A microscopic characterization of phonon decays is thus a key step in improving the understanding of the properties of these materials, whereas engineering individual decay channels would allow to control energy relaxation and ultimately performance.

In 2004, Jiang *et al.* [63] performed the el-ph interaction calculations in graphite using up to 4^{th} nearest-neighbor sites within the tight-binding framework. Also, they [63] calculated the relaxation time of photo-excited electrons over a wide energy region. Fig. 7.1 shows the results found by Jiang *et al.* [63], the emission and absorption relaxation times of a photo-excited electron (τ_e and τ_a) as a function of energy. For an electron to absorb a phonon, there should exist a phonon in the solid. However, an electron can emit a phonon even though there is no phonon in the solid. Therefore, generally the phonon

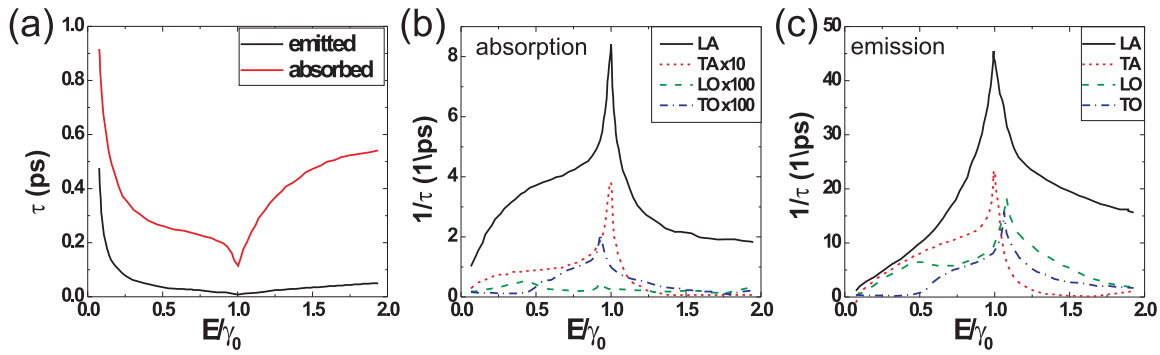

Figure 7.1: (a) Electron relaxation time dependence on the initial electron state energy. Black and red lines are for phonon emission τ_e and absorption τ_a, respectively. Inverse of the relaxation time for each phonon branch for (b) phonon absorption and (c) phonon emission. In (b) the values for the optical branches have been amplified by a factor of 100 and the values for the tangential acoustic branches have been amplified by a factor of 10. The results are for $\gamma_0 = 2,9\,\text{eV}$ and $T = 300\,\text{K}$. Figure adapted from Ref. [63].

emission process has more phonons and the electron relaxes faster by phonon emission than by phonon absorption, as can be seen in Fig 7.1(a). The el-ph relaxation time is determined by the el-ph coupling strength, and by the electron and phonon dispersion relations. The dip in Fig. 7.1(a) reflects the van Hove singularity of the electron density of states at the M points in the Brillouin zone. Figs. 7.1(b) and (c) give the inverse of the relaxation time for each of the phonon branches considered in the work of Ref. [63], where we can see that the main responsible for the electron relaxation process is the emission of acoustic phonons, due to its small energy when compared to the optical phonons.

The photo-excited electron relaxation mechanism was studied experimentally in graphite and in carbon nanotubes [113,114] using time-resolved and photoluminescence experiments. But this kind of electron-phonon interaction was not reported in graphene systems until now. What we will show in this work is that, due to the special electronic structure of bilayer graphene, we can use the Raman spectroscopy to study electron relaxation processes, through the dependence of the Raman cross-section of the G′ feature on laser energy and temperature.

7.2 Photo-excited electron relaxation in bilayer graphene

In this section we explain how to obtain information of the phonon dynamics in bilayer graphene using Raman spectroscopy. The Raman measurements were taken in

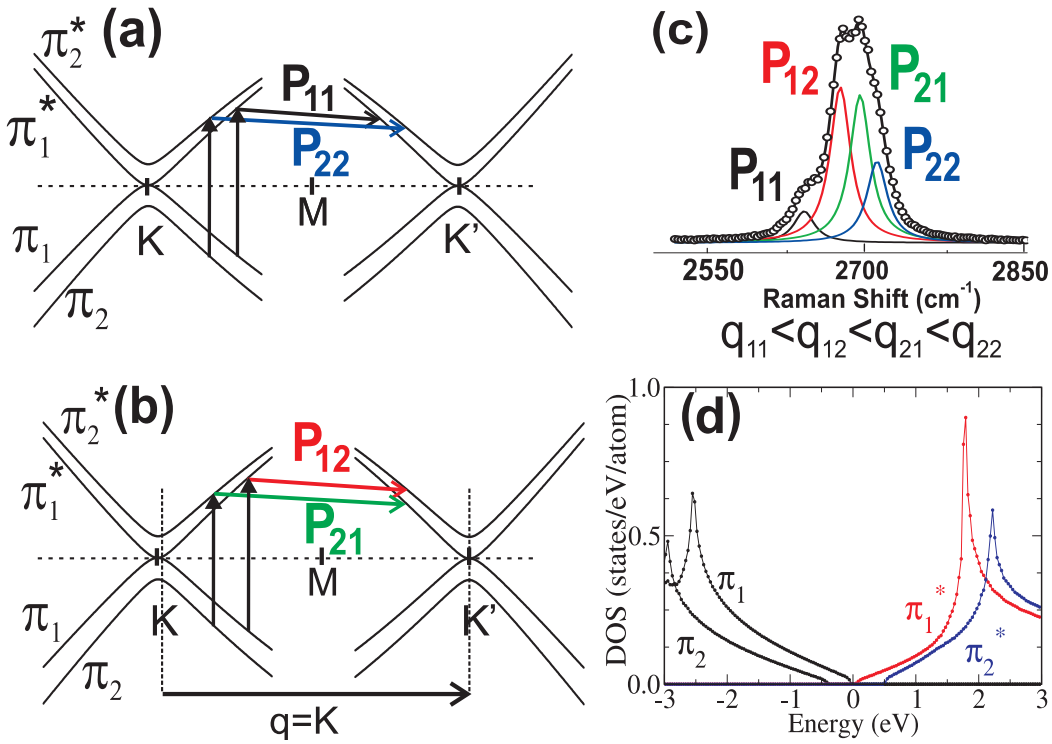

Figure 7.2: (a) and (b) Double resonance Raman processes which give rise to the four peaks in the G′ band in AB stacked bilayer graphene. (c) The G′ band measured with the 532 nm laser line and the four peaks corresponding to each process: P_{11} (black line), P_{12} (red line), P_{21} (green line) and P_{22} (blue line), with the relative magnitude of the phonon wavevectors **q** shown. (d) Density of electronic states of 2LG for the valence bands π_1 and π_2 (black curves) and for the conduction bands $\pi_1^\star$ (red curve) and $\pi_2^\star$ (blue curve).

the back scattering configuration using four different laser excitation energies: 2.18 eV (570 nm) dye laser, 2.33 eV (532 nm) Nd:YAG laser, 2.41 eV and 2.54 eV (514 and 488 nm, respectively) Ar laser. For each E_L, we changed the laser power over the 0.5 to 12 mW range. The sample only was exposed to the laser beam, whose spot size was $\sim$1 μm with a 100 $\times$ objective, during the acquisition time (2 seconds) in order to avoid damage to the graphene flake. In this laser power range, no D band was observed in the Raman spectra, indicating that no defects were introduced by the laser light exposure. All the Raman features presented in the measured spectra were fitted with four Lorentzian curves.

The process which gives rise to the G′ band in graphene is an intervalley double resonance Raman (DRR) process involving two phonons from the in-plane transverse optical (iTO, $q \approx 2k$) phonon branches [39,74]. In the case of 2LG with the Bernal AB layer stacking, the electronic structure close to the K point has two valence bands (π_1 and π_2) and two conduction bands ($\pi_1^\star$ and $\pi_2^\star$). In a general DRR P_{ij} process for 2LG

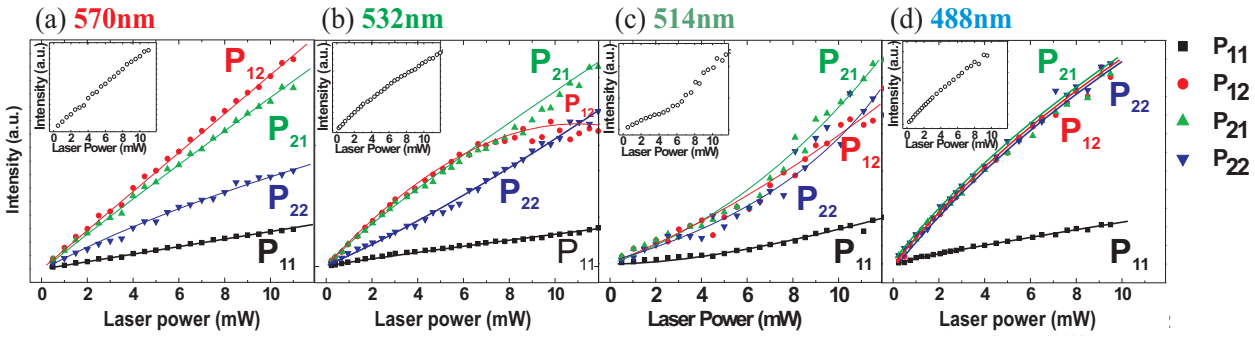

Figure 7.3: The measured Raman integrated area IA of the four peaks that compose the G′ band of bilayer graphene as a function of the laser power for the (a) 570 nm, (b) 532 nm (c) 514 nm and (d) 488 nm incident laser lines. The black squares correspond to the P_{11} processes, the red dots to the P_{12}, the green up and blue down triangles to the P_{21} and P_{22}, respectively. The open circles in the insets correspond to the total IA of the G′ band. The solid lines are guide for the eyes.

(Figs. 7.2(a) and (b)), one electron is resonantly and vertically excited from the valence band π_i ($i = 1, 2$) to the conduction band $\pi_i^\star$ by absorbing a photon with energy E_L. The electron is then resonantly scattered by a phonon with wavevector $\mathbf{q}$ to the $\pi_j^\star$ (j=1,2) band of an inequivalent K' point of the BZ. Finally, the electron is scattered back by another phonon and recombines with the hole, thereby emitting a photon. As we have shown in Chapter 6, the main contribution to the G′ peak occurs when the electron is scattered from the inside of the electronic dispersion ($\mathbf{q} < \mathbf{K}$) [75,94,95,98], as we show in Fig. 7.2. Since there are two possible electronic transitions (π_i to $\pi_i^\star$ for $i = 1, 2$), there are four possible electron scattering processes, and they are illustrated in Figs. 7.2(a) and (b). The iTO phonons from the symmetric (S) phonon branch are involved in the processes P_{11} and P_{22} (Fig. 7.2(a)), while the anti-symmetric (AS) ones are involved in the P_{12} and P_{21} processes (Fig. 7.2(b)). [28] Since the electronic states are shifted from each other because of an interlayer interaction energy [89], the wavevectors of the phonons that satisfy the DRR condition are different, and consequently, the phonons have a small energy difference from one another. In the case of the G′ band, the larger the q wavevector, the higher is its phonon energy. Thus, considering q_{ij} as the wavevector of the phonon involved in the process P_{ij}, we find that $q_{11} < q_{12} < q_{21} < q_{22}$. Then, the G′ band of 2LG is composed of four peaks, as we can see in Fig. 7.2(c), where we show the fitting based on four Lorentzians and their corresponding scattering processes.

The power dependence of the IA of the four peaks of the G′ band for the 570 nm,

532 nm, 514 nm and 488 nm laser excitation lines is shown in Figs. 7.3 (a), (b), (c) and (d), respectively. For clarity, the colors and the symbols in the legends of Figs. 7.2 and 7.3 were kept the same for each process. The black squares in Fig. 7.3 correspond to the P_{11} process, the red dots to P_{12}, the green up and blue down triangles to P_{21} and P_{22}, respectively. The open dots in the insets correspond to the total IA of the G′ band. Disregarding the electron-phonon relaxations, the IA in a Raman process is proportional to its Raman cross-section and the cross-section is proportional to $H_{ii} \times Q_{ij}$, where the matrix element H_{ii} gives the electron-photon interaction that is basically associated to the electronic density of states (DOS), while the matrix element Q_{ij} gives the electron-phonon interaction. In other words, the electron which makes a transition between the electronic bands $\pi_i - \pi_i^\star$ for i=1,2, is scattered by a phonon, which subsequently connects that electron to electronic states $\pi_i^\star$ to $\pi_j^\star$ for i,j=1,2. From Fig 7.2(d), we can see that $H_{11} > H_{22}$, *i.e.*, the DOS for the $\pi_1^\star$ band is larger than that for the $\pi_2^\star$ band. Also, it is known that the matrix elements Q_{ij} are larger for the anti-symmetric phonons than for the symmetric ones [63,115]. Then, in a first approximation, the Raman cross-sections σ_{ij} is expected to obey $\sigma_{22} < \sigma_{11} < \sigma_{21} < \sigma_{12}$, leading to the corresponding IA of the peaks $P_{22} < P_{11} < P_{21} < P_{12}$. However, this is not the dependence found in Fig. 7.3. Moreover, Fig. 7.3 shows two behaviors: one which is E_L-dependent (here we are considering qualitative behavior) and another which is T-dependent, as we explain below.

Regarding the E_L dependence of the IA, one can see in Fig. 7.3 that the P_{11} peak is weaker in intensity than the other peaks, including the P_{22} peak. Also, the P_{11} IA does not change appreciably for the different E_L values, which is consistent with the P_{11} process being determined by a single relaxation time. On the other hand, we clearly see that the IA of the other three processes are changing for each E_L and they are becoming very close to each other as the incident E_L increases. This is an important point that was never addressed before and we can relate this behavior to the el-ph coupling mechanism and to the phonon relaxation times.

First, one must pay attention to whether an increase in the laser power P_L is increasing the temperature and changing the force constants of the material or if the increasing laser power is just increasing the phonon population in the system. The change of the phonon frequency with temperature is a manifestation of the anharmonic terms in the lattice potential energy, which is determined by the anharmonic potential constants, the phonon occupation number, the phonon-phonon interactions and the thermal expansion of the crystal [112]. Figs. 7.4(a) and (b) show, respectively, the frequency ω_G and the width decay γ_G of the Raman G band as a function of the laser power P_L for the 488 nm (blue

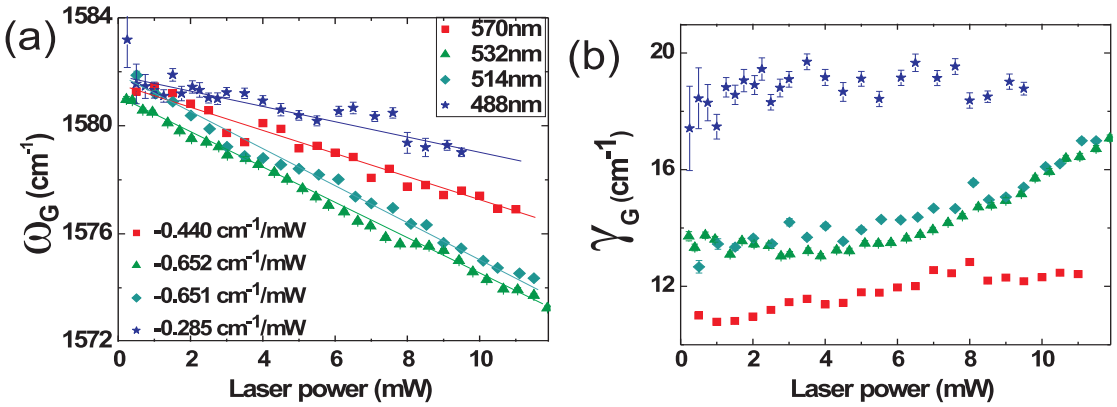

Figure 7.4: (a) The frequency ω_G with the respective slope for each laser line and (b) the decay width Γ_G of the G band of bilayer graphene as a function of the laser power for the 488 nm (blue stars), 514 nm (dark cyan diamonds), 532 nm (green triangles) and 570 nm (red squares) laser lines.

stars), 514 nm (dark cyan diamonds), 532 nm (green triangles) and 570 nm (red squares) laser lines. For all E_L, it is possible to observe a softening of the ω_G and a small broadening of the γ_G as a function of the P_L. According to Bonini *et al.* [112], these results clearly show that the temperature of our bilayer system is increasing with increasing P_L and we are seeing the combined result of the thermal expansion of the crystal and also of the phonon-phonon scattering [112]. Based on the literature [108,116], for experiments using samples prepared under similar conditions as the samples used in this work, a downshift of -0.0154 cm^{-1}/^{o}C is expected for the G band of bilayer graphene. From Fig. 7.4(a), one can see a $\sim$ 7 cm^{-1} downshift of the G band for the 514 nm and 532 nm laser lines, which corresponds to an increase of $\sim$ 455 ^{o}C in temperature. For the 570 nm laser line, we find a redshift of $\sim$ 6 cm^{-1}, corresponding to a increasing in the temperature of $\sim$ 390 ^{o}C, while for the 488 nm laser line, we find a redshift of $\sim$ 5 cm^{-1} indicating a increasing in the temperature of $\sim$ 325 ^{o}C. It is important to comment that the variation of the temperatures with E_L is an expected occurrence since the thermal response of both bilayer graphene and also the SiO_2 will be somewhat different for different E_L [117].

The G$'$ band comes from the scattering of an electron by two iTO phonons from one K point to another inequivalent K' point in the BZ [39,74]. It is worth noting that all the analysis made for the electron scattering and relaxation in the conduction band can be analyzed in an similar way for the scattering of a hole in the valence band. In the time between when the electron is photo-excited and the electron is scattered by the first iTO phonon (an intervalley EV$_{ij}$ process) [63,118], the electron can first relax from $\pi_2^\star$ to $\pi_1^\star$

(or from $\pi_1^\star$ to $\pi_2^\star$) by the emission or absorption of a phonon [63,118] and this relaxation can also involve intravalley AV or intervalley EV processes (see Fig. 7.5(a)). In the range of the laser excitation energies used in this work (2.18-2.54 eV), the electron relaxation time is faster by the emission of a phonon (around 20 fs) than by the absorption of a phonon (around 200 fs), as can be seen in Fig 7.1 [63,118]. Moreover, the electrons relax from 2 to 3 times faster by an emission of an acoustic phonon than by an optical phonon emission [63,118]. Thus, the main channel of relaxation for the excited electrons is by the emission of a low-energy acoustic phonon. From the Fermi golden rule, it is known that the transition rate is proportional to the density of states (DOS). We can see from Fig. 7.2(d) that the electronic DOS of $\pi_1^\star$ (red curve) is larger than the DOS of $\pi_2^\star$ (blue curve) in the range of E_L used in this experiment. In this framework, it is important to note that both intra-band ($\pi_i^\star$ to $\pi_i^\star$ for i=1,2) and inter-band ($\pi_1^\star$ to $\pi_2^\star$ and $\pi_2^\star$ to $\pi_1^\star$) relaxations are allowed to occur. In particular, because $\pi_1^\star$ has a higher DOS in comparison to $\pi_2^\star$, then $\pi_1^\star$ loses more population than $\pi_2^\star$ during the relaxation process. To illustrate what this means, consider that $\pi_1^\star$ has 100 electrons and $\pi_2^\star$ has 50 electrons. Next, by relaxation mechanisms, consider that both the $\pi_1^\star$ and $\pi_2^\star$ will give 10% of their population to one another. In the end, $\pi_1^\star$ will have 95 electrons while $\pi_2^\star$ will have 55, which means that $\pi_1^\star$ lost more electrons (10) than $\pi_2^\star$ lost (5). Since a low decay rate from $\pi_2^\star$ to $\pi_1^\star$ is expected, the red arrows in Fig. 7.5 denote the net transition from $\pi_1^\star$ to $\pi_2^\star$. After being scattered by the first iTO phonon, the electron can relax by emitting a phonon at the K' point in a similar way. When these decays happen, the rate of the scattering that gives rise to the G$'$ band for some processes decreases in IA and contributes to the IA of another process at the same time. For example, in the process P_{11} the electron can decay from the $\pi_1^\star$ to the $\pi_2^\star$ state at the K point before the scattering by the iTO phonon (see Figs. 7.5(b) and (f)). In this case, this decay contributes to the increase of the P_{21} and P_{22} processes, while the IA of the P_{11} peak decreases. A similar analysis can be made after the electron is scattered to the K' point by the first iTO K point phonon. At the K' point, the electron decays from the $\pi_1^\star$ to the $\pi_2^\star$ band, in which the IA of the P_{11} peak decreases again and the IA of the P_{12} and P_{22} peaks increases. A decay effect also occurs for the other three processes, P_{12}, P_{21} and P_{22}, and these processes are illustrated in Figs. 7.5(c), (d), and (e), respectively. In the figures, the solid lines represent the original scattering of the iTO phonon process and the dashed lines represent the new possible scattering processes for the electron that can occur after the decay. When the electron at $\pi_1^\star$ is relaxed to $\pi_2^\star$, the hole at π_1 is required to be relaxed to π_2 so as to recombine with the electron. Because of all the decays and competitions between one process and another, there is a

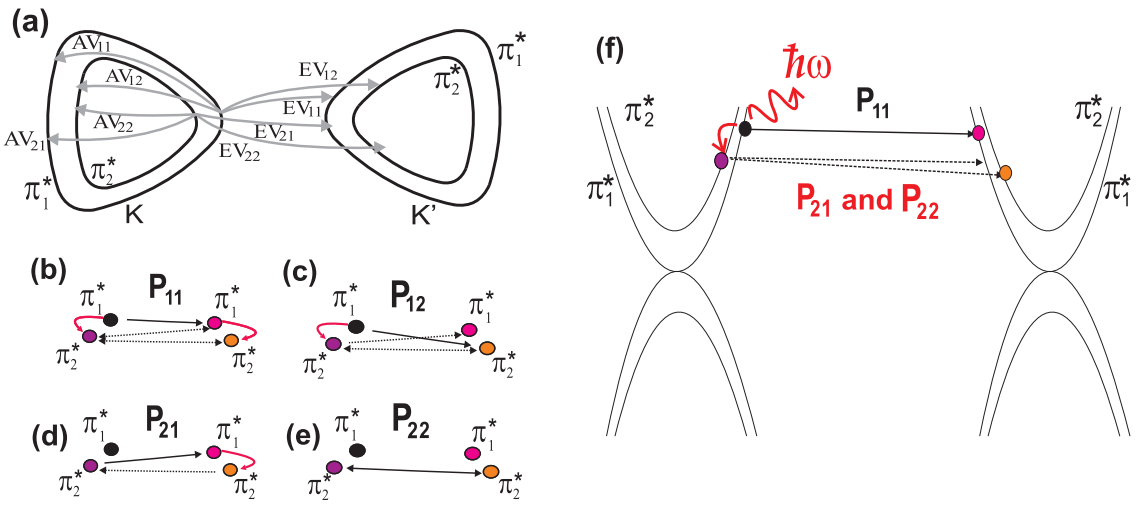

Figure 7.5: (a) All the possible electron relaxation processes by the emission of a phonon (the same processes can also occur by the absorption of a phonon). The decay can be by an intravalley (AV) or intervalley (EV) process (see text). The possible electron decay (red arrows) for processes (b) P_{11}, (c) P_{12}, (d) P_{21} and (e) P_{22}. The solid lines represent the original scattering events for that process and the dashed lines represent the new possible scattering processes for the electron after the decay. In this sense, from the most to the less favored process by the electron decay we have $P_{22} > P_{21} \sim P_{12} > P_{11}$. (f) Schematic view of the P_{11} process relaxation into the P_{21} and P_{22} processes.

large difference in the IA of the four G′ components P_{ij}.

In the E_L range used in this work, Jiang *et al.* [63] showed that the electron relaxation time in graphite by phonon emission becomes shorter when the energy is increased (~ 10 fs faster for 2.54 eV than for 2.18 eV). This happens because the density of the final states for a given initial state after phonon emission is higher in graphite for higher energy (or momentum) phonons. Then, we expect that this situation should be the same for the case of 2LG. In this latter case, for higher E_L, the relaxation rate increases, consequently increasing the contribution of all the processes to the P_{22} process. This is the reason why the IA of the P_{22} process gets closer to the IA of P_{12} and P_{21} for higher E_L. According to Jiang *et al.* [63], this effect is a maximum when the energy of the electronic state is equal to the hopping energy ($\gamma_0 \approx 2.9$ eV) between the nearest neighbor carbon atoms. For energies higher than 3 eV, the relaxation time increases and we expect the IA of the P_{22} process to again become smaller than that for the P_{12} and P_{21} processes. As seen in the insets of Figs. 7.3(a)-(d), the total IA monotonically increases for each E_L. This means that the increase or decrease of the four peaks is a continuous process and comes from the relaxation within the P_{ij} transitions. For 448 nm laser excitation, the mutual relaxation

for P_{12}, P_{21} and P_{22} is sufficiently fast so that the populations of the photo-excited carriers rapidly reach thermal equilibrium. The reason why the P_{11} is relatively small is that the probability of the relaxation process to $\pi_1^\star$ is small and there is almost no flow into the P_{11} process from the other processes.

Another interesting point to be noted is regarding the T dependence, where one can see an anomalous behavior of the IA of the four peaks of the G′ band for the 532 nm laser line. From Fig. 7.3(b), there is a saturation of the process P_{12} and a slight increase in the slope of the P_{21} and P_{22} processes as the laser power increases. Different laser lines excite the electron to a different point of the conduction band. In the case of bilayer graphene, the conduction $\pi_1^\star$ band gets close to the $\pi_2^\star$ band for higher energies due to γ_3 and γ_4 interlayer interactions [18,22,23,44].

Thus this extra resonance mechanism depends on laser energy. For the 532 nm laser line, the energy difference likely matches the energy of the ZO′ phonon (breathing mode between the two layers) whose energy is about 10 meV. [119] In this resonance regime, the rate of emission of phonons by the relaxation of the electrons from the $\pi_1^\star$ to the $\pi_2^\star$ band becomes very high. For a laser with longer (smaller) wavelength, the difference in energy between the $\pi_1^\star$ and $\pi_2^\star$ bands is higher (lower) than the energy of the ZO′ phonon. The additional relaxation path by the ZO′ phonon might suppress the saturation of the absorption which is the reason why the total Raman IA for the 514nm line (inset of Fig. 7.3(c)) is acceleratingly increased with increasing laser power. For the other cases of Fig. 7.3, however, the total Raman IA monotonically increases with a slightly saturating behavior. In the case of Fig. 7.5(c), the P_{12} process decreases followed by a larger contribution to the P_{21} and P_{22} processes. It is also worth mentioning that this resonance condition also depends on the laser power. For lower laser power, this resonance is not observed. Since there is no saturation in the optical absorption, the relative differences between P_{12} and P_{21} with increasing power are mostly due to phonon-phonon processes that become more important with increasing temperature. Since the contribution of the process P_{11} to the other processes is already large, even out of the resonance regime, we cannot see any appreciable change in the IA of the P_{11} peak with increasing laser power. For the 514 nm laser line, this saturation of the P_{12} process persists, but this saturation is weaker than that for the 532 nm laser line, indicating that the relaxation process is getting out of resonance. This is a very important result for the applications of bilayer graphene in nano devices, since most electronic systems show an increase in T when in use. Especially for photocurrent measurements, it has been shown that the maximum enhancement coefficient of the electric field was found to occur for

incident light around the green region [120,121], in agreement with our result.

7.3 Summary

In summary, we made a detailed analysis of the integrated area (IA) under the four peaks (P_{11}, P_{12}, P_{21} and P_{22}) that compose the G′ Raman band of bilayer graphene under various laser excitation conditions. We show that their IA depends on the temperature and on the excitation laser energy. Due to the strong electron-phonon coupling and the fast electron thermalization, some processes experience a decrease in their scattering rate due to electron relaxation through the conduction band by low-energy phonon emission. This decreased scattering rate contributes to the increase of the rate of another P_{ij} scattering process. Our analysis of the experiment is in agreement with theoretical calculations about the phonon decay process, which predicts that the A_1' mode at the K point (the mode with the strongest el-ph coupling in graphene and the one that will be overpopulated by the optical phonons) has a large decay channel toward the low-energy acoustic phonon modes [112]. Also, due to a resonance condition which increases the electron relaxation rate, we found an anomalous behavior for the IA of the G′ peaks around the green 532 nm laser line that can be observed by increasing the temperature. This is an important characteristic of the electron scattering in bilayer graphene and should be taken into account in future electronics applications of this material. This work is published in *Nano Letters* **12**, 2883 (2012).

Chapter 8

Conclusions

In this thesis we study the origin and the consequences of the electron-phonon coupling in graphene systems. With the Raman spectroscopy together with gate dependent measurements in graphene devices we are able to get information on the electron-phonon interaction and how tuning the Fermi level position affects this coupling. In Chapters 2 and 3 we make an overview of the electronic and vibrational structure of monolayer graphene, as well as the theory behind the Raman scattering and the double resonance Raman process. Predictions of some expected electron-phonon effects such as the Kohn anomaly are also described in Chapter 2. A detailed explanation of the fabrication of graphene devices for both back gate and top gate measurements is discussed in the Chapter 4 and the samples produced by the techniques described there are used for the experiments in the following chapters.

The electron-phonon (el-ph) interaction is very strong in graphene, and some special phonons, specially those responsible for the main Raman features, can create an electron-hole pair. This process renormalizes the phonon energy giving rise to the Kohn anomaly. The Kohn anomaly was very well studied theoretically and experimentally for the zone-center (Γ point) $q = 0$ phonon branch, which can be appreciated by observing the G band Raman feature evolution in graphene as the Fermi level energy (E_F) is varied [19,32,52]. In the case of the zone-center $q = 0$ phonon, the renormalization is suppressed when the Fermi level position is changed by an amount larger than half of the phonon energy due to the Pauli exclusion principle, and a hardening of the phonon frequency followed by a line width narrowing is observed. In this thesis we study the phonon renormalization in monolayer graphene for the $q \neq 0$ phonons around the Γ point (intravalley processes) and around the K point (intervalley processes) of the Brillouin zone. For the $q \approx 2k$ phonons we observe a softening of the phonon frequency and a broadening of the decay

width, the opposite behavior observed for the $q = 0$ phonons. For the $q = 0$ (measured from the K point) intervalley phonon, the phonon renormalization was negligible. A phenomenological model based on the density of states of electron and phonons was given to explain the behavior of the $q \neq 0$ phonon renormalization.

These new results launch gate-modulated Raman as a new approach to identify and assign phonon modes in solid state materials. We then applied gate-modulated Raman, together with laser-dependent Raman measurements to study the G* band ($\sim 2450\,\mathrm{cm}^{-1}$) and five combination modes in the spectral range of $1700 - 2300\,\mathrm{cm}^{-1}$ in monolayer graphene. We showed that the G* mode is an asymmetric peak composed by two peaks, the iTO+LA combination mode, which is an intervalley $q \approx 2k$ process with a strong phonon renormalization, and the 2iTO overtone mode, which is an intervalley $q = 0$ (measured from the K point) process with a weak phonon renormalization. For the five combination modes, we have assigned the first three peaks, respectively, to the intravalley combination modes LO+iTA, iTO+LA and LO+LA around the Γ point of the Brillouin zone and peaks 4 and 5 to the intervalley oTO+iTO ($K\Gamma$ direction) and iTO+iTA (KM direction) combination modes around the K point of the Brillouin zone, respectively. The el-ph dependencies of the peaks frequency and decay width on gate voltage support our assignments when compared to the assignments in the current literature [17,67,68,71]. We believe that this technique will certainly contribute to the understanding of more complex structures such as few-layer graphene, their stacking order relations as well as how these stacking orders influence the many-body interactions in the system. Moreover, the techniques reported here can become a key strategy to learn and understand a whole class of new layered 2D-materials, such as molybdenum sulfide (MoS_2), hydroxides and oxides in general, now emerging in the scientific community.

For bilayer graphene, we shown the mixing of the optical phonon modes due to the asymmetry between the two layers. By applying a top gate voltage, charge carries are induced in the top layer of the bilayer graphene that lower the symmetry of the system and then, two peaks are observed in the G band of the Raman spectrum. By monitoring the frequency, the width and the relative intensity of the two peaks of the G band and comparing our experimental results with theoretical calculations made by Gava *et al.* [82], we could probe distinct electron-phonon couplings in bilayer graphene and estimate the amount of unintentional doping that comes from the environment.

In the second part of this thesis, we probed the electronic and vibrational structure of bilayer graphene by analyzing the G$'$ band measured with laser excitation energies in the visible and near-infrared region (1.33-2.81 eV). Within the Slonczewski-Weiss-McClure

(SWM) parametrization [22,23], we can adjust the phonon dispersion and obtain the γ_0, γ_1,γ_3 ,γ_4, Δ and t' hopping parameters considering both the outer and the inner double resonance Raman processes, as well as the phonon dispersion for the symmetric and anti-symmetric iTO phonon branches. By comparing our SWM hopping parameters with those obtained in the literature by other experimental techniques and calculations, we showed that the inner double resonance process is the main responsible for the origin of the G$'$ band in bilayer graphene.

Finally, by the study of the dependence of the relative intensity of the four peaks of the G$'$ band of bilayer graphene on laser energy and laser power, we could have information about the phonon dynamics in bilayer graphene. We showed that, due to the strong electron-phonon coupling and the fast electron thermalization, some processes experience a decrease in their scattering rate due to electron relaxation through the conduction band by low-energy phonon emission. This decreased scattering rate contributes to the increase of the rate of another scattering process.

This work shows how important the electron-phonon interactions are in solid state materials. The well understanding of such interactions is essential for the correct application of the material in technological devices. We show that the Raman spectroscopy is a powerful technique to materials characterization and a wealth of information can be obtained by the properly analysis of the Raman spectra.

Appendix A

Publications

1. Mafra, D. L.; Kong, J.; Sato, K.; Saito, R.; Dresselhaus, M. S.; Araujo, P.T.. "Using the G′ Raman cross-section to understand the phonon dynamics in bilayer graphene systems". *Nano Letters*, v. 12, p. 2883, 2012.

2. Araujo, P. T.†; Mafra, D. L.†; Sato, K.; Saito, R.; Kong, J.; Dresselhaus, M. S.. "Phonon selfenergy corrections to non-zero wavevector phonon modes in single-layer graphene". *Physical Review Letters*, v. 109, p. 046801, 2012. †Those authors contributed equally for the work.

3. Mafra, D. L.; Kong, J.; Sato, K.; Saito, R.; Dresselhaus, M. S.; Araujo, P.T.. "Using gate-modulated Raman scattering and electron-phonon interactions to probe single layer graphene: a new technique to assign phonon combination modes". Under review in *Nano Letters*.

4. Mafra, D. L.; Gava, P.; Malard, L. M.; Borges, R. S.; Silva, G. G.; Leon, J. A.; Plentz, F.; Mauri, F; Pimenta, M. A.. "Characterizing intrinsic charges in top gated bilayer graphene device by Raman spectroscopy". *Carbon*, v. 50, p. 3435, 2012.

5. Mafra, D. L.; Moujaes, E. A.; Doorn, S. K.; Htoon, H.; Nunes, R. W.; Pimenta, M. A.. "A study of inner process double-resonance Raman scattering in bilayer graphene". *Carbon*, v. 49, p. 1511, 2011.

6. Mafra, D. L.; Malard, L. M.; Doorn, S. K.; Htoon, H.; Nilsson, J.; Castro Neto, A. H.; Pimenta, M. A.. "Observation of the Kohn anomaly near the K point of bilayer graphene". *Physical Review B* (Rapid Communications), v. 80, p. 241414, 2009.

7. Malard, L. M.; Mafra, D. L.; Doorn, S. K.; Pimenta, M. A.. "Resonance Raman scattering in graphene: Probing phonons and electrons". *Solid State Communications*, v. 149, p. 1136, 2009.

8. Malard, L. M.; Guimarães, M. H. D.; Mafra, D. L.; Mazzoni, M. S. C.; Jorio, A.. "Group theory analysis of electrons and phonons in N -layer graphene systems". *Physical Review B*, v. 79, p. 125426, 2009.

9. Malard, L. M.; Nilsson, J.; Mafra, D. L.; Elias, D. C.; Brant, J. C.; Plentz, F.; Alves, E. S.; Castro Neto, A. H.; Pimenta, M. A.. "Electronic properties of bilayer graphene probed by Resonance Raman Scattering". *Physica Status Solidi B*, v. 245, p. 2060, 2008.

Appendix B

Characters tables

In this Appendix, the character tables for all points inside the first Brillouin zone of graphene will be given, as well as the base function, the character of equivalence χ^{eq} and the atom equivalence representation Γ^{eq} for each table. With Γ^{eq} is possible to calculate the representations for electrons and vibrations for each point in the Brillouin zone, as done in Chapter 2.2 and 2.3 [122].

Table B.1: Character table for the Γ point.

D_{6h}	E	C_2	$2C_3$	$2C_6$	$3C_2'$	$3C_2''$	i	σ_h	$2S_6$	$2S_3$	$3\sigma_d$	$3\sigma_v$	
Γ_1^+	1	1	1	1	1	1	1	1	1	1	1	1	x^2+y^2,z^2
Γ_2^+	1	1	1	1	-1	-1	1	1	1	1	-1	-1	
Γ_3^+	1	-1	1	-1	1	-1	1	-1	1	-1	1	-1	
Γ_4^+	1	-1	1	-1	-1	1	1	-1	1	-1	-1	1	
Γ_5^+	2	-2	-1	1	0	0	2	-2	-1	1	0	0	(xz, yz)
Γ_6^+	2	2	-1	-1	0	0	2	2	-1	-1	0	0	(x^2-y^2, xy)
Γ_1^-	1	1	1	1	1	1	-1	-1	-1	-1	-1	-1	
Γ_2^-	1	1	1	1	-1	-1	-1	-1	-1	-1	1	1	z
Γ_3^-	1	-1	1	-1	1	-1	-1	1	-1	1	-1	1	
Γ_4^-	1	-1	1	-1	-1	1	-1	1	-1	1	1	-1	
Γ_5^-	2	-2	-1	1	0	0	-2	2	1	-1	0	0	(x, y)
Γ_6^-	2	2	-1	-1	0	0	-2	-2	1	1	0	0	
χ^{eq}	2	0	2	0	0	2	0	2	0	2	2	0	$\Gamma^{eq} = \Gamma_1^+ + \Gamma_4^-$

Table B.2: Character table for the K (K') point.

D_{3h}	E	$2C_3$	$3C_2'$	σ_h	$2S_3$	$3\sigma_v$	
K_1^+	1	1	1	1	1	1	x^2+y^2,z^2
K_2^+	1	1	-1	1	1	-1	
K_3^+	2	-1	0	2	-1	0	(x, y),(x^2-y^2, xy)
K_1^-	1	1	1	-1	-1	-1	
K_2^-	1	1	-1	-1	-1	1	z
K_3^-	2	-1	0	-2	1	0	
χ^{eq}	2	-1	0	2	-1	0	$\Gamma^{eq} = K_3^+$

Table B.3: Character table for the M point.

D_{2h}	E	C_2	C_2'	C_2''	i	σ_h	σ_d	σ_v	
M_1^+	1	1	1	1	1	1	1	1	x^2, y^2, z^2
M_2^+	1	1	-1	-1	1	1	-1	-1	xy
M_3^+	1	-1	1	-1	1	-1	1	-1	xz
M_4^+	1	-1	-1	1	1	-1	-1	1	yz
M_1^-	1	1	1	1	-1	-1	-1	-1	
M_2^-	1	1	-1	-1	-1	-1	1	1	z
M_3^-	1	-1	1	-1	-1	1	-1	1	y
M_4^-	1	-1	-1	1	-1	1	1	-1	x
χ^{eq}	2	0	0	2	0	2	2	0	$\Gamma^{eq} = M_1^+ + M_4^-$

Table B.4: Character table for the $T\,(T')$ point.

C_{2v}	E	C_2'	σ_h	σ_v	
T_1	1	1	1	1	$y,\ x^2, y^2, z^2$
T_2	1	1	-1	-1	xz
T_3	1	-1	1	-1	x, xy
T_4	1	-1	-1	1	z, yz
χ^{eq}	2	0	2	0	$\Gamma^{eq} = T_1 + T_3$

Table B.5: Character table for the Σ point.

C_{2v}	E	C_2'	σ_h	σ_v	
Σ_1	1	1	1	1	$x,\ x^2, y^2, z^2$
Σ_2	1	1	-1	-1	zy
Σ_3	1	-1	1	-1	y, xy
Σ_4	1	-1	-1	1	z, zx
χ^{eq}	2	2	2	2	$\Gamma^{eq} = 2\Sigma_1$

Table B.6: Character table for the u point.

C_{1h}	E	σ_h	
u^+	1	1	$x, y,\ x^2, y^2, z^2, xy$
u^-	1	-1	z, zy, zx
χ^{eq}	2	2	$\Gamma^{eq} = 2u^+$

Bibliography

[1] O. Heinonen P. L. Taylor. *A quantum approach to condensed matter physics*. Cambridge University Press, 2002.

[2] F. Bonaccorso, Z. Sun, T. Hasan, A. C. Ferrari. *Nature Photonics*, 4:611, 2010.

[3] A. H. Castro Neto, F. Guinea, N. M. R. Peres, K. S. Novoselov, A. K. Geim. *Reviews of Modern Physics*, 81:109, 2009.

[4] S. Stankovich, D. A. Dikin, G. H. B. Dommett, K. M. Kohlhaas, E. J. Zimney, E. A. Stach, R. D. Piner, S. T. Nguyen, R. S. Ruoff. *Nature*, 442:282, 2006.

[5] K. S. Novoselov, A. K. Geim, S. V. Morozov, D. Jiang, M. I. Katsnelson, I. V. Grigorieva, S. V. Dubonos, A. A. Firsov. *Nature*, 438:197, 2005.

[6] Y. Zhang, Y. W. Tan, H. L. Stormer, P. Kim. *Nature*, 438:201, 2005.

[7] K. S. Kim, Y. Zhao,H. Jang, S. Y. Lee, J. M. Kim, J. H. Ahn, P. Kim, J. Y. Choi, B. H. Hong. *Nature*, 457:706, 2009.

[8] S. Bae, H. Kim, Y. Lee, X. Xu, J. S. Park, Y. Zheng, J. Balakrishnan, T. Lei, H. R. Kim, Y. I. Song, Y. J. Kim, K. S. Kim, B. Özyilmaz, J. H. Ahn, B. H. Hong, S. Iijima. *Nature Nanotechnology*, 5:574, 2010.

[9] A. K. Geim, K. S. Novoselov. *Nature Materials*, 6:183, 2007.

[10] A. B. Kuzmenko, E. van Heumen, D. van der Marel, P. Lerch, P. Blake, K. S. Novoselov, A. K. Geim. *Physical Review B*, 79:115441, 2009.

[11] P. Gava, M. Lazzeri, A. M. Saitta, F. Mauri. *Physical Review B*, 79:165431, 2009.

[12] R. Van Noorden. *Nature*, 442:228, 2006.

[13] G. Konstantatos, M. Badioli, L. Gaudreau, J. Osmond, M. Bernechea, F. P. Garcia de Arquer, F. Gatti, F. H. L. Koppens. *Nature Nanotechnology*, 7:363, 2012.

[14] P. Matyba, H. Yamaguchi, G. Eda, M. Chhowalla, L. Edman, N. D. Robinson. *ACS Nano*, 4:637, 2010.

[15] B. M. Venkatesan, R. Bashir. *Nature Nanotechnology*, 6:615, 2011.

[16] L. M. Malard, M. A. Pimenta, G. Dresselhaus, M. S. Dresselhaus. *Physics Reports*, 473:51, 2009.

[17] D. L. Mafra, G. Samsonidze, L. M. Malard, D. C. Elias, J. C. Brant, F. Plentz, E. S. Alves, M. A. Pimenta. *Physical Review B*, 76:233407, 2007.

[18] L. M. Malard, J. Nilsson, D. C. Elias, J. C. Brant, F. Plentz, E. S. Alves, A. H. Castro Neto, M. A. Pimenta. *Physical Review B*, 76:201401, 2007.

[19] M. Lazzeri, F. Mauri. *Physical Review Letters*, 97:266407, 2006.

[20] M. S. Dresselhaus R. Saito, G. Dresselhaus. *Physical Properties of Carbon Nanotubes*. Imperial College Press, London, 1998.

[21] P. R. Wallace. *Physics Review*, 71:622, 1947.

[22] J. W. McClure. *Physics Review*, 108:612, 1957.

[23] J. C. Slonczewski, P. R. Weiss. *Physics Review*, 109:272, 1958.

[24] B. Partoens, F. M. Peeters. *Physical Review B*, 74:075404, 2006.

[25] A. Das, B. Chakraborty, S. Piscanec, S. Pisana, A. K. Sood, A. C. Ferrari. *Physical Review B*, 79:155417, 2009.

[26] T. Ohta, A. Bostwick, T. Seyller, K. Horn, E. Rotenberg. *Science*, 311:951, 2006.

[27] N. V. Popov, P. Lambin. *Physical Review B*, 73:085407, 2006.

[28] L. M. Malard, M. H. D. Guimaraes, D. L. Mafra, M. S. C. Mazzoni, A. Jorio. *Physical Review B*, 79:125426, 2009.

[29] S. Piscanec, M. Lazzeri, F. Mauri, A. C. Ferrari, J. Robertson. *Physical Review Letters*, 93:185503, 2004.

[30] T. Ando. *Journal of the Physical Society of Japan*, 75:024707, 2006.

[31] J. Yan, E. A. Henriksen, P. Kim, A. Pinczuk. *Physical Review Letters*, 101:136804, 2008.

[32] S. Pisana, M. Lazzeri, C. Casiraghi, K. S. Novoselov, A. K. Geim, A. C. Ferrari, F. Mauri. *Nature Materials*, 6:198, 2007.

[33] T. Ando. *Journal of the Physical Society of Japan*, 76:104711, 2007.

[34] L. M. Malard, D. C. Elias, E. S. Alves, M. A. Pimenta. *Physical Review Letters*, 101:257401, 2008.

[35] T. Ando, M. Koshino. *Journal of the Physical Society of Japan*, 78:034709, 2009.

[36] J. Yan, T. Villarson, E. A. Henriksen, P. Kim, A. Pinczuk. *Physical Review B*, 80:241417(R), 2009.

[37] P. T. Araujo, D. L. Mafra, K. Sato, R. Saito, J. Kong, M. S. Dresselhaus. *Physical Review Letters*, 109:046801, 2012.

[38] A. V. Baranov, A. N. Bekhterev, Y. S. Bobovich, V. I. Petrov. *Optics and Spectroscopy*, 62:612, 1987.

[39] R. Saito, A. Jorio, A. G. Souza Filho, G. Dresselhaus, M. S. Dresselhaus, M. A. Pimenta. *Physical Review Letters*, 88:027401, 2001.

[40] C. Thomsen, S. Reich. *Physical Review Letters*, 85:5214, 2000.

[41] A. C. Ferrari, J. C. Meyer, V. Scardaci, C. Casiraghi, M. Lazzeri, F. Mauri, S. Piscanec, D. Jiang, K. S. Novoselov, S. Roth, A. K. Geim. *Physical Review Letters*, 97:187401, 2006.

[42] K. S. Novoselov, A. K. Geim, S. V. Morozov, D. Jiang, Y. Zhang, S. V. Dubonos, I. V. Grigorieva, A. A. Firsov. *Science*, 306:666, 2004.

[43] A. Reina, H. B. Son, L. Y. Jiao, B. Fan, M. S. Dresselhaus, Z. F. Liu, J. Kong. *Journal of Physical Chemistry C*, 112:17741, 2008.

[44] Z. Q. Li, E. A. Henriksen, Z. Jiang, Z. Hao, M. C. Martin, P. Kim, H. L. Stormer, D. N. Basov. *Physical Review Letters*, 102:037403, 2009.

[45] C. Berger, Z. M. Song, X. B. Li, X. S. Wu, N. Brown, C. Naud, D. Mayo, T. B. Li, J. Hass, A. N. Marchenkov, E. H. Conrad, P. N. First, W. A. de Heer. *Science*, 312:1191, 2006.

[46] D. A. Dikin, S. Stankovich, E. J. Zimney, R. D. Piner, G. H. B. Dommett, G. Evmenenko, S. T. Nguyen, R. S. Ruoff. *Nature*, 448:457, 2007.

[47] P. Blake, E. W. Hill, A. H. Castro Neto, K. S. Novoselov, D. Jiang, R. Yang, T. J. Booth, A. K. Geim. *Applied Physics Letters*, 91:063124, 2007.

[48] S. H. Lewis R. G. Meyer P. R. Gray, P. J. Hurst. *Analysis and Design of Analog Integrated Circuits - Fifth Edition*. Wiley, New York, 2009.

[49] N. D. Mermin N. W. Ashcroft. *Solid State Physics*. Saunders College Publishing, Fort Worth, 1989.

[50] J. Yan. *Raman Spectroscopy of Graphene*. Graduate School of Arts and Sciences - Comlumbia University, 2009.

[51] L. R. Faulkner A. J. Bard. *Electrochemical Methods, Fundamentals and Applications*. John Wiley and Sons, New York, 1980.

[52] A. Das, S. Pisana, B. Chakraborty, S. Piscanec, S. K. Saha, U. V. Waghmare, K. S. Novoselov, H. R. Krishnamurthy, A. K. Geim, A. C. Ferrari, A. K. Sood. *Nature Nanotechnology*, 3:210, 2008.

[53] J. W. Lamb. *International Journal of Infrared and Millimeter Waves*, 17:1997, 1996.

[54] O. Dubay, G. Kresse, H. Kuzmany. *Physical Review Letters*, 88:235506, 2002.

[55] A. Sedeki, L. G. Caron, C. Bourbonnais. *Physical Review B*, 62:6975, 2000.

[56] V. M. Stojanovic, N. Vukmirovic, C. Bruder. *Physical Review B*, 82:165410, 2010.

[57] C. Nisoli. *Physical Review B*, 80:113406, 2009.

[58] H. Farhat, K. Sasaki, M. Kalbac, M. Hofmann, R. Saito, M. S. Dresselhaus, J. Kong. *Physical Review Letters*, 102:126804, 2009.

[59] C.-H. Park, F. Giustino, M. L. Cohen, S. G. Louie. *Nano Letters*, 8:4229, 2008.

[60] K. Sasaki, H. Farhat, R. Saito, M. S. Dresselhaus. *Physica E*, 42:2005, 2010.

[61] R. Saito G. Dresselhaus A. Jorio, M. S. Dresselhaus. *Raman Spectroscopy in Graphene Related Systems*. WILEY-VCH, Weinheim, 2011.

[62] J. C. Meyer, A. K. Geim, M. I. Katsnelson, K. S. Novoselov, T. J. Booth, S. Roth. *Nature*, 446:60, 2007.

[63] J. Jiang, R. Saito, A. Grüneis, G. Dresselhaus, M. S. Dresselhaus. *Chemical Physics Letters*, 392:383, 2004.

[64] J. Yan, Y. Zhang, P. Kim, A. Pinczuk. *Physical Review Letters*, 98:166802, 2007.

[65] T. Shimada, T. Sugai, C. Fantini, M. Souza, L. G. Cançado, A. Jorio, M. A. Pimenta, R. Saito, A. Grüneis, G. Dresselhaus, M. S. Dresselhaus, Y. Ohno, T. Mizutani, H. Shinohara. *Carbon*, 43:1049, 2005.

[66] A. G. Souza Filho, A. Jorio, G. Dresselhaus, M. S. Dresselhaus, R. Saito, A. K. Swan, M. S. Ünlü, B. B. Goldberg, J. H. Hafner, C. M. Lieber, M. A. Pimenta. *Physical Review B*, 65:035404, 2001.

[67] R. Rao, R. Podila, R. Tsuchikawa, J. Katoch, D. Tishler, A. M. Rao, M. Ishigami. *ACS Nano*, 5:1594, 2011.

[68] C. Cong, T. Yu, R. Saito, G. Dresselhaus, M. S. Dresselhaus. *ACS Nano*, 5:1600, 2011.

[69] K. Sato, J. S. Park, R. Saito, C. Cong, T. Yu, C. H. Lui, T. Heinz, G. Dresselhaus, M. S. Dresselhaus. *Physical Review B*, 84:035419, 2011.

[70] C. Cong, T. Yu, K. Sato, J. Shang, R. Saito, G. Dresselhaus, M. S. Dresselhaus. *ACS Nano*, 5:8760, 2011.

[71] K. Sasaki, M. Yamamoto, S. Murakami, R. Saito, M. S. Dresselhaus, K. Takai, T. Mori, T. Enoki, K. Wakabayashi. *Physical Review B*, 80:155450, 2009.

[72] R. Saito, A. Grüneis, Ge. G. Samsonidze, V. W. Brar, G. Dresselhaus, M. S. Dresselhaus,A. Jorio, L. G. Cançado, C. Fantini, M. A. Pimenta, A. G. Souza Filho. *New Journal of Physics*, 5:157, 2003.

[73] M. A. Pimenta, G. Dresselhaus, M. S. Dresselhaus, L. G. Cancado, A. Jorio, R. Saito. *Physical Chemistry Chemical Physics*, 9:1276, 2007.

[74] J. Maultzsch, S. Reich, C. Thomsen. *Physical Review B*, 70:155403, 2004.

[75] D. L. Mafra, E. A. Moujaes, S. K. Doorn, H. Htoon, R. W. Nunes, M. A. Pimenta. *Carbon*, 49:1511, 2011.

[76] D. L. Mafra, J. Kong, K. Sato, R. Saito, M. S. Dresselhaus, P. T. Araujo. *submitted*, 2012.

[77] E. McCann. *Physical Review B*, 74:161403, 2006.

[78] E. V. Castro, K. S. Novoselov, S. V. Morozov, N. M. R. Peres, J. M. B. Lopes dos Santos, J. Nilsson, F. Guinea, A. K. Geim, A. H. Castro Neto. *Physical Review Letters*, 99:216802, 2007.

[79] J. B. Oostinga, H. B. Heersche, X. Liu, A. F. Morpurgo, L. M. K. Vandersypen. *Nature Materials*, 7:151, 2008.

[80] Y. Zhang, T. Tang, C. Girit, Z. Hao, M. C. Martin, A. Zettl, M. F. Crommie, Y. R. Shen, F. Wang. *Nature*, 459:820, 2009.

[81] K. F. Mak, C. H. Lui, J. Shan, T. F. Heinz. *Physical Review Letters*, 102:256405, 2009.

[82] P. Gava, M. Lazzeri, A. M. Saitta, F. Mauri. *Physical Review B*, 80:155422, 2009.

[83] M. Bruna, S. Borini. *Physical Review B*, 81:125421, 2010.

[84] L. M. Zhang, Z. Q. Li, D. N. Basov, M. M. Fogler, Z. Hao, M. C. Martin. *Physical Review B*, 78:235408, 2008.

[85] T. Ozel, A. Gaur, J. A. Rogers, M. Shim. *Nano Letters*, 5:905, 2005.

[86] K. Bradley, J. Cumings, A. Star, J. -C. P. Gabriel, G. Gruner. *Nano Letters*, 3:639, 2003.

[87] H. Wang, Y. Wu, C. Cong, J. Shang, T. Yu. *ACS Nano*, 4:7221, 2010.

[88] H. Min, B. Sahu, S. K. Banerjee, A. H. MacDonald. *Physical Review B*, 75:155115, 2007.

[89] A. Grüneis, C. Attaccalite, L. Wirtz, H. Shiozawa, R. Saito, T. Pichler, A. Rubio. *Physical Review B*, 78:205425, 2008.

[90] D. L. Mafra, L. M. Malard, S. K. Doorn, H. Htoon, J. Nilsson, A. H. Castro Neto, M. A. Pimenta. *Physical Review B*, 80:241414(R), 2009.

[91] A. B. Kuzmenko, L. Benfatto, E. Cappelluti, I. Crassee, D. van der Marel, P. Blake, K. S. Novoselov, A. K. Geim. *Physical Review Letters*, 103:116804, 2009.

[92] L. M. Malard, J. Nilsson, D. L. Mafra, D. C. Elias, J. C. Brant, F. Plentz, E. S. Alves, A. H. Castro Neto, M. A. Pimenta. *Physica Status Solidi B*, 245:2060, 2008.

[93] J. Kurti, V. Zolyomi, A. Gruneis, H. Kuzmany. *Physical Review B*, 65:165433, 2002.

[94] D. Yoon, Y. -W. Son, H. Cheong. *Physical Review Letters*, 106:155502, 2011.

[95] M. Mohr, J. Maultzsch, C. Thomsen. *Physical Review B*, 82:201409(R), 2010.

[96] K. Sugihara I. L. Spain H. A. Goldberg M. S. Dresselhaus, G. Dresselhaus. *Graphite Fibers and Filaments*. Springer Series in Materials Science, vol. *5*, Springer-Verlag: Berlin, 1988.

[97] J. M. Schneider, M. Orlita, M. Potemski, D. K. Maude. *Physical Review Letters*, 102:166403, 2009.

[98] P. Venezuela, M. Lazzeri, F. Mauri. *Physical Review B*, 84:035433, 2011.

[99] Z. H. Ni, T. Yu, Y. H. Lu, Y. Wang, Y. P. Feng, Z. X. Shen. *ACS Nano*, 2:2301, 2008.

[100] T. Yu, Z. Ni, C. Du, Y. You, Y. Wang, Z. Shen. *Journal of Physical Chemistry*, 112:12602, 2008.

[101] V. M. Pereira, A. H. Castro Neto. *Physical Review Letters*, 103:046801, 2009.

[102] M. Lazzeri, C. Attaccalite, L. Wirtz, F. Mauri. *Physical Review B*, 78:081406(R), 2008.

[103] S. V. Morozov, K. S. Novoselov, M. I. Katsnelson, F. Schedin, D. C. Elias, J. A. Jaszczak, A. K. Geim. *Physical Review Letters*, 100:016602, 2008.

[104] A. K. Geim. *Science*, 324:1530, 2009.

[105] P. Avouris, Z. Chen, V. Perebeinos. *Nature Nanotechnology*, 2:605, 2007.

[106] J. -U. Lee, D. Yoon, H. Kim, S. W. Lee, H. Cheong. *Physical Review B*, 83:081419(R), 2011.

[107] S. Chen, A. L. Moore, W. Cai, J. W. Suk, J. An, C. Mishra, C. Amos, C. W. Magnuson, J. Kang, L. Shi, R. S. Ruoff. *ACS Nano*, 5:321, 2011.

[108] A. A. Balandin. *Nature Materials*, 10:569, 2011.

[109] D. Yoon, Y. -W. Son, H. Cheong. *Nano Letters*, 11:3227, 2011.

[110] T. Hertel, G. Moos. *Chemical Physics Letters*, 320:359, 2000.

[111] K. Seibert, G. C. Cho, H. Kurz, W. Kutt, D. H. Reitze, J. I. Dadap, H. Ahn, M. C. Downer. *Physical Review B*, 42:2842, 1990.

[112] N. Bonini, M. Lazzeri, N. Marzari, F. Mauri. *Physical Review Letters*, 99:176802, 2007.

[113] S. G. Chou, M. F. DeCamp, J. Jiang, Ge. G. Samsonidze, E. B. Barros, F. Plentz, A. Jorio, M. Zheng, G. B. Onoa, E. D. Semke, A. Tokmakoff, R. Saito, G. Dresselhaus, M. S. Dresselhaus. *Physical Review B*, 72:195415, 2005.

[114] S. G. Chou, F. Plentz, J. Jiang, R. Saito, D. Nezich, H. B. Ribeiro, A. Jorio, M. A. Pimenta, Ge. G. Samsonidze, A. P. Santos, M. Zheng, G. B. Onoa, E. D. Semke, G. Dresselhaus, M. S. Dresselhaus. *Physical Review Letters*, 94:127402, 2005.

[115] K. M. Borysenko, J. T. Mullen, X. Li, Y. G. Semenov, J. M. Zavada, M. B. Nardelli, K. W. Kim. *Physical Review B*, 83:161402(R), 2011.

[116] I. Calizo, A. A. Balandin, W. Bao, F. Miao, C. N. Lau. *Nano Letters*, 7:2645, 2007.

[117] P. H. Tan, Y. M. Deng, Q. Zhao, W. C. Cheng. *Applied Physics Letters*, 74:1818, 1999.

[118] J. Jiang, R. Saito, Ge. G. Samsonidze, S. G. Chou, A. Jorio, G. Dresselhaus, M. S. Dresselhaus. *Physical Review B*, 72:235408, 2005.

[119] L. J. Karssemeijera, A. Fasolinoa. *Surface Science*, 605:1611, 2011.

[120] T. .J. Echtermeyer, L. Britnell, P. K. Jasnos, A. Lombardo, R. V. Gorbachev, A. N. Grigorenko, A. K. Geim, A. C. Ferrari, K. S. Novoselov. *Nature Communications*, 2:458, 2011.

[121] M. C. Lemme, F. H. L. Koppens, A. L. Falk, M. S. Rudner, H. Park, L. S. Levitov, C. M. Marcus. *Nano Letters*, 11:4134, 2011.

[122] A. Jorio M. S. Dresselhaus, G. Dresselhaus. *Group Theory: Application to the Physics of Condensed Matter*. Springer-Verlag, Berlin, 2008.